Novel Mesh Generation Method
for Accurate Image-Based Computational Modelling of Blood Vessels

Nieuwe roostergeneratiemethode
voor nauwkeurige beeldgebaseerde computermodellering van bloedvaten

Gianluca De Santis

UNIVERSITEIT
GENT

Supervisors:

prof. dr. ir. Benedict Verhegghe
prof. dr. ir. Pascal Verdonck

Examination Committee:

prof. dr. ir. H. Van Landeghem (chairman)	Ghent University
dr. ir. M. De Beule (secretary)	Ghent University
prof. dr. ir. U. Morbiducci	Politecnico di Torino (IT)
prof. dr. ir. F. van de Vosse	Eindhoven University of Technology (NL)
prof. dr. ir. J. Vierendeels	Ghent University
prof. dr. ir. P. Segers	Ghent University
prof. dr. ir. B. Verhegghe	Ghent University
prof. dr. ir. P. Verdonck	Ghent University

Research lab:

Biofluid, Tissue and Solid Mechanics for Medical Applications
Institute Biomedical Technology
Ghent University
De Pintelaan 185 - Blok B
B-9000 Gent
Belgium

Acknowledgements

L'alba e la sera: crepuscoli ambedue di questa vita.
Ma tu sei l'alba, io son la sera.

The dawn and the dusk: both twilights of this life.
But you are the dawn, I am the dusk.

—Nonno Nino, my grand father,
wrote it to comment a picture of him with my daughter.

If you work with nice people four years pass very quickly. The first year was the slowest, because at that time I could not clearly see where my research was directed. I learned that in a marathon being optimistic is more important than rushing (though, I have never run one yet!). I would like to thank the people that gave me this lesson and ran with me.

Benedict (the Prophet), your technical expertise was necessary, from the beginning till the end, to translate my tortuous ideas into many straightforward pieces, and then implement them as pyFormex scripts. It was a privilege to learn from you. Pascal, thanks for supervising me during the (very pleasant) Erasmus period and for giving me the chance to join the Lab. Patrick, thanks for your punctual revisions, for promoting the application of my cubes and for keeping the harmony in the Lab.

I am very grateful to Matthieu, who has taken care of me like an older brother, and Peter, who, after a toilet trauma, has become a major supporter of my cubes. I hope this can continue! Thanks to dr. Umberto Morbiducci for using my cubes in his Lab, dr. Luca Antiga for having developed a lot of tools, useful for my research, and prof. Jan Vierendeels, for discussing with me some technical points. I feel gratified when I see an application of my cubes in the research of my collegues: Michele (who called me *disturbia*), Bram, Abigail, Koen, Francesco, Sander, Joris and Diego. I would like to thank Tomas and Sofie for sharing their pyFormex experiences with me and Mirko and Luis for accepting my frequent invitations to take a coffee.

Some years ago my teacher Salvatore Negro has trained me with enthusiasm in math and geometry. I think he was the first one I met with the 'obsession' of (geometrical) parametric analysis. Was my PhD already started 11 years ago?

Thanks Femke for training my happiness, Anna-Rosa for sharing your smile with me, *papà e mamma* for having given me roots and wings (*le radici e le ali*), *nonni e nonne* for being funny, Bernard and Annemie for making me feel home...in your home :).

Gent, October 2011

Gianluca

Contents

Samenvatting

De eerste melding van atherosclerose werd waarschijnlijk gemaakt door Leonardo da Vinci. Na de autopsie op een eeuweling, rustig in bed overleden in het hospitaal Santa Maria Nuova, het oudste nog actieve ziekenhuis in Firenze, schreef de geleerde: de doodsoorzaak *is zwakte door het falen van het bloed en de arterie die het hart en de ledematen van bloed voorziet* (i.e. de aorta), *die ik zeer droog, gekrompen en verschrompeld vond ... en door het gebrek aan voeding* (i.e. bloedstroom) *... door de vernauwing van de doorgang van de mesenteriale vaten door verdikking van de wand*. Toen da Vinci later een autopsie uitvoerde op een tweejarig kind schreef hij: *hier vond ik alles tegengesteld aan hoe het was bij de oude man*. Uit deze tekst is het duidelijk dat Leonardo in de oude patiënt een toegenomen arteriële stijfheid en stenoses vond, die niet aanwezig zijn in de jonge patiënt. In veroudering ziet hij de oorzaak van de degeneratie van de vaatwand, want *de vaatwand gedraagt zich in de mens als een sinaasappel, waarvan de schil verdikt en de pulp vermindert als ze ouder worden*. En hij tracht een verklaring te vinden in het feit dat *iets dat dichter ligt bij zijn voedingsbron meer zal opnemen, en hierdoor, aangezien de bloedvaten het bloed omhullen dat het lichaam voedt, de vaten meer gevoed worden door hun nabijheid*, wat doet denken aan de rol van cholesterol in de verdikking van de intima [1].

Het directe zicht op de arteriële weefsels liet Leonardo toe om voor te lopen op vele eeuwen kennisverwerving rond arteriële fysiopathologie, ook al had hij er geen notie van dat de bloedsomloop een gesloten circulair systeem is. Hij ging mee in de (in die tijd wijdverspreide) opvatting dat bloed werd gemaakt in de lever, gekoeld in de longen, doorgepompt in het hart en opgebruikt in de spieren [2]. In plaats van direct het arteriële systeem met een autopsie te onderzoeken (in de 16e eeuw waarschijnlijk de enige optie), zorgt moderne medische beeldvorming voor een krachtig en niet invasieve alternatief, en, door koppeling met computeranalyses (i.e. beeld-gebaseerde analyse) kan in silico het in vivo voorkomend geval gerepliceerd worden. Dit proefschrift beschrijft de technologische vooruitgang in vasculaire beeld-gebaseerde analyse, ontwikkeld tijdens vier jaar onderzoeksactiviteit.

Hoofdstuk 1. Inleiding

Cardiovasculaire ziekte is de meest voorkomende doodsoorzaak wereldwijd, verantwoordelijk voor 48% van alle doden in Europa [3,4]. Een van de meest voorkomende cardiovasculaire ziektes is atherosclerose, een ziektebeeld dat vaak leidt tot vernauwde slagaders en trombo-embolische voorvallen, waarbij de perfusie van de stroomafwaarts gelegen weefsels in gevaar komt.

Ondanks het systemische risico manifesteert atherosclerose zich in de grote slagaders als geometrische, focale plaques, met een locale wijziging van de anatomie, histologie en mechanische eigenschappen van de aangetaste vaatwand. De enkele laag endotheelcellen, in de tunica intima, is in direct contact met het bloed en draagt het meest van de wandschuifspanning (WSS), de wrijfingskracht die voortkomt uit het stromende bloed. Endotheelcellen onderhevig aan de dwarskrachten opgewekt door het bloed reageren hierop door het bevorderen van vasculaire homeostase of door een hermodellering. De mechanisch gevoelige rol van de endotheelcellen verklaart het lokaal voorkomen van de effecten van atherosclerose in de buitenste randen van arterie bifurcaties en in zones met een hoge kromming. In deze regio's kan een verstoring van de bloedstroom een lage een oscillerende WSS veroorzaken, die een atherogevoelig fenotype van endotheelcellen kan bevorderen, en zo de vorming van plaque initieert.

Huidige beeldvormingstechnieken (ultrageluid, biplanaire angiografie, rotationele angiografie, computer tomografie (CT), magnetische resonantie beeldvorming (MRI), optische coherentietomografie (OCT) en intravasculaire ultrageluid (IVUS)) zijn wijdverspreid in ziekenhuizen voor het in beeld brengen van bloedvaten in vivo, waardoor diagnose en behandeling van stenoses mogelijk wordt. Meer recent werd een virtueel luik geopend op de in vivo bloedstroom en mechanica van de vaatwand met beeld-gebaseerde analyse, een unieke manier om de bestaande in vivo hemodynamica te onderzoeken en de uitkomst van vasculaire interventies te voorspellen (e.g. stenting).

Doordat de partiële differentiaalvergelijkingen die de bloedstroom en de mechanica van de wand beschrijven geen analytische oplossingen kennen, wordt het beeld-gebaseerde domein opgesplitst in subdomeinen, mesh elementen of cellen genaamd, waar de vergelijkingen gediscretiseerd worden en opgelost. Verschillende geometrische primitieven, zoals hexaëders, tetraëders en prisma's kunnen gebruikt worden voor het discretiseren van een volume (i.e. roostergeneratie), waarbij het type, de vorm, de vormkwaliteit, topologische ordening en oriëntatie van de elementen correct moeten gekozen worden, aangezien deze eigenschappen de nauwkeurigheid van de numerieke oplossing beïnvloeden. Het doel van dit proefschrift is het verbeteren van de mesh generatie voor beeld-gebaseerde analyse van

bloedvaten, met een focus op meshes van gestructureerde hexaëders, die een hoge nauwkeurigheid van de numerieke oplossing combineren met een lage computationele kost.

Hoofdstuk 2. Het effect van de discretisatie van het volume op de berekening van coronaire doorbloeding: een case study

Als eerste case werd een arteriële boom met tubulaire takken beschouwd: een linker coronaire slagaderwand gereconstrueerd van een biplanaire angiografie en gemodelleerd met circulaire secties langs de middellijn. De complexe arteriële structuur werd in een aantal eenvoudige delen onderverdeeld, met name rechte arteries en bifurcaties. Na de reconstructie van het oppervlak van elk onderdeel door longitudinale 'Bézier splines' wordt een isoparametrische transformatie toegepast om de subregio's van het lumen in te delen in gestructureerde hexaëdrale blokken (i.e. een cartesiaans rooster). Deze blokken worden samengevoegd, met als resultaat een 'multi-blok gestructureerde mesh' van hoge kwaliteit van het lumen van de coronairen, geschikt voor een numerieke stromingsmechanica berekening (CFD: computational fluid dynamics). Dit rekenrooster is conform en de topologie geeft de vertakkingen en draaiingen van de zijtakken weer, wat toelaat om meerdere niet-planaire bifurcaties te meshen. De cellen en de randen van de cellen zijn gealigneerd volgens de middellijn van de arterie, die de stroomrichting in een bijna rechte tak benaderd. De cellen kunnen in radiale richting gelaagd worden om de hoge snelheidsgradiënt te begroten.

Om de gegenereerde meshes te vergelijken met de meest voorkomende automatisch gegenereerde meshes, werd een serie gestructureerde hexaëderale meshes en een serie van ongestructureerde hybride meshes van tetraëders en prisma's getest voor de berekening van WSS tijdens een CFD berekening. Met dezelfde geometrie en randvoorwaarden heeft een gestructureerde mesh een lager aantal elementen nodig om een mesh-ongevoelige WSS te bekomen (met een zekere tolerantie), waardoor de berekening nauwkeuriger en sneller kan gebeuren met een lager geheugengebruik. Dit resultaat geeft aan dat het gebruik van gestructureerde meshes voordelig kan zijn voor beeld-gebaseerde analyse en is een motivatie voor verder methodologische ontwikkeling voor mesh generatie in beeld-gebaseerde arteriële domeinen.

Hoofdstuk 3. Bifmesh: hexaëdrale mesh generatie in een bijna-vlakke vertakking

De simulatie van de coronaire slagader suggereert dat de generatie van een hexaëdrale mesh mogelijk is, de efficiëntie van de berekening ten goede komt, maar ook een omvangrijke interventie door de gebruiker vereist: van de partitie van het domein in eenvoudige subregio's en de constructie van splines rond het lumen, tot het indelen in een cartesiaans rooster. De nood naar een vereenvoudigde procedure wordt gerealiseerd door een grafische implementatie van een meshing toepassing, 'de vasculaire BIFurcation MESHer', of 'Bifmesh'. De toepasbaarheid van de methode wordt beperkt tot een enkele bijna-vlakke bifurcatie, voorgesteld door een oppervlakte-model (STL-bestand: een geometrische beschrijving van het oppervlak door driehoeken), waardoor de nodige input door de gebruiker drastisch wordt verminderd, dit laat toe om een gestructureerde hexaëdrale mesh te genereren in enkele minuten tijd.

Een bifurcatie van de halsslagader wordt gekozen als een test case voor de implementatie van deze tool. Eerst wordt het oppervlak doorsneden met vlakken, die de STL omzetten naar een serie van secties. Hiervoor wordt van de gebruiker als input enkele punten rond de bifurcatie gevraagd, zodat een standaard bifurcatie topologie kan toegepast worden op de patiënt-specifieke bifurcatie geometrie. Vervolgens worden, net als voor de coronaire slagader, longitudinale splines gebruikt om het lumen te reconstrueren. Deze splines worden nu echter automatisch gegenereerd door de applicatie. Gebaseerd op de splines en op de middellijnen van een tak wordt een isoparametrische transformatie gebruikt om een 2D cartesiaans rooster in de doorsneden van het bloedvat te projecteren, om zo een serie topologisch equivalenten quadrilaterale meshes te genereren. Door deze meshes te verbinden wordt een volume mesh gegenereerd in een tak. Deze handelingen worden herhaald voor de overige twee takken, waardoor een gestructureerde hexaëdrale mesh van het lumen van de bifurcatie gegenereerd wordt. Door gebruik te maken van dezelfde strategie kan ook de arteriële wand gemeshed worden, na reconstructie van de buitenste wand, door beeldsegmentatie of door het lumenoppervlak te laten uitzetten. Het aantal elementen in het lumen en de wand kan *a priori* gespecificeerd worden aan de hand van enkele parameters, waardoor de gewenste mesh resolutie kan gekozen worden. De lumen en wand meshes gegenereerd met Bifmesh kunnen zowel voor CFD en FEA (finite element analysis) analyses dienen.

Hoofdstuk 4. Treemesh: multi-blok hexaëdrale rooster-generatie in een complexe vasculaire boomstructuur

Wanneer vasculair onderzoek, gebaseerd op medische beelden, gericht is op complexe arteriële gebieden en pathologische gevallen, komt men vaak in contact met bifurcaties, trifurcaties, n-furcaties, stenoses en aneurysma's. De topologie en de geometrie van deze structuren bemoeilijken het definiëren van een structuur voor de mesh. De ontwikkeling van een algemene methodologie die een eenvoudige en gebruiksvriendelijke mesh generatie toelaat is een grote uitdaging. Om dit doel te bereiken werd 'Treemesh' ontwikkeld, een framework dat rooster generatie toelaat op allerhande vasculaire netwerken. In plaats van te vertrekken van een voorgedefinieerde structuur, kan de gebruiker de topologie van de mesh zelf opbouwen door blokstructuren in het lumen te plaatsen. De centerlijn en bijhorende parameters, zoals deze kunnen worden opgevraagd door de Vascular Modeling Toolkit (VMTK). Deze vormen het geraamte waarmee de blokstructuren worden opgebouwd. Op basis van deze blokken wordt vervolgens een isoparametrische transformatie uitgevoerd gevolgd door een projectie wat resulteert in een multi-blok gestructureerd rooster binnenin het lumen. De projectie zorgt ervoor dat de buitenrand van de mesh het oorspronkelijk model van het buitenoppervlak met een grote nauwkeurigheid benadert. Na de generatie van een mesh voor het lumen kan er ook een mesh voor de wandstructuur gegenereerd worden. Wanneer geen informatie over de wanddikte is voorzien, kan de buitenwand alsnog gereconstrueerd worden op basis van de lokale grootte van de vaatwand en de anatomische data. Immers, voor ieder punt op de buitenwand van het lumen kan de afstand berekend worden tot aan de centerlijn (wat bij een cirkelvormige cilinder gelijk zou zijn aan de straal). Dit kan gebruikt worden om locatie afhankelijk een wanddikte toe te kennen. Zoals bij een Bifmesh, wordt het de gebruiker mogelijk gemaakt om in het mesh ontwerp het aantal elementen te specifiëren die gewenst zijn in de axiale, radiale en omtreksrichting. Wat de vaatwand betreft kan er een onderscheid gemaakt worden tussen de verschillende arteriële lagen (tunica intima, tunica media en tunica adventitia) zodat aan deze een verschillend materiaalmodel kan worden toegekend. Ook is het mogelijk het materiaal te voorzien van anisotropie om zo de collageen vezels aanwezig in het arterieel weefsel in rekening brengen. Uit twee voorbeelden, nl. een humane aorta boog en een abdominaal aorta aneurysma, kan de lezer afleiden dat de boomstructuur gebaseerde mesh methode (Treemesh) een robuuste en krachtige tool is voor het genereren van meshes met een hoge kwaliteit voor computationele analyses gebaseerd op medische beelden. De algemeenheid en de ruime toepasbaarheid van deze methode is, in vergelijking met de Bifmesh methode, ten koste van de langere tijd nodig voor de roostergeneratie.

Hoofdstuk 5. Toepassing van Bifmesh en Treemesh op realistische voorbeelden

Zowel de Bifmesh als de Treemesh kunnen gebruikt worden bij biomedisch onderzoek, meer bepaald in het domein van CFD, FEA en fluidum-structuur interactie (FSI) analyses. Hoofdstuk 5 voorziet een overzicht van de bijdrage aan reeds gepubliceerde werken waarin de nieuwe mesh generatie methodes werden toegepast.

Het gemak waarmee een Bifmesh kan worden geconstrueerd wordt bewezen door de volgende studies:

- het ontwerp van een arterioveneuze graft voor hemodialyse ter verbetering van de hemodynamica in de veneuze anastomose;

- de structurele performantie van verschillende zelf-expandeerbare stents in een patiënt-specifieke carotis bifurcatie;

- de structurele performantie van verschillende ballon-expandeerbare stents gebruik makend van een parametrische coronaire bifurcatie als bench-test.

De flexibiliteit en de algemeenheid waarmee een Treemesh kan geconstrueerd worden toont zich in het volgende onderzoek:

- een retrospectief onderzoek van de aorta hemodynamica in vijf muizen die een aneurysma hebben ontwikkeld;

- de kwantificatie van de impact van verschillende strategieën om de in vivo opgemeten randvoorwaarden op te leggen bij twee humane aorta bogen;

- een computationele en experimentele studie om de nauwkeurigheid van FEA te onderzoeken bij stent simulaties van de coronaire bifurcatie;

- een onderzoek van de wandbeweging bij een carotis bifurcatie om algoritmes voor ultrasone beeldvorming te testen.

Al deze toepassingen bevestigen de bruikbaarheid van de Bifmesh en de Treemesh voor mesh generatie op basis van medisch beelden.

Grote, veeleisende numerieke simulaties kunnen vereenvoudigd worden door een strategie die toelaat overgangsblokken te gebruiken in de Bifmesh en de Treemesh gebaseerde roosters. Met deze blokstructuren kan het aantal elementen in de dwarsdoorsnede van een bloedvat worden aangepast om zo de resolutie van de mesh te verlagen in de niet-kritische gebieden waarin men niet geïnteresseerd is. Dit vermindert de rekenduur en het geheugen verbruik nodig voor de berekeningen en vergemakkelijkt de post-processing.

Hoofdstuk 6. Een computationeel onderzoek om de hemodynamica te voorspellen na carotis stenting

Het simuleren van de stent procedure in een halsslagader door een, op medische beelden gebaseerde, eindige elementen analyse laat toe de geometrie van de gestente vaatwand te voorspellen. Hierbij wordt het patiënt-specifiek bloedvat en stent model in rekening gebracht, zoals getoond in hoofdstuk 5 (een toepassing van de Bifmesh). Na het inbrengen van de stent in het eindige elementen model kan er een CFD analyse worden uitgevoerd om de hemodynamica die zich zou instellen direct na het stenten te voorspellen. Een open-cell stent model, gelijkend op een commercieel beschibaar hulpmiddel, wordt ontplooid in een patient-specifieke carotis met behulp van FEA. Uit de vervormde vaatwand en stent wordt er een 'negatief' structuur gereconstrueerd, representatief voor het vloeistofdomein. Een drukverloop, gebaseerd op data uit de literatuur, wordt opgelegd aan de inlaat van de halsslagader en impedantie modellen worden voorzien aan de uitlaten van de interne en de externe halsslagader. In een eerste benadering wordt verondersteld dat deze randvoorwaarden ongevoelig zijn aan de aanwezigheid van de stent en aan de vormverandering van de vaatwand.

De WSS map identificeert kritische regio's in de buurt van een milde stenose, waar stent malappositie voorkomt, distaal van de stent - strut interconnecties en in het ostium van de externe halsslagader, waar zwevende struts de bloedstroming hinderen. De CFD analyse gebaseerd op medisch beeld gebaseerde FEA is geschikt om het resultaat van een patiënt-specifieke stent procedure te voorspellen, zowel wat het structuur- als het stromingsaspect betreft. In de toekomst kan het artsen voorzien van realistische scenario's die kunnen optreden na het stenten wat dus kan helpen in hun keuze naar het meest geschikte hulpmiddel, zowel bij training als in de klinische praktijk.

Hoofdstuk 7. Conclusie

Het laatste hoofdstuk van dit proefschrift omvat een overzicht van de belangrijkste bevindingen binnen dit onderzoek met betrekking tot de initiële doelstellingen. Toekomstige uitbreidingen voor zowel de Bifmesh als de Treemesh worden voorgesteld, gebaseerd op de verkregen resultaten en de nog lopende toepassingen.

Summary

Leonardo da Vinci is maybe the first to report a case of atherosclerosis. After the autopsy of a centenarian man, who died peacefully on a bed of the hospital Santa Maria Nuova, the oldest hospital still active in Florence, he wrote: the death *proceeded from weakness through the failure of blood and of the artery that feeds the heart and the other lower members* (i.e. the aorta), *which I found to be very dry, shrunked and withered ... and from the lack of sustenance* (i.e. the blood flow) *... brought by the continuous narrowing of the passage of the mesenteric vessels by thickening of the coats of these vessels.* Afterwards, when he had the occasion to perform an autopsy on a two-year old child he wrote: *here I found everything the contrary to what it was in the case of the old man.* From this text it is clear that Leonardo finds in the old patient an increased arterial stiffness and stenoses, which are missing in the young patient. He identifies in the aging a cause of the vessel wall degeneration because the *coat of the vessels acts in man as in oranges, in which the peel becomes thicker and the pulp diminishes the more they become old.* And attempts an explanation in the fact that *a thing which is nearer to that which feeds it increases more, and for this reason, these vessels being a sheath of the blood that nourishes the body it nourishes the vessels so much the more as they are closer to the blood*, reminding the role of cholesterol in the thickening of the intima [1].

The direct visualization of the arterial tissues allowed Leonardo to anticipate of several centuries the knowledge of the arterial physiopathology but he didn't understand that the blood was in a circulatory system. He went along with the belief (commonly held at the time) that blood was made in the liver, cooled in the lungs, pumped by the heart and consumed in the muscles [2]. Instead of (directly) examining the arterial system with an autopsy (in the XVI century it was probably the only option), current medical imaging provides a more powerful and non-invasive modality, and if, integrated with the computational analysis (i.e. image-based analysis), allows replicating in silico the in vivo case of interest. This dissertation reports the technological improvements in the vascular image-based analysis developed during a four-year research activity.

Chapter 1. Introduction

Cardiovascular diseases are the world's largest killers and represent the cause of 48% of all deaths in Europe [3,4]. One of the most common cardio-vascular diseases is atherosclerosis, which often leads to narrowed (stenosed) arteries and to thrombo-embolic events, compromising the perfusion of the downstream tissues.

Despite a systemic risk, atherosclerosis manifests itself in large arteries as geometrically focal plaques, with a local alteration of the anatomy, the histology and the mechanical properties of the diseased vessel wall. The endothelial monolayer, in the tunica intima, is in direct contact with the blood and bears most of the wall shear stress (WSS), which is the frictional force arising from the flowing blood. Endothelial cells sense the blood shear forces and may react to it by promoting either the vascular homeostasis or remodeling. The mechano-sensitive role of endothelial cells explains the local occurrence of the atherosclerotic manifestations in the outer edges of the vessel bifurcations and in regions of marked curvature. There, a flow disturbance may cause a low and oscillating WSS, which, in turn, may promote an atheroprone endothelial phenotype and the formation of a plaque.

Current imaging technologies (ultrasounds, biplane angiography, rotational angiography, computer tomography, magnetic resonance imaging, optical coherence tomography and intravascular ultrasounds) are largely used in clinical practice to visualize the blood vessels in vivo, enabling the diagnosis and treatment of a stenosis. More recently, a virtual window on the in vivo blood flow and arterial wall mechanics has been opened with the advent of image-based analysis, offering a unique tool to investigate the existing in-vivo hemodynamics and predict the outcomes of a vascular intervention (e.g. stenting).

Because the partial differential equations that govern the fluid flow and arterial wall mechanics do not offer in general an analytical solution, the image-based computational domain is split into subdomains, called mesh elements or cells, in which the governing equations are discretized and solved. Different primitives, such as hexahedrons, tetrahedrons and prisms, may be used for the volume discretization (i.e. the mesh generation) but the type, the size, the shape quality, the topological arrangement and the orientation of the elements should be chosen with care because they influence the accuracy of the numerical solution. The mission of this thesis is to improve the mesh generation method for image-based analysis of blood vessels, with a specific focus on structured hexahedral meshes, which provide a high accuracy of the computed parameters with a low computational cost.

Chapter 2. Effect of the volume discretization on the coronary flow computation: a case study

As a first case, an arterial tree with tubular branches is considered: a left coronary artery reconstructed from a biplane angiography and modeled with circular sections aligned along centerlines. The complex arterial structure is partitioned into a number of simpler parts, being straight vessels and vessel bifurcations. After reconstructing the surface of each part by means of longitudinal Bézier splines, an isoparametric transformation is used to map a structured hexahedral block (i.e. a Cartesian grid) into several sub-regions of the lumen. All these blocks are then merged, resulting in a high-quality multi-block structured hexahedral mesh of the coronary lumen, suitable for a CFD (computational fluid dynamics) analysis. This mesh is conformal and its topology reproduces the branching and twisting of the branches, allowing meshing multiple non-planar bifurcations. The cells and the cells' edges are aligned along the vessel centerline, which approximates the predominant flow in a nearly-straight branch, and can be layered in the radial direction to capture the high velocity gradient.

To compare the newly generated meshes to the most common automatically-generated meshes, a series of structured hexahedral meshes and a series of unstructured hybrid meshes of tetrahedrons and prisms are tested for the calculation of the WSS using a CFD analysis. When considering the same coronary artery and the same boundary conditions, a structured mesh is found to require a lower number of elements to obtain a mesh-insensitive WSS (within a desired tolerance), enabling a more accurate, faster and less memory-demanding computation. This finding suggests that the use of structured meshes may be beneficial for an image-based analysis and motivates further methodological developments of the mesh generation in image-based arterial domains.

Chapter 3. Bifmesh: hexahedral mesh generation in a nearly-planar bifurcation

The 'experiment' of the coronary artery suggests that the generation of a hexahedral mesh is feasible, may improve the computation, but also requires an extensive operator intervention, from the partition of the domain into simpler subdomains and the construction of the splines around the lumen to the mesh mapping. The need to simplify the procedure brings to the graphical implementation of a meshing tool, the vascular BIFurcation MESHer or Bifmesh. By devoting the applicability of the method to a single nearly-planar bifurcation, represented as a triangulated surface model (STL), the input required by the user is drastically reduced, allowing generating a structured hexahedral mesh with few clicks on the monitor

and within two minutes.

A carotid artery bifurcation is chosen as a test case for the implementation of the tool. First, the surface is sliced by means of planes, converting the STL into a series of sections. To do it, the user needs to select few points around the vessel in order to apply a standard bifurcation topology to the patient-specific bifurcation geometry. Then, as for the coronary artery, longitudinal splines are used to reconstruct the vessel lumen but are now generated automatically. Based on the splines and on the centerlines of a branch, an isoparametric transformation is used to map a 2D Cartesian grid in the vessel cross-sections, generating a series of topologically-equivalent quadrilateral meshes. By connecting these meshes, a volume mesh is generated in a branch. After repeating the operation for the other two branches, a structured hexahedral mesh of the lumen of a carotid artery bifurcation is generated. Additionally, the arterial wall can also be meshed in the same way, after reconstructing the outer wall surface either by image segmentation or by expanding the lumen surface. Remarkably, the exact number of elements in the lumen and in the wall can be defined *a priori*, by setting few parameters to design the mesh with the desired mesh resolution. The lumen and wall mesh generated with the Bifmesh can be used for CFD and FEA (finite element analysis) investigations, respectively.

Chapter 4. Treemesh: multi-block hexahedral mesh generation in a complex vascular tree

When the image-based vascular research is oriented towards complex arterial territories and pathological cases, the domains of interest often include bifurcations, trifurcations, n-furcations, stenoses and aneurysms. The topology and the geometry of such domains complicate the definition of the structure of the mesh. As such, the development of a general methodology to facilitate the mesh generation is a challenging task. For this purpose, the vascular-TREE MESHer or Treemesh, a meshing framework potentially applicable to all kind of vascular networks, is developed. Instead of imposing a predefined topology, the user can specify the topology of the mesh by inserting few blocks inside the vessel lumen. The centerline-based descriptors of the vasculature, as defined in the Vascular Modeling Toolkit (VMTK), are taken as a skeleton for the construction of the blocks. Then, based on these blocks, an isoparametric transformation and a projection operation are used to fit a multi-block structured mesh into the lumen. The boundary of the lumen mesh reproduces the initial surface model with a sub-micrometric accuracy, thanks to a projection operation. After generating the lumen mesh, the wall mesh can also be generated. When not provided, the outer wall surface can be reconstructed based on the local vessel size and anatomical data. Indeed, at each location of the lumen surface the distance from the

centerline can be computed (the distance from the centerline is equivalent to the radius in a perfect cylinder) and used to assign a location-dependent wall thickness. As for the Bifmesh, a set of parameters provide the user with the possibility of designing the mesh, choosing the number of elements in the longitudinal, circumferential and radial direction. In the vessel wall, different materials can be assigned to the arterial tunicae (intima, media and adventitia) and a material anisotropy can be implemented to take into account the role of the collagen fibers that reinforce the living arterial tissue. From two test cases, a human aortic arch and an abdominal aortic aneurysm, the Treemesh appears a robust and powerful tool to generate high-quality meshes for image-based computational analysis, but its larger applicability/generality as compared to the Bifmesh is paid with a longer mesh-construction time.

Chapter 5. Real case applications of the Bifmesh and the Treemesh

Both the Bifmesh and the Treemesh can be applied to biomedical research, in the fields of CFD, FEA and fluid-structure interaction (FSI). Chapter 5 provides an overview of the initial (published) contributions of the new meshing methodologies.

The ease of the mesh generation using the Bifmesh can be found in the investigation of

- the swirling design of an arterio-venous graft for hemodialysis for the improvement of the hemodynamics in the venous anastomosis;

- the structural performance of different self-expanding stents in a patient-specific carotid artery bifurcation;

- the structural performance of different balloon-expanding stents using a parametric coronary bifurcation as a bench test.

The flexibility and generality of the mesh generation using the Treemesh is reported in

- a retrospective investigation of the aortic hemodynamics in five mice which developed an aneurysm;

- the quantification of the impact of different strategies of imposing in vivo measured boundary conditions on two human aortic arches;

- a computational and experimental study to assess the accuracy of FEA to simulate coronary bifurcation stenting;

- a multiphysics investigation of the wall motion of a carotid artery bifurcation to test ultrasound imaging algorithms.

These applications of the framework (and others ongoing) at one year time from the development of the framework confirm the usefulness of the Bifmesh and Treemesh for image-based mesh generation.

To facilitate computational demanding simulations, a strategy to insert transitional blocks in the mesh generated with the Bifmesh and Treemesh is implemented, in order to increase or decreased the number of elements in a vessel cross-section, maintaining a conformal mesh. In such a way, the mesh resolution outside the region of interest can be lowered, reducing the run time and the memory required for the computation and facilitating the post-processing.

Chapter 6. A computational investigation of the hemodynamics after carotid artery stenting

Simulating carotid artery stenting using image-based FEA has the potential to predict the stented-vessel geometry, taking into account the patient-specific vessel and the specific stent model, as shown in Chapter 5 (an application of the Bifmesh). From the post-stenting finite element model, a CFD analysis can be performed to predict the hemodynamics that would establish immediately after stenting. An open-cell stent model, resembling a commercially available device, is deployed in a patient-specific carotid artery using a FEA. From the deformed vessel and stent, a 'negative' of the structure is reconstructed to delimit the physical domain of blood. Based on average data reported in literature, a pressure waveform is applied to the inlet, on the common carotid artery, while impedances are imposed at the outlets, on the internal and external carotid arteries. Such boundary conditions are believed, in a first approximation, to be insensitive to the presence of the stent and to the modification of the shape of the vessel.

The WSS map identifies critical regions nearby a mild stenosis, where stent-to-vessel malapposition occurs, distal to the stent strut interconnections and in the ostium of the external carotid artery, were floating struts disturb the blood stream. The CFD analysis based on an image-based FEA represents a suitable tool to forecast the outcomes of a patient-specific stenting from both a structural and flow perspective. In future, it may provide a clinician with realistic post-stenting hemodynamic scenarios and help him to select the most appropriate device, either for clinical applications or for training.

Chapter 7. Conclusion

The last chapter of the dissertation includes an overview of the major findings of this research with respect to the initial mission. Future extensions for both the Bifmesh and the Treemesh, are suggested, based on the obtained results and ongoing applications.

Chapter 1

Introduction

THE blood vessels are the part of the circulatory system that transports blood throughout the body. There are three major types of blood vessels: the arteries, which carry the blood away from the heart; the capillaries, which enable the exchange of water and chemicals between the blood and the tissues; and the veins, which carry blood from the capillaries back toward the heart [5]. Moving away from the heart, the blood vessels decrease in size and increase in number, constructing a tree-like transport system. The tree-like topology saves material for building the vessels' wall and energy for the transport of blood as compared to a parallel topology (constant size and no branching), which is typical of the peripheral nervous system. A consequence of this hierarchical organization of the vascular system is that the blood vessels have a priority which depends on the topological distance from the heart: occluding one large artery has the same effect of occluding all its daughter branches, impairing the perfusion of a large portion of the human body (exceptions are the redundancies offered by collateral vessels, such as in the Circle of Willis).

Vascular diseases, such as atherosclerosis, may lead to the occlusion of large arteries and have been associated to abnormal flow conditions, attributing to the (local) hemodynamics a key role for the vessel-tissue mechano-biology [6]. As such, the assessment of the in vivo hemodynamics and vessel mechanics is of interest for the bio-medical research. Image-based computational analysis is a powerful tool to assess the structural and fluid mechanics in vivo and represents a suitable alternative to direct measurements, which are still limited despite the current technological advances. A challenging step in the image-based analysis is the generation of a high quality computational mesh from medical images to allow an accurate patient-specific analysis of vascular regions.

This chapter begins with the assessment of the impact of atherosclerosis and provides a link between vessel physiopathology and blood flow using a model of atherogenesis. Then, an image-based analysis for the assessment of in vivo blood flow and vessel stress state is presented, with a strong focus on the mesh generation. The last part of the chapter defines the aim of the doctoral research and presents the organization of the dissertation.

1.1 Atherosclerosis

1.1.1 Socio-economic impact

Cardiovascular diseases are the world's largest killers, claiming 17.1 million lives a year, and represent the cause of 48% of all deaths in Europe [3, 4]. One of the most common cardiovascular diseases is atherosclerosis, which often leads to narrowed (stenosed) arteries and to thrombo-embolic events, compromising the perfusion of the downstream tissues.

1.1.2 Arterial physiopathology

Despite the systemic nature of known clinical risk factors (e.g. cholesterol, genetic inheritance, alcohol, tobacco, unhealthy diet, sedentary life), atherosclerosis manifests itself in large arteries as geometrically focal plaques, with a local alteration of the anatomy, the histology and the mechanical properties of the diseased vessel wall [6].

Large healthy arteries have a tubular structure with a trilayered wall: tunica adventitia, tunica media and tunica intima, moving radially inward. In general, the adventitia contains connective tissue, with collagen fibers arranged as a counter-rotating helical system, and protects the vessel in case of large deformations. The media contains smooth muscle cells, collagen fibers and elastine, and is responsible for the compliance of the artery during the cardiac cycle, accumulating and releasing energy in response to blood-pressure variations. The intima consists of a monolayer of endothelial cells that faces the flowing blood, provides an antithrombogenic surface, and regulates the transport of macromolecules from the blood into the outer layers of the vessel wall. In coronary arteries, the thickness of the intima is comparable to the thickness of the other tunicae [8]. The internal elastic lamina, a layer of elastic tissue, separates the intima from the media (Fig. 1.1). The biological composition and thickness of the tunicae are layer-specific and vessel-specific, providing a broad range of mechanical properties. It is known that arterial tissue behaves as a non-linear and
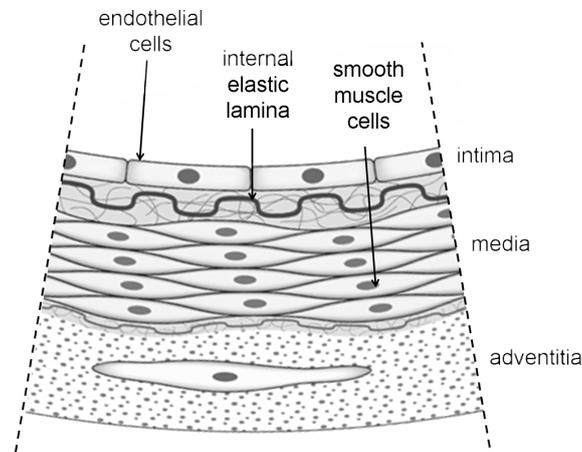
Figure 1.1: Sector of a cross-section of an artery showing the layered structure of the arterial wall (adapted from [7]).

anisotropic material, mainly due to the heterogeneous composition of the arterial wall which resembles a fiber-reinforced matrix.

Early manifestations of atherosclerosis are fatty streaks appearing on the arterial wall of children. Atherosclerosis remains asymptomatic for decades [9], while an arterial thickening is being compensated by an outward remodeling. According to the accepted paradigm for atherogenesis, the internal elastic lamina, which represents a barrier between media and intima, is gradually disrupted, due to injury produced by macromolecules such as low-density lipoproteins (LDL), and medial smooth muscle cells migrate through fenestrations into the intima. These cells proliferate and produce new extracellular matrix, thus increasing the plaque volume [9–13]. The complications of advanced atherosclerosis manifestations are chronic, slowly progressive and cumulative. Inflammatory reactions following the plaque initiation may result into a vulnerable plaque, which includes a lipid pool, a necrotic tissue and a thin fibrous cap. When invading the lumen, a plaque limits the blood supply to the downstream tissues (it increases the hydraulic resistance of the vessel), causing ischemia (Fig. 1.2). Additionally, the fibrous cap of a plaque may rupture, exposing thrombogenic material, such as collagen, to the circulation and eventually inducing the formation of a thrombus in the lumen [14] (Fig. 1.3). Upon formation, the intra-luminal thrombi can occlude an artery outright (i.e. coronary occlusion), but more often they detach, move into the circulation and eventually occlude smaller downstream branches (e.g. stroke is often caused by thrombo-embolic events occurring in the carotid arteries) [15].
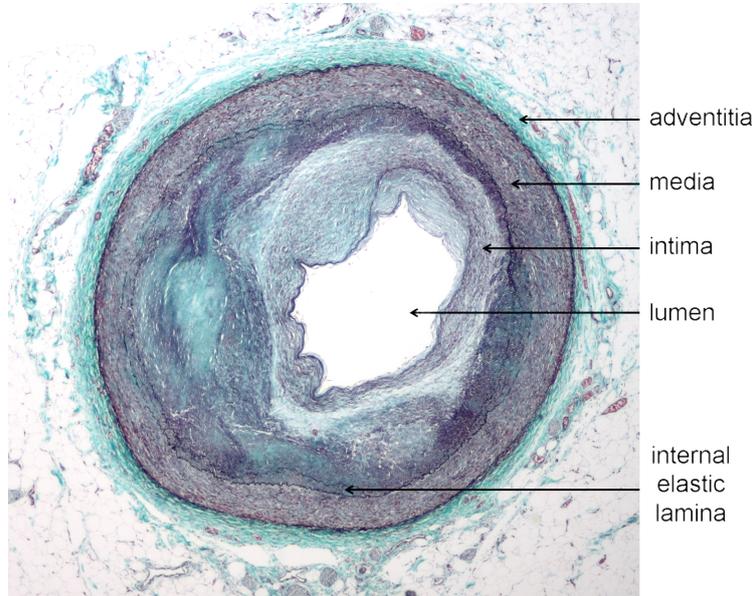
Figure 1.2: The cross-section of a stenosed coronary artery displays a severly thickened intima, a fragmented internal elastic lamina and a significant lumen narrowing. The original lumen corresponds approximately to the internal elastic lamina (adapted from [15]).
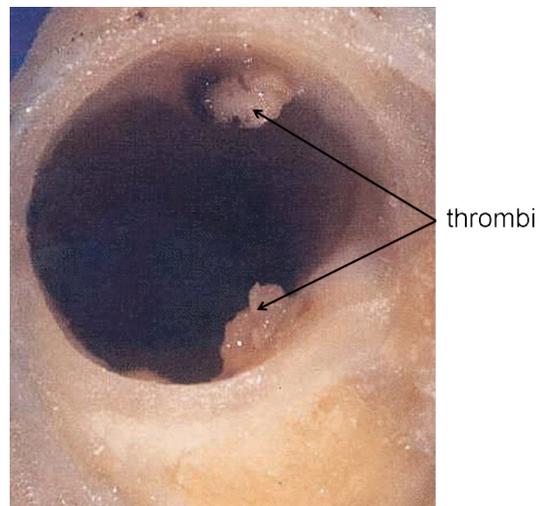
Figure 1.3: Two mural thrombi protrude into the lumen of a coronary artery (adapted from [16]).

1.1.3   Model of atherogenesis

Blood vessels are subjected to various types of hemodynamic forces (including hydrostatic pressure, cyclic stretch, and fluid shear stress). The endothelial monolayer is in direct contact with flowing blood and bears most of the wall shear stress (WSS), which is the frictional force arising from blood flow and acting parallel to the luminal surface (Fig. 1.4). Endothelial cells sense the blood shear forces and may react to it either by promoting the vascular homeostasis or by remodeling. The mechano-transduction of endothelial cells has been largely investigated both in vitro and in vivo using different blood flow conditions [17]. Local fluid shear stress has been found to modulate an atheroprotective or atheroprone endothelial phenotype, promoting a diverse gene expression [18]. If subjected to sustained and monodirectional WSS, endothelial cells appear elongated in the direction of the WSS, show long and parallel stress fibers in the cell cytoskeleton and tend to migrate and tightly pave the arterial lumen, thus reducing the endothelial permeability. Conversely, when exposed to low and oscillating shear forces, endothelial cells appear round, polygonally shaped [19], do not show stress fibers, show a low tendency to migrate and have a high permeability due to large fenestrations in the endothelium [19–23] (Fig. 1.5). In such a system, the WSS acts on the inner side of the intima on a cellular scale (nm-micron), and induces a mechano-biological response on a tissue scale (cm-dm)[1].

Atherosclerotic plaques preferentially affect the outer edges of vessel bifurcations and regions of marked curvature [6, 25], where flow disturbances are likely to occur, as suggested by clinical and postmortem studies [26–29]. A comparison of these locations with the map of the WSS on the inner side of the arterial wall in vivo has shown a topological correlation between low or oscillating WSS and plaque formation, suggesting a model of atherogenesis based on the WSS [6, 30, 31]. A possible explanation for this correlation is an increased permeability of the endothelium observed in case of low and oscillating WSS, which results in an increased uptake of macromolecules like LDL [32]. The shear-induced atheroprone/atheroprotective endothelial phenotype (i.e. the model of atherogenesis [6]) has stimulated extensive research, and the hemodynamic characterization of the arterial flow in vivo is considered to be important to understand the arterial biology/pathobiology

---

[1] A model of cell mechano-transduction was published in the journal, European Cells and Materials:
**How can cells sense the elasticity of a substrate? An analysis using a cell tensegrity model**
G. De Santis, A. B. Lennon, F. Boschetti, B. Verhegghe, P. Verdonck, and P. J. Prendergast
in press (available online)
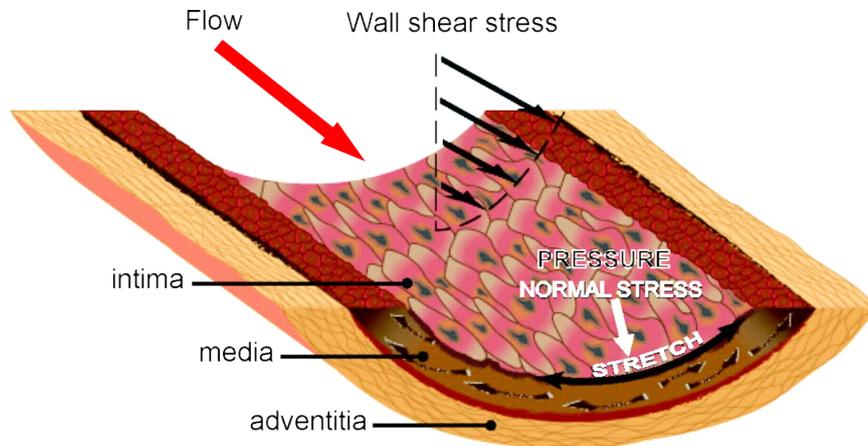
Figure 1.4: WSS and pressure acting on the arterial endothelium (adapted from [24]).
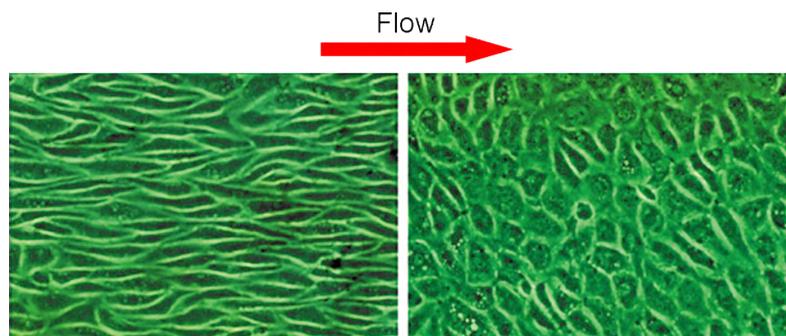
Figure 1.5: Change of the shape of the endothelial cells in response to a physiologic (left) or a low (right) shear stress (adapted from [6]).

in health and disease [6, 24]. Although arterial blood flow may reasonably be considered laminar throughout the vascular system, the flow patterns and hemodynamic forces are not uniform. In straight parts of the arterial tree, blood flows in the direction of the vessel centerline and WSS is high and directed. In branches and curvatures the blood flow is complex, including zones of recirculation and secondary flow, with a non-uniform and irregular distribution of low WSS. A sustained laminar flow with high WSS upregulates the expressions of endothelial cells' genes and proteins that are protective against atherosclerosis, whereas a disturbed flow with associated reciprocating, low WSS generally upregulates the endothelial cells' genes and proteins that promote atherogenesis [24]. These findings have led to the concept that the disturbed flow pattern typical of branch points and cur-

vatures causes the preferential localization of atherosclerotic lesions [6, 24]. The role of the endothelial WSS in the arterial remodeling was elegantly demonstrated by Carlier et al. [33] who noticed a decrease of the intimal hyperplasia in arteries of pigs at the locations where the WSS was increased by the insertion of a flow divider. Quantitatively low and oscillating WSS (< 0.4 Pa) is atherogenic while high WSS (> 1.5 Pa) is atheroprotective and induces endothelial quiescence [6]. An overview of the current knowledge on vascular mechano-biology from a cellular to a tissue scale is reported by Chiu and Chien [24].

1.1.4 Image-based Computational Fluid Dynamics

The model of atherogenesis represents a straightforward criterion to assess the distribution of the atherogenic risk in a vascular district and can improve the diagnosis and therapy of atherosclerotic plaques. In order to apply the model of atherogenesis in a patient, accurate flow data are required. However, direct measurements of the arterial flow in vivo are difficult because the current technologies are often limited to superficial vessels and do not offer sufficient spatial resolution to quantify important parameters such as the WSS (e.g. Doppler Ultrasound and phase contrast MRI [31, 34–37]) which, being a differential quantity, needs an accurate estimation of the velocity in the vicinity of the wall [38]. From the late 1990s, by taking advantage of the fast development of the imaging techniques (3D Ultrasound, biplane angiography, CT, MRI and rotational angiography), the morphologies of patient-specific vascular domains have been used to simulate in vivo blood flow by means of Computational Fluid Dynamics (CFD) [39–46].

For an image-based analysis four steps are required in order to obtain a WSS map from a 3D image: (a) segmentation, to extract the arterial surface from medical images, (b) volume meshing, to discretize the flow domain, (c) CFD computation and (d) post-processing [46]. Segmentation and patient-specific meshing represent additional complications for the image-based CFD compared to CFD performed on an idealized geometry. Tools for (semi)automatic segmentation are available as open source (e.g. Vascular Modeling Toolkit (VMTK) [39, 47]) or commercial (e.g. Mimics, Materialize [48]) software packages and usually return the arterial geometry as a triangulated surface model (STL) which describes the boundary of a flow domain. Because the partial differential equations (PDE) that govern the fluid flow (i.e. the incompressible Navier-Stokes equations) do not offer in general analytical solutions, the flow domain is split into subdomains in which the governing PDE are discretized and solved. Both the finite element method and the finite volume method can be used to solve the system of equations numerically, but latter is the most used in vascular applica-

tions. Care must be taken to ensure proper continuity of the solution across the common interfaces between two subdomains, so that the approximate solutions inside the various portions can be put together to give a complete picture of the fluid flow in the entire domain. The subdomains are often called elements or cells, and the collection of all elements or cells is called a mesh or grid.

1.1.5   Image-based Finite Element Analysis

Next to the application in hemodynamic research, image-based analysis has shown the potential to predict the structural mechanical behavior of the arterial wall by means of the Computational Structural Dynamics (CSD). In the rest of this dissertation, Finite Element Analysis (FEA) will be used to indicate a CSD analysis. The mechanics of the arterial tissue is characterized by a non-linear stress-strain relation due to large displacements/deformations, and non-linear elasticity (hyperelastic and fiber-reinforced material model) [8]. In order to assess the patient-specific mechanics of a vessel, Kiousis et al. integrated the geometry of a carotid artery model reconstructed from medical images with a non-linear material model of the arterial tissue, including calcification, lipid core and fibrous plaque, to estimate the stress distribution in a realistic pressure loading condition [49]. In silico models have also been used to investigate the stenting intervention based on a patient-specific vessel geometry and a prosthesis-specific design. To mention a few examples, balloon-expandable stents have been virtually deployed in a coronary bifurcation [50], self-expanding Nitinol stents have been inserted both in a carotid artery [51,52], and in an aneurysm [53], pulmonary stented valves have been implanted in the right ventricular outflow tract [54].

More recently, image-based analysis has been performed on both the lumen and the wall of blood vessels, combining CFD and FEA, in order to capture in silico the interaction between the compliant arterial wall and the moving blood. The Fluid-Structure Interaction analysis (FSI) has been applied to the aortic arch [55] and the abdominal aortic aneurysm [56,57].

From a technological perspective, the cost of the pre-processing phase, and the volume mesh generation in particular, for image-based vascular modelling is independent of the application (CFD, FEA or FSI) and is directly related to the geometrical complexity of the vessel.

1.1.6   Types of mesh

The mesh elements are geometric primitives, such as **tetrahedrons**, **hexahedrons** and (less common) **prisms** (see Fig. 1.6) with different geomet-

rical and topological properties, as reported in Table 1.1.

Few definitions are required for the classification of a mesh. A **structured** mesh is characterized by a regular connectivity that can be expressed as a three dimensional array (in practice, only hexahedrons are used in structured grids). An advantage of a structured mesh is the regularity of the connectivity matrix, which allows detecting neighborhood relationships by checking the storage arrangement. An **unstructured** mesh is characterized by an irregular connectivity which cannot be readily expressed as a three dimensional array. Compared to structured meshes, the storage requirements for an unstructured mesh can be substantially larger since the neighborhood connectivity must be explicitly stored. A **multi-block structured** mesh is an unstructured collection of structured blocks. Thus, this mesh is composed of several domains and each domain is a structured mesh. For conciseness, we will use 'structured' instead of 'multi-block structured' in the rest of this dissertation. Hexahedral, prismatic and tetrahedral meshes can all be unstructured. A mesh is **conformal** if it respects two conditions: (1) the intersection between any two elements is a sub-element of both elements (a face, an edge, a node or none) and (2) the maximal dimensional shared sub-element is only one and complete (see Fig. 1.6).

Table 1.1: Features of the most common types of mesh elements. A tetrahedron (TET), a prism and a hexahedron (HEX) contain an increasing number (N) of sub-elements (nodes, edges and faces). The faces of a tetrahedron and a hexahedron are four triangles and eight quadrilaterals, respectively. A prism contains both triangular and quadrilateral faces.

Element type	N of nodes	N of edges	N of faces	Face angles
TET	4	6	4	$120°$
Prism	6	9	5	$90° - 120°$
HEX	8	12	6	$90°$

The process of obtaining an appropriate mesh has long been considered a bottleneck in the image-based analysis process, until dedicated software programs were developed for the purpose of automatic mesh generation. A volume can be discretized into tetrahedral elements starting from the boundary surface by using algorithms such as the Delaunay tetrahedralization [58]: a volume is seeded with source points, the Voronoi diagram is constructed (around a source point a convex polygon defines the region closer to that source point than to any other source point) together with its dual, the Delaunay tessellation, which in the 3D space is a tetrahedral mesh [59]. Prismatic elements are generally not used in the full computational domain,
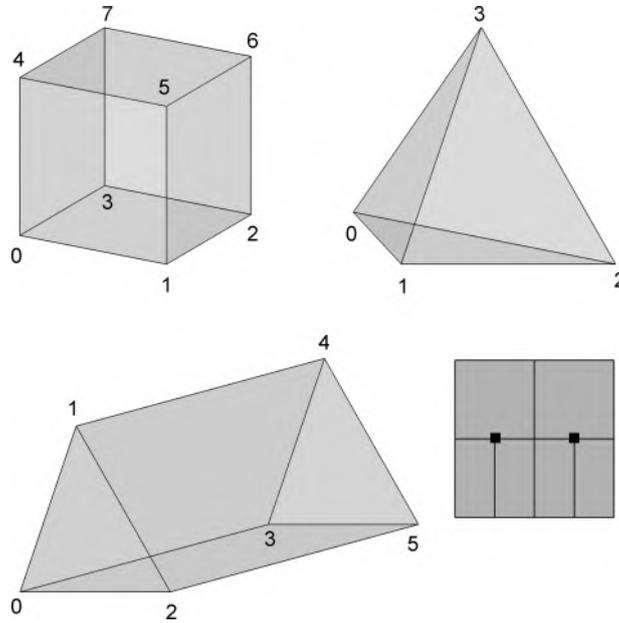
Figure 1.6: The most common mesh element types: (top-left) a 8-node hexahedron, (top-right) a 4-node tetrahedron, (bottom-left) a 6-node prism (or wedge). The number of nodes per element can be increased by introducing additional nodes on an edge or a face, generating a high-order element. (bottom-right) An example of a non-conformal quadrilateral mesh in which the maximal-dimensional shared sub-element between a larger element on the top and a smaller element on the bottom is one but is not complete (half of an edge of the larger element), producing two hanging nodes (dark points).

as they expose two kinds of faces (triangles and quadrilaterals) which may give rise to a non-conformal grid. As the velocity near the arterial wall is of great interest for hemodynamics (e.g. WSS), it is often preferred to increase the mesh density near the wall with elements aligned in parallel with respect to the boundary surface. In practice, this is achieved by extruding the surface triangles into the flow domain, producing one or more layers of prismatic elements [39]. Such hybrid meshes (tetrahedrons in the bulk and prisms near the wall) can be generated automatically and represents the standard approach in current applications of image-based CFD. Structured hexahedral meshes are less common because they are difficult to generate, due to the topological constraints of a hexahedral element (i.e. a hexahedron has eight neighbors by face) and because of the lack of algorithms that enable to automatically decompose a general volume domain into block-meshable subdomains. As a result, conformal structured meshes have been rarely generated for image-based analysis in case of branching vessels.

1.1.7 State of the art in structured mesh generation for image-based modeling of branching blood vessels

Different methodological approaches to structured mesh generation starting from a surface model of the vessel anatomy have been proposed. The first successful attempt to generate a structured mesh in a carotid artery bifurcation was reported by Long et al. in 1998 [60]. These authors have reconstructed the surface of the arterial lumen by means of four sets of longitudinal splines. By interpolating between the splines and the centerlines, a number of hexahedral cells were generated in the lumen. The result was a mesh suitable for CFD analysis, topologically equivalent to the union of three **sweeping**-based meshes, one per branch (a sweeping-based mesh, or 2.5D mesh, is obtained by sweeping a 2D mesh along a path). This approach was modified by Antiga et al. [61], who added an ad hoc group of cells in the middle of the bifurcation in order to improve the mesh quality (see section 1.1.8). An original strategy was developed by Verma at al. [62]: starting from the lumen surface, an unstructured tetrahedral mesh was constructed to simulate additional heat conduction problems in the bifurcation. The resulting isothermal surfaces represented a set of non-intersecting vessel sections aligned longitudinally. Each section was then meshed with a quadrilateral grid and, on each branch, the quadrilateral grids were interconnected, generating a sweeping-based mesh of the CFD domain. This mesh was topologically similar to the mesh generated by Long et al. but the amount of operator interaction necessary to generate it was significantly reduced. Instead of directly constructing a sweeping-based mesh on the complex patient-specific geometry, Wolters et al. defined a template of a standard bifurcation (a sweeping-based mesh model) and deformed it to fit the vessel lumen (**mapping**-based mesh [56]). By displacing the surface nodes outside the lumen surface by a constant distance to create the outer vessel surface, a structured mesh in the wall was also generated. However, highly deformed elements appeared in the bifurcation regions due to the mapping operation, requiring multiple smoothing operations in order to improve the mesh quality for an FSI analysis. These four bifurcation meshing methods are shown in in Fig. 1.7 . Because of to the fact that meshing the lumen is more challenging than meshing the wall, several authors have simplified the methodology proposed by Long et al. and adapted it to mesh the wall-only for FEA [49, 63, 64].

With the exception of a single bifurcation, the structured mesh generation in a topologically complex vascular district is still unexplored. All the previously cited methodologies would fail in case of a vessel with multiple non-planar bifurcations or general branching patterns (trifurcations, n-furcations). Zhang et al. have proposed a methodology to generate
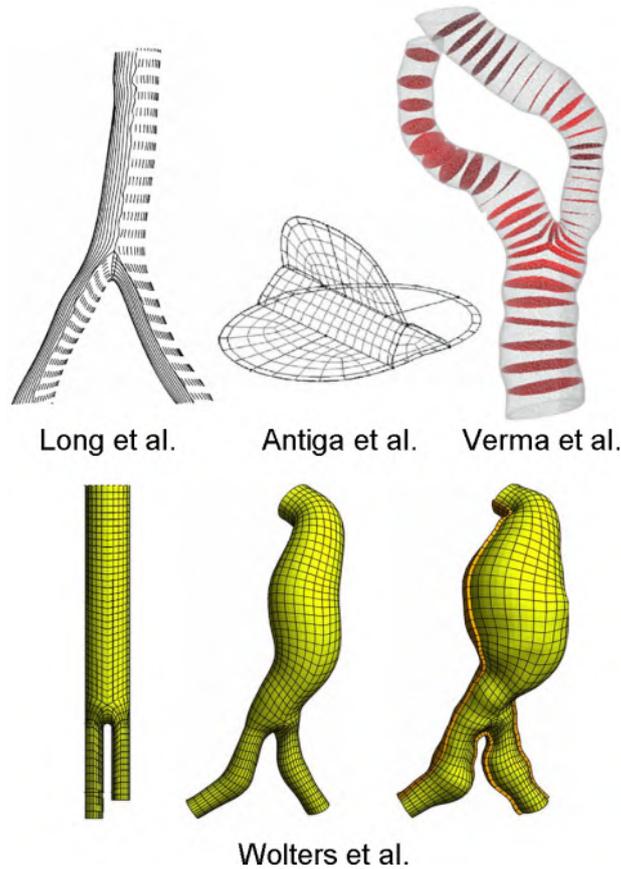
Figure 1.7: An arterial bifurcation mesh can be constructed using four sets of longitudinal splines [60] (top-left), a central structure to connect three branches [61] (top-center), isothermal-based cross-sections [62] (top-right) or deforming a standard bifurcation model [56] (bottom).

hexahedral-dominated structured meshes by combining parametrically-defined branching templates with sweeping-based meshing. The branching templates were specific to the branching topology and could be used to mesh all kinds of branching regions. Sweeping was used to mesh the non-branching portions of the vessel. Because of the axial-symmetric mesh of the vessel cross-section, required to interconnect the sweeping-based mesh with the template-based mesh, prisms were generated along the centerlines, obtaining a hybrid mesh for isogeometric analysis of blood flow (see Fig. 1.8).

Despite the above mentioned contributions, the use of structured meshes in image-based research is rare and often limited to one single case as a proof

of feasibility. The low impact of these mentioned methodologies can be ascribed to a lack of generality (e.g. applicability to one single bifurcation only), difficulty of the procedure as compared to automated unstructured mesh generators, long user interaction and difficulty to correct highly distorted elements. Details on the sweeping and mapping algorithms are available in [55, 65–70].
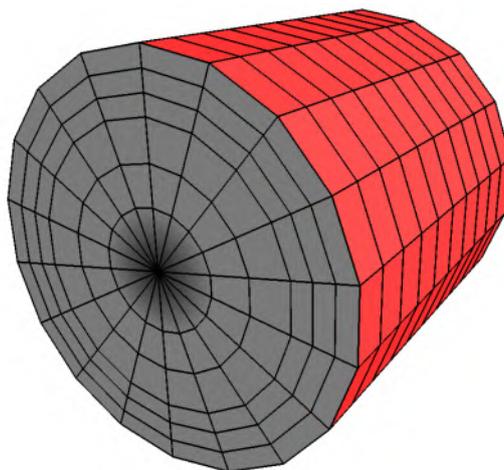
Figure 1.8: By sweeping or extruding a 2D mesh of a section (quadrilateral or triangles) along a path, a volume mesh is generated (hexahedrons or prisms). If the sections is meshed using an axial-symmetric topology, the sweeping operation will produce prisms along the centerline and hexahedrons around the prisms [55].

1.1.8   Mesh quality metrics

A coarser and a finer mesh differ in the number of elements and nodes, which is indicative of the mesh resolution and affects the accuracy in the numerical integration of the PDE. The ratio between the number of nodes (in general indicating the degrees of freedom of the model) and the number of elements depends on the mesh topology and on the element type. As a proof of concept, we have generated a series of tetrahedral and hexahedral meshes into a sphere and estimated the elements-to-nodes ratio. Three resolutions have been considered, from 1,000 to 100,000 nodes for both the tetrahedral and the hexahedral mesh series, as shown in Figure 1.9. Approximately, a hexahedral mesh of N nodes contains 0.9N elements whereas a tetrahedral mesh of N nodes contains 6N elements. As a result, a hexahedral mesh allows reducing the number of elements by a factor 6.5 with respect to a tetrahedral mesh of similar nodal resolution (see Table 1.2).

The element shape influences the performance and the accuracy of the computation. This is ascribed to the integration of the PDE that describe the physical problem on a finite element. Indeed, the system of PDE is stiff (ill-conditioned) in case of a highly distorted element. As such, the computational solution will change rapidly (high sensitivity) in response to a small variation of the values of the coefficients and data of the system of PDE, and round-off errors may lead to an unrealistic solution or numerical instability (i.e. non-convergent simulation).

The quality of a mesh is generally quantified using the quality of its elements. In general, two different geometrical metrics are used for FEA and CFD: the scaled Jacobian and the equiangle skew. Considering the Jacobian transformation

$$\mathbf{J} = \partial\mathbf{X}/\partial\mathbf{U}$$

of a particular finite element from the physical domain $\mathbf{X} = \{X_1, X_2, X_3\}$ into its parent domain $\mathbf{U} = \{U_1, U_2, U_3\}$ the scaled Jacobian at a node k of an element can be calculated as the Jacobian (volume of the parallelepiped defined by the 3 edge vectors applied to node k) divided by the lengths of the 3 edge vectors:

$$SJ_k = \frac{\mathbf{e_{k1}} \cdot \mathbf{e_{k2}} \times \mathbf{e_{k3}}}{e_{k1} e_{k2} e_{k3}}$$

The scaled Jacobian of an element is the minimum nodal scaled Jacobian:

$$SJ = \min SJ_k$$

The scaled Jacobian can range from -1 (worst) to +1 (best, a rectangular hexahedron or cuboid) but elements with negative scaled Jacobian (i.e. inverted elements) are not recommended for analysis [64, 71, 72].

The parameter equiangle skew (Qeas) is often taken as quality index for CFD meshes and represents a normalized measure of skewness, ranging from 0 to 1. The Qeas depends on the angle formed between adjacent edges of each cell in the mesh (zero corresponds to a perfect equiangular cell):

$$Qeas = \max\left(\frac{\theta_{max} - \theta_e}{180 - \theta_e}, \frac{\theta_e - \theta_{min}}{\theta_e}\right)$$

where θ_{max} and θ_{min} are the largest and smallest angles in the cell and θ_e is the angle of the equiangular cell (see Table 1.1), which is 90° for hexahedrals and 60° for tetrahedrals (see Fig. 1.6). For prismatic cells,

θ_e is 90° for the three quadrilateral faces and 60° for the two triangular faces [61, 73, 74].
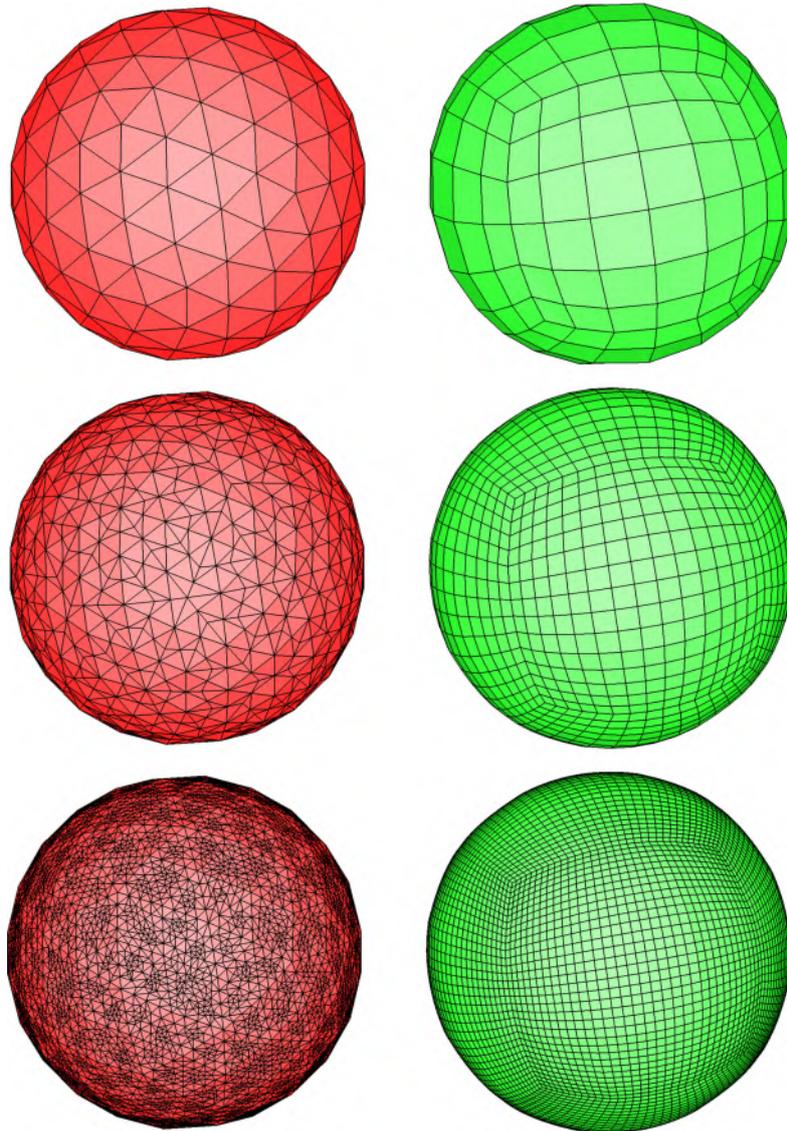
Figure 1.9: Three different nodal resolutions (course, medium and fine, from top to bottom), reported in Table 1.2, are used to mesh a sphere with tetrahedrons (left) and hexahedrons (right).

Table 1.2: The ratio of the number of elements and the number of nodes in a mesh does not depend on the resolution. In general, for the same number of nodes, a tetrahedral mesh (TET) requires 6.5 times more elements than a hexahedral mesh (HEX) independently of the mesh resolution.

Mesh of a sphere	TET (nodes)	HEX (nodes)	TET/HEX
Coarse (1 k nodes)	4418 (792)	648 (779)	6.71
Medium (10 k nodes)	64093 (10468)	10125 (10856)	6.56
Fine (100 k nodes)	723140 (115741)	107811 (111200)	6.44

1.2 Aim of the research

The mission of this doctoral research is to develop a framework for optimal-mesh generation dedicated to image-based analysis of vascular districts. An optimal mesh is the result of a trade-off between the cost of the mesh generation and the performance of the mesh in the computation. Therefore, both structured and unstructured meshes are generated, depending on the geometrical complexity of the vascular domain of interest. All the tools have been implemented in pyFormex [75], which is a python-based open-source software, currently under development at Ghent University, dedicated to create and to handle large geometrical models.

1.3 Outline of the dissertation

The dissertation is organized as follows:

- In chapter 2, the distribution of the WSS magnitude in a left coronary artery imaged with biplane angiography is computed. A series of multi-block structured meshes and a series of unstructured meshes, consisting of tetrahedrons in the bulk and prismatic boundary layers near the wall, are tested under identical geometrical and flow conditions. From a quantitative evaluation, structured meshes appear superior to unstructured meshes, because they provide mesh-independent WSS values with significantly fewer elements as compared to unstructured meshes, reducing the computational costs in terms of run time and memory.

- In chapter 3, a new structured mesh generator for image-based analysis of a single nearly-planar vascular bifurcation is developed (the Bifmesh). The code is embedded in the Graphical User Interface

(GUI) of pyFormex, reducing the complex structured mesh generation of the lumen and wall to few clicks on a mouse.

- In chapter 4, a robust procedure for structured hexahedral mesh generation in vascular districts is defined (the Treemesh). As a first step, a flexible geometrical and topological description of the vasculature is provided using centerlines. Then, based on the centerlines' attributes (local radius, local orientation), a structured mesh is fitted inside the vessel surface, with high geometrical accuracy. This methodology is then extended to generate a mesh in the arterial wall, including multi-layered element groups and allowing an anisotropic characterization of the elements.

- In chapter 5, a glance of the applications of the mesh generation frameworks (Bifmesh and Treemesh) is given. The applications have been grouped by the physics of the model: CFD (mouse abdominal aorta, human aortic arch, and graft for hemodyalisis), FEA (carotid and coronary artery stenting) and FSI (carotid artery). In all the mesh models used in these applications, the cross-sections of the vessel are characterized by a fixed mesh topology, which is the consequence of the topological constraints of a structured mesh. In the last part of the chapter, this limitation is bypassed by defining ad hoc transitional blocks (multi-block structured meshes) which allow a conformal refinement of the cross-section of part of a structured hexahedral mesh, enabling a higher flexibility in the design of the mesh (e.g. higher cross-sectional resolution in the region of interest).

- In chapter 6, the hemodynamic impact of carotid artery stenting is investigated using a full computational approach. After an image-based FEA simulation of carotid artery stenting, pulsatile blood flow in the stented carotid artery is simulated using CFD coupled with an impedance model. While the FEA was performed using a structured mesh of the stent and the arterial wall, the CFD was performed using an unstructured mesh: the complex geometry of the stent and the imperfect contact between the vessel and the stent make structured mesh generation unpractical in the flow domain of a stented vessel. The WSS-based descriptors are used to discriminate between atheroprotective and atheroprone post-stenting hemodynamics, applying the model of atherogenesis.

- Finally, in chapter 7, the original contributions of this research to image-based meshing are summarized and compared to the original objectives. The methodological improvements in mesh generation are considered from a perspective view towards future applications in different research areas and further developments.

Chapter 2

Effect of the volume discretization on the coronary flow computation: a case study

INVESTIGATING the local hemodynamics by means of CFD requires first to reconstruct and mesh the patient-specific vascular lumen. In Chapter 1, it was anticipated that (structured) mesh generation is a difficult operation because the arterial geometry appears all together in its complexity after segmentation and because of the inter-individual anatomical variability. However, it is critical for both the model accuracy and the computational cost. In this chapter, two mesh types, i.e. structured hexahedral and unstructured tetrahedral-prismatic meshes, are compared.

We consider a left coronary artery (LCA), imaged using biplane angiography and automatically segmented into groups of circular sections. First, we develop a strategy to map pre-meshed blocks inside the arterial lumen and generate a structured hexahedral mesh (multiple bifurcations and a stenosis are present in the domain). Then, under the assumptions of a rigid wall, a steady state flow and simplified boundary conditions, CFD analyses of the coronary flow are performed. A series of multi-block structured hexahedral meshes is generated by gradually decreasing the average cell volume in a parametric manner using the novel ad hoc meshing strategy. As a counterpart, a series of unstructured meshes including tetrahedrons in the bulk and prisms near the wall is generated using general purpose software packages. The two mesh types are tested under identical condi-

tions and evaluated using the mesh-independence of the computed WSS magnitude as indicator of accuracy and the CPU run time as indicator of the computational performance[1].

2.1 Introduction

The assessment of an atherosclerotic lesion (i.e. a stenosis) for clinical diagnosis is often based on the measurement of the local arterial lumen diameter from medical images. However, especially in coronary arteries, the simple mechanistic concept of diameter is incomplete, because the diameter analysis of stenosed arteries based on coronary angiograms may not be able to accurately assess the functional significance (i.e. impact on the blood flow) of that stenosis [76, 77]. In order to evaluate the severity of a stenosis, its hemodynamic impact rather than its geometrical appearance should be taken into account. For example, in case of collateral vessels, an anatomical blockage may be functionally unimportant but classified as severe stenosis based on a purely anatomical evaluation. Therefore, the fractional flow reserve (FFR, i.e. the pressure decline caused by a vessel narrowing) has been proposed as a reliable index to assess the severity of a coronary stenosis [77–79].

Coronary flow has been investigated with angiography-based CFD in a number of studies [36, 80–82]. Among the coronary imaging techniques, biplane angiography is the standard, whereas MRI and CT are currently restricted to a limited number of patients. Recently, biplane angiography has been validated with respect to CT and MRI for coronary surface reconstruction and flow estimation by Goubergirts et al. [80]. These authors have reconstructed a left main coronary bifurcation in a silicon model and imaged it using biplane angiography, CT and MRI. The original model and the data acquired using the three imaging techniques have been used for CFD simulations. No significant differences were found in the predicted values of mean WSS and WSS distribution, thus validating the biplane angiography-based reconstruction for WSS profiling of coronary arteries using CFD.

Despite the relative simplicity of assessing arterial flow with CFD (this holds for unstructured meshes), the simulated flow can be different from

---

[1] The content of this chapter was published in the journal, Medical and Biological Engineering and Computing:
Patient-specific computational fluid dynamics: structured mesh generation from coronary angiography
G. De Santis, P. Mortier, P, M. De Beule, P. Segers, P. Verdonck, and B. Verhegghe
48, 4:371-380, 2010

the original in vivo flow because of (among others) inaccuracies in the geometrical lumen reconstruction, as pointed out by Antiga et al. [39]. Lumen reconstruction typically requires a number of steps (segmentation, surface modeling and volume meshing) in which the patient-specific analysis risks to be masked by operator-dependent decisions, eventually resulting in an inaccurate flow simulation [83–85]. The level of operator interaction depends on the complexity of the arterial district of interest and may corrupt the repeatability of the analysis. To circumvent the segmentation process, we have taken the geometry as it was generated automatically from the segmentation software included in the angiographic scanner. This geometry, representing a left coronary artery (LCA), was used to develop a novel semi-automatic approach to generate structured hexahedral meshes. Structured meshes often require extra efforts compared to tetrahedral-prismatic meshes and their use has been limited to simplified or idealized vessel geometries [61, 86–89]. However, it has been suggested that they may be superior to unstructured meshes because of a possible alignment of the elements with the predominant flow [46, 83, 90]. In order to assess the value of the new mesh generation approach a series of structured hexahedral meshes (HEX series) was compared with a series of tetrahedral-prismatic meshes (TP series), both representing the same LCA. The WSS, rather than the velocity, has been pointed out as a highly mesh-dependent result and has been chosen as the parameter for comparison [91].

2.2 Materials and methods

2.2.1 Image acquisition and surface segmentation

A biplane angiogram of a LCA was acquired using the Allura 3D-CA machine [92] available at the Ghent University Hospital, Belgium, and currently used in clinical practice to visualize the coronary arteries. The segmentation software package was embedded in the scanner and was not directly accessible (black-box). Based on a validation of the segmentation algorithm of the angiographic scanner performed by Agostoni and collaborators [93], the output of the examination was considered accurate and suitable for image-based analysis of the patient-specific coronary anatomy: two projections (2D images) of the vasculature on nearly orthogonal planes were used to reconstruct the lumen surface model in VRML file format, which contained differently oriented circular sections lined up along the centerlines (see Fig. 2.1).

The open-source software pyFormex was used to implement the meshing process from the angiographic VRML file, in order to generate a structured hexahedral computational mesh of the patient-specific left coronary tree.

The modeling framework included three main steps which will be separately described: topological partition, geometrical surface reconstruction and mesh mapping.
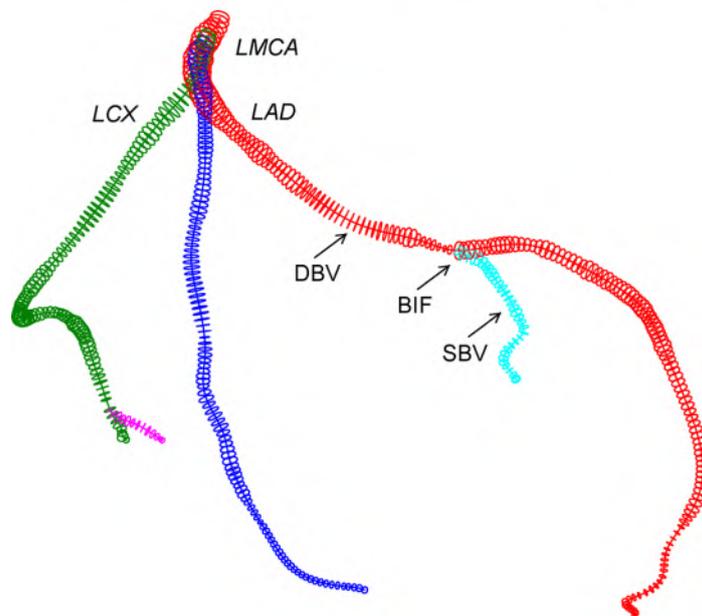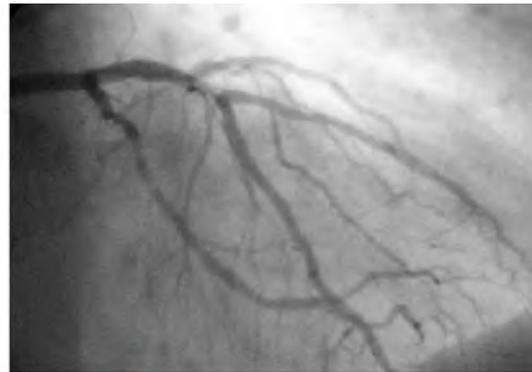
Figure 2.1: (Top) Example of one of the two angiographic images needed to perform a biplane angiography of the LCA [94]. (Bottom) The exported left coronary angiographic data containing differently oriented circular sections lined up along centerlines. The Left Main Coronary Artery (LMCA) bifurcates into the Left Anterior Descending Artery (LAD) and the Left Circumflex Artery (LCX), which then further bifurcate downstream. A double-bifurcating vessel (DBV), a bifurcation (BIF) and a single bifurcating vessel (SBV) are indicated by arrows.

2.2.2 Topological partitions

The branches of the left coronary tree were manually partitioned in three different groups on the base of topological considerations: bifurcations (BIF), vessels connecting two bifurcations (double-bifurcating vessel, DBV) and vessels connecting a bifurcation to an inlet/outlet (single-bifurcating vessel, SBV), as shown in Fig. 2.1. In the BIF, intersecting sections were visually detected and removed as they did not correspond to real vessel luminal surfaces: of the two branches having intersecting sections, the branch with the larger diameter (main branch) was retained while the intersecting sections of the smaller branch (side branch) were removed. This operation was done by the operator but can be automated. No sections intersecting each other were found in DBV and SBV (see Fig. 2.2).
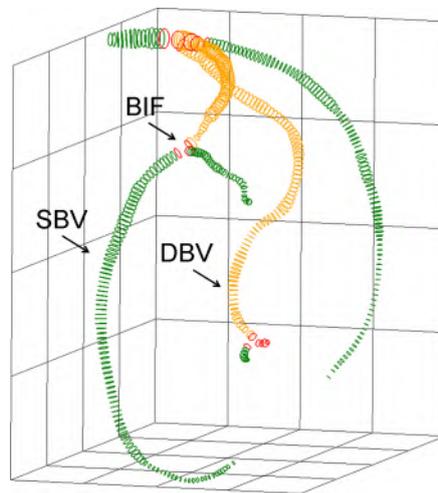
Figure 2.2: The LCA tree was divided in three different partitions by high-level operator interaction on the base of topological considerations: bifurcations (BIF, in red), vessels connecting two bifurcations (DBV, in yellow) and vessels connecting a bifurcation to an inlet/outlet (SBV, in green). In a bifurcation, the sections of the side branch intersecting a main branch were removed. This Figure offers a different view of the same LCA with respect to Fig. 2.1.

2.2.3 Geometrical surface reconstruction

2.2.3.1 Bézier spline implementation

The boundary surface described by circular sections in the VRML file was converted into a spline model by means of Bézier splines. The analytical implementation of the spline is described below.

A Bézier spline is a sequence of spline segments where each segment (a cubic curve) is defined by four control points by the following vectorial cubic function of the scalar variable $t \in [0, 1]$:

$$\mathbf{P}(t) = (1-t)^3\mathbf{P_i} + 3(1-t)^2 t\mathbf{P_i''} + 3(1-t)t^2\mathbf{P_{i+1}'} + t^3\mathbf{P_{i+1}} \qquad (2.1)$$

The points $\mathbf{P_i}$ and $\mathbf{P_{i+1}}$ are part of the initial set of input points and define the starting and the ending points of the spline segment. The two remaining points, $\mathbf{P_i''}$ and $\mathbf{P_{i+1}'}$ are not given as input and are calculated on the base of the initial set of points ($\mathbf{P_{i-1}}$, $\mathbf{P_i}$, $\mathbf{P_{i+1}}$ and $\mathbf{P_{i+2}}$) to define the slope of the curve at the end points. For example, $\mathbf{P_i''}$ lays on a straight line through $\mathbf{P_i}$, the direction of which is determined by the average of two unit vectors ($\mathbf{n_1}$ and $\mathbf{n_2}$) in the direction of $\overrightarrow{\mathbf{P_{i-1}P_i}}$ and $\overrightarrow{\mathbf{P_iP_{i+1}}}$. The distance between $\mathbf{P_i}$ and $\mathbf{P_i''}$ is equal to:

$$\left\|\mathbf{P_i} - \mathbf{P_i''}\right\| = 0.5 \left\|\mathbf{n_1} + \mathbf{n_2}\right\| \left\|\mathbf{P_i} - \mathbf{P_{i+1}''}\right\| cu \qquad (2.2)$$

where the cu is the curliness, a parameter that defines the curvature of the spline segment. The position of point $\mathbf{P_{i+1}'}$ is determined in a similar manner. This definition allows obtaining G_1 continuity (i.e. continuity of the tangent vector) in the connection point between two subsequent spline segments as illustrated in Fig. 2.3 [95].
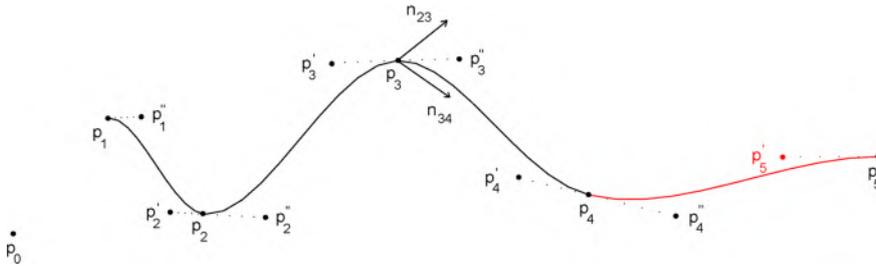
Figure 2.3: Illustration of the spline generation starting from six input points (from $\mathbf{P_0}$ to $\mathbf{P_5}$). All other points ($\mathbf{P'}$ and $\mathbf{P''}$) are derived from these initial six points. For example, in point $\mathbf{P_3}$, two unit vectors $\mathbf{n_{23}}$ and $\mathbf{n_{34}}$ are calculated based on the directions of the two line segments $\mathbf{P_2P_3}$ and $\mathbf{P_3P_4}$. Points $\mathbf{P_3'}$ and $\mathbf{P_3''}$ lay on the bisectrix of these two vectors. The spline can be extended by specifying the tangent in the extreme points as shown in point $\mathbf{P_5}$.

The surfaces of each vessel partition were reconstructed and parameterized using two sets of Bézier splines orthogonal to each other: closed splines for a transversal vessel section and open splines for the longitudinal vessel evolution.

The generation of artificial bumpiness or excessive tightness needs to be avoided in the vessel surface reconstruction from a set of points. The Catmull-Rom spline, which is a Cardinal spline with zero tension, incorporates the adjacent points without introducing an arbitrary curvature and is therefore adequate for reconstruction. [96] The tension $\mathtt{te}$ in a Cardinal spline is a parameter of curvature and makes the spline looser ($\mathtt{te} < 0$) or tighter ($\mathtt{te} > 0$). The curliness of the Bézier spline is equivalent to the tension of the Cardinal spline, given the relation:

$$\mathtt{cu} = \frac{(1 - \mathtt{te})}{3} \tag{2.3}$$
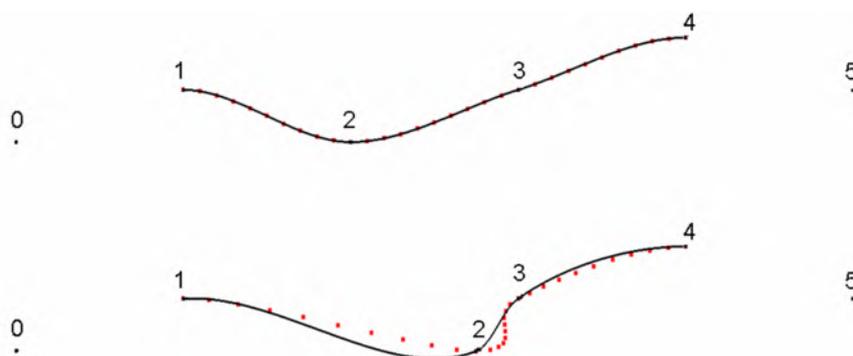
Figure 2.4: The relation between the curliness of a Bézier spline and the tension of a Catmull-Rom spline is shown graphically. The points 0-5 are the original points used to create a Catmull-Rom spline (dots) and a Bézier spline with $\mathtt{cu} = 1/3$ (solid line). (Top) If the points are equally distant from each other, Bézier and Catmull-Rom splines result identical, because the average of the normalized neighboring directions is equal to the vector between the neighboring points. (Bottom) With respect to its initial position, point 2 has been moved closer to point 3, thus altering the distance of point 2 from its neighboring points, point 1 and point 3. Consequently, the normalization included in the Bézier spline changes the direction of the curve at point 2 with respect to the Catmull-Rom spline. The Bézier spline seems giving a 'smoother' curvature (without forming 's'-shaped segments) as compared to the Catmull-Rom spline in case of non-equally distant points.

To reproduce the Catmull-Rom spline with a Bézier spline, the curliness was

set to 1/3. The Bézier spline implementation was preferred to the Catmull-Rom spline because of a more convenient definition of the tangents vectors: at the end points of a Catmull-Rom spline segment, the tangent vectors are parallel to the chords formed with the neighboring control points whereas, at the end points of a Bézier spline-segment, the tangent vectors are parallel to the average directions (average after vector length normalization) of the neighboring control points. Thus, the implemented Bézier spline differs from the Catmull-Rom spline because of a direction normalization and provides a more realistic profile in case of non-equally distant points, as shown in Fig. 2.4. Nevertheless, in the considered biplane coronary angiography, the distance of the points was approximately constant and both splines could have been used.

2.2.3.2 Bifurcations

All the bifurcations were reconstructed before the other partitions. The three non-intersecting cross-sections closest to the bifurcation were selected for each branch and separated from the rest of the branches (which could evolve forming new bifurcations, DBV, or end into an inlet or an outlet, SBV). Using the centerlines to define the directions of the three branches, the axis of the bifurcation was determined as the bisectrix of the trihedral angle formed by these directions. A bifurcation plane normal to this axis and passing through the intersection point of the three centerlines was defined. The projections of the cross-sections of the three branches on the bifurcation plane were used to create smooth lateral connections between the branches using planar open Bézier splines. For each spline the point closest to the bifurcation center was used to define the corresponding bifurcation side. This method is illustrated in Fig. 2.5, together with the resulting bifurcation sides. For each bifurcation, three branches composed of four sections (the original three and one defined by the two corresponding bifurcation sides) were separately reconstructed and parameterized. For each of the three original sections, a closed Bézier spline was used to define 16 equally-spaced points which were then stored as control points for the mesh generation (see section 2.2.4). This operation was repeated for all the sections of the three branches and the resulting points were used to define 16 longitudinal open Bézier splines for each branch. A different parameterization can be easily obtained by choosing a higher (lower) number of control points when higher (lower) geometrical accuracy is needed. At the connections between splines of different branches, G_1 continuity was obtained by forcing the tangent vectors of the splines' boundaries to be locally perpendicular to the bifurcation side. Finally, also the three original centerlines of a BIF were parameterized with open Bézier splines.
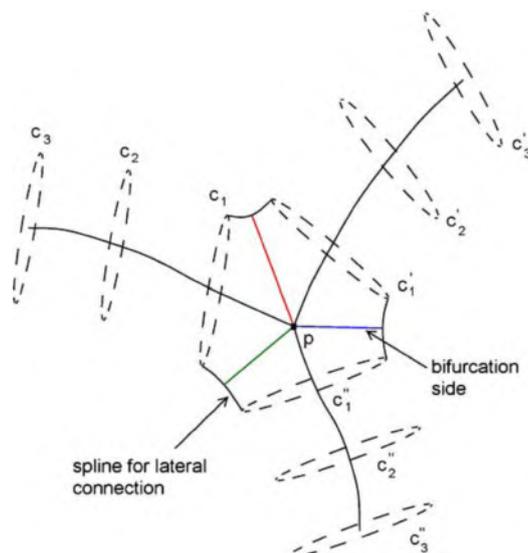
Figure 2.5: The three branches are projected on the bifurcation plane (defined by the bisectrix of the trihedral angle identified by the directions of the centerlines in the proximity of the bifurcation center) and smooth lateral connections between them are created using Bézier splines, in order to decompose the bifurcation into its three branches.

2.2.3.3 Double bifurcating vessels and single bifurcating vessels

The vessel portions between two bifurcations (DBV) or between one bifurcation and an inlet/outlet (SBV) contained a stack of circular sections which identified a tubular domain. For each section a closed Bézier spline was used to define 16 equally-spaced points (as described in section 2.2.3.2). Sixteen open Bézier splines were then used to parameterize the DBV/SBV longitudinally and one extra spline was used for the centerline.

2.2.3.4 Continuity at the connection between partitions

For a particular branch of the BIF, longitudinal splines have been created starting from the two corresponding bifurcation sides and ending at the section c_2 of Fig. 2.5. The tangent of the splines in this final section is determined by the two cross-sections c_1 and c_3 of Fig. 2.5, following the spline implementation described in section 2.2.3.1. The longitudinal splines of the attached SBV or DBV parts also end in section c_2 and the tangent is again determined by the sections c_1 and c_3. As a result, G_1 continuity is ensured between the different partitions [95]. The set of longitudinal splines for a portion of the LAD can be visualized in Fig. 2.6 with different colors

for different partitions.
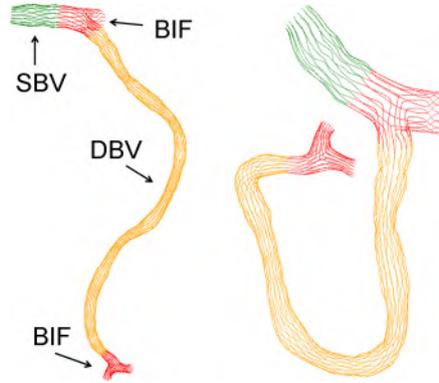
Figure 2.6: The three partition groups, BIF (in red), DBV (in yellow) and SBV in green), are converted from circular sections into longitudinal Bézier splines. At the transition between two partitions, G_1 continuity is ensured. Only a portion of the LAD is visualized for clarity from two directions.

2.2.4 Mesh mapping

After the spline parameterization, all the reconstructed vessel partitions appeared as tube-like structures (BIF, SBV and DBV) with a surface described and parameterized by sets of 16 longitudinal splines around a centerline spline. Thus, the same meshing strategy could be applied for all the partitions. An iso-parametric transformation was used to map an original mesh into the correct volume, by repositioning the original mesh nodes but without altering the original topological connections. The transformation, implemented in pyFormex, acted on an original meshed volume by means of 36 control points, transforming originally straight lines into parabolic or cubic curves, depending on the number of control points used (lines controlled by 3 or 4 points were transformed into parabolic or cubic curves, respectively, as shown in Fig. 3.10). Parabolic curves were used to fit the vessel partition circumferentially whereas cubic curves were chosen to have a higher control in longitudinal direction.

Two different meshed blocks (i.e. cuboids), one for the inner (IN_Block) and one for the outer (BL_Block) part of the lumen have been defined. A boundary layer of thin elements attached to the vessel wall is recommended when constructing the mesh in order to increase the solution accuracy near the wall, where higher velocity gradients are expected [61]. Both the IN_Block and the BL_Block have been constructed by extruding a pattern of quadrilaterals (Fig. 3.10). Each slice of tube was filled with four IN_Blocks and

eight BL_Blocks circumferentially. Hence, the resulting mesh topology was not axial-symmetric, but repeated after 90 degrees. Both the IN_Block and BL_Block meshes could be chosen finer or coarser in order to get a finer or coarser structured mesh. To account for the different longitudinal lengths of the vessel partitions, multiple mesh blocks were inserted longitudinally and their number was taken equal to the ratio between the curvilinear length of the centerline and the longitudinal resolution of the angiographic data (slice thickness 1 mm), in order to avoid a loss of information from the VRML angiogram. The vessel partitions were meshed separately and then merged into a single hexahedral mesh with G_1 continuity preserved all over the surface. It is noteworthy that the final structured mesh was topologically equivalent to the mesh chosen for the original meshed blocks and that the resolution could be varied parametrically by varying the number of elements in the meshed blocks. Additionally, if the original meshed blocks would be meshed with different element types (such as tetrahedrons and prisms), the same elements and the same element connectivity would appear in the mesh of the LCA. The mesh generation process in a bifurcation, from the circular sections to the hexahedral blocks is summarized in Fig. 2.8.
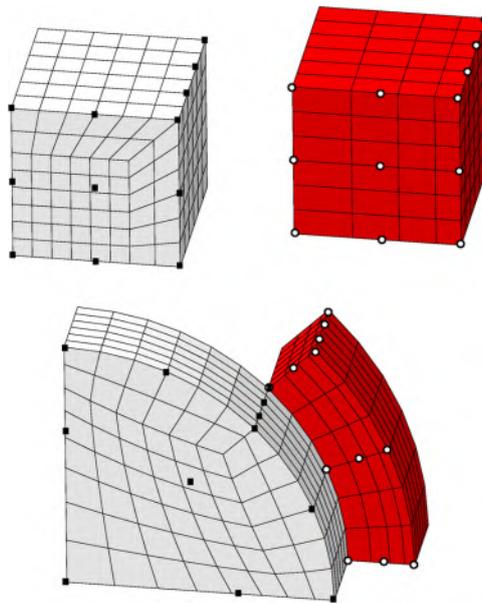
Figure 2.7: A set of 36 control points has been used to map a parametrically-defined mesh block (top) into a target volume (bottom). Two different blocks have been chosen for the lumen: IN_Block (white) for the inner part of the lumen, and BL_Block (red) for the portion of the lumen closer to the wall (boundary layer). Only the nine control points on one face and the four control points along the longitudinal edge are shown.
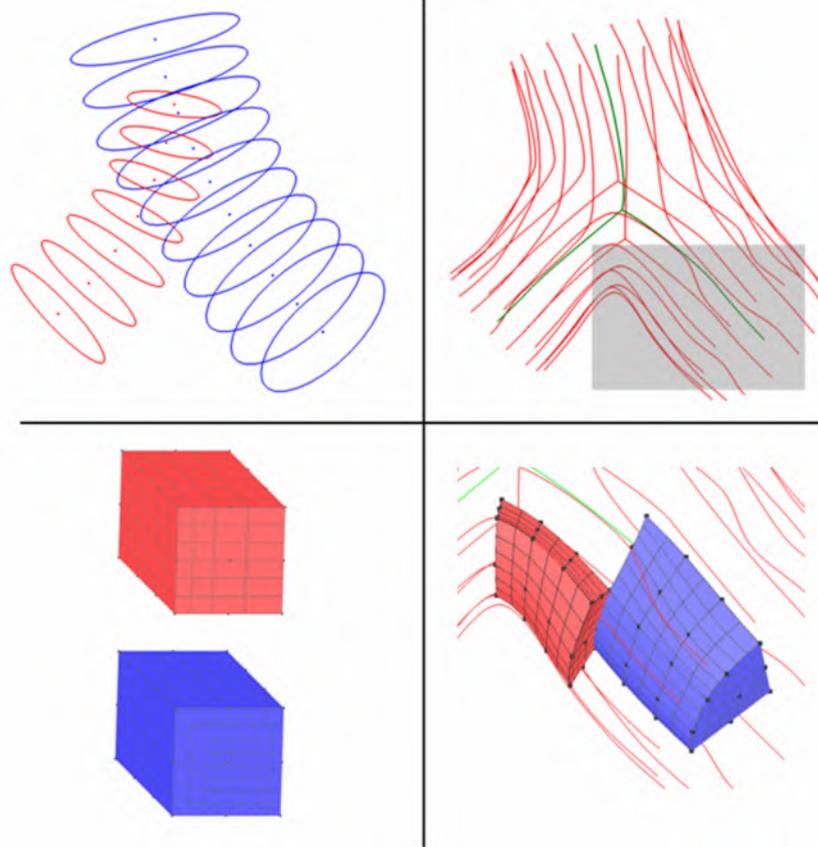
Figure 2.8: Mesh generation in a bifurcation: (from top-left to bottom-right) circular sections of a bifurcation with a main branch (blue) and a side branch (red); Bézier splines reconstruction of surface (red) and centerlines (green); the IN_Block (blue) and the BL_Block (red) before and after the spline-guided mapping.

2.2.5   Mesh sensitivity analysis

Seven structured hexahedral meshes (HEX series) were generated with the novel approach and seven tetrahedral-prismatic meshes (TP series) were generated for comparison, following a well established procedure [39, 80, 97, 98]. First, a very fine surface of 680,000 triangles was created from the coronary spline reconstruction in pyFormex and remeshed using Gambit [74] to improve the triangles' quality. Then, a volume mesh made of prismatic layers in the proximity of the wall and tetrahedrons in the inner volume was generated in TGrid [74]. Details on the mesh series are reported in Table 2.1. The parameter equiangle skew (Q_{eas}), described in Chapter 1, was taken as a measure of mesh quality.

Table 2.1: Seven meshes for the HEX series and seven meshes for the TP series have been generated for the grid convergence analysis. The number of prismatic layers in the TP series was arbitrarily chosen. For a chosen number of nodes, the number of required cells was approximately three times higher in a TP mesh with respect to a HEX mesh.

HEX cells	HEX nodes	TP cells (prismatic layers)	TP nodes
46,176	50,790	195,855 (5)	84,290
158,460	168,172	591,717 (7)	251,840
365,376	384,075	754,272 (10)	338,902
445,824	473,009	1,087,537 (3)	387,549
588,240	621,901	1,720,779 (7)	709,965
1,245,440	1,294,023	2,096,115 (5)	801,698
3,250,400	3,352,503	3,117,091 (3)	1,169,048

All the meshes of the HEX and the TP series have been used for CFD analysis under identical conditions using a general purpose commercial code (Fluent [74]). Blood was modeled as a Newtonian fluid (density 1060 kg/m^3 and viscosity 3.5 $mPa \cdot s$), the coronary wall was considered rigid and a zero-velocity was applied at the lumen boundary in order to satisfy the no-slip condition. Steady state 3D flow simulations were performed with parallel calculation on a in-house built low-cost, high performance computing cluster [99]. A plug-shaped velocity profile was applied at the inlet because coronary arteries originate from a large compartment (sinus Valsalvae) which prevents the development of a parabolic velocity profile [76, 82]. The inlet flow was taken from literature by averaging one cardiac cycle from Nichols & O'Rourke [100] and converted into an inlet velocity of 0.1824 m/s. The solver was set with second order upwind for the discretization of the momentum equation and double precision in order to minimize the round-off errors.

Prakash and Ethier have shown that WSS in coronary arteries is a critical quantity with respect to grid convergence [91]. Therefore, the WSS magnitude was chosen as term of comparison of the grids and analyzed using the area-averaged WSS, the 99 area-weighted percentile of the WSS and the local WSS. The area-averaged WSS was computed using the magnitude of the face-centered WSS vector ($\mathbf{WSS_{fc}}$) according to the following equation:

$$\text{Area-weighted WSS} = \frac{\int_A \|\mathbf{WSS}_{fc}\| \, dA}{A} \qquad (2.4)$$

The 99 area-weighted percentile (WSS_{99}) was calculated using the following relation: 99% of the lumen boundary surface had a $\|\mathbf{WSS}_{fc}\| < WSS_{99}$.

In order to evaluate the local WSS, a line, located between a stenosis and a bifurcation (a critical region with respect to the flow), was traced on the surface by intersecting the surface with a rectangle. The intersection entities were points on edges which, in general, did not correspond with the mesh nodes. Therefore, the post-processing interface provided together with the solver was queried to interpolate the WSS on the intersection points.

By means of this analysis, five parameters were quantified: (1) the mean WSS (area-weighted WSS on the entire lumen surface), (2) the WSS_{99} on the entire surface, (3-4) the area-weighted WSS on sub-domains of the first and the second bifurcation and (5) the WSS along a line located on the downstream side of a stenosis crossing the third bifurcation (Fig. 2.9).
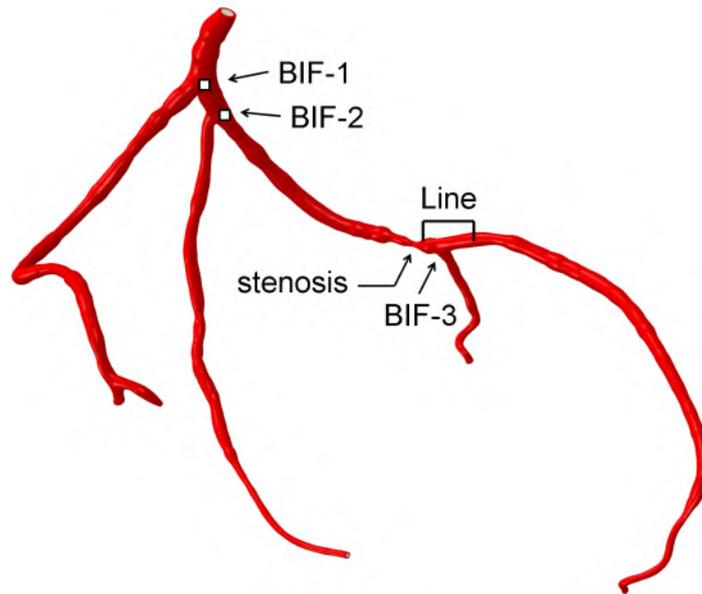
Figure 2.9: The surfaces on the first and second bifurcation (0.35 and 0.31 mm^2, respectively) used to compute the local area-weighted WSS magnitude, and the line (6 mm) used to compute the local WSS magnitude.

2.3 Results

2.3.1 Mesh quality
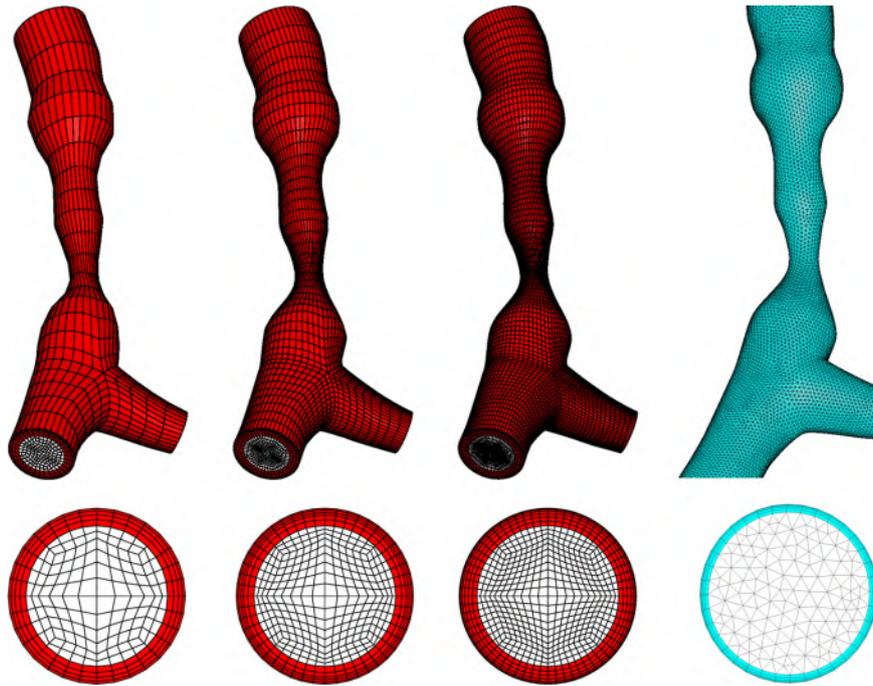
Figure 2.10: The first three panels show a detail of the different hexahedral meshes obtained changing the parameters assigned to the mesh blocks described in Fig. 3.10, resulting in increasingly finer meshes. The lumen sections show the square-based pattern (butterfly) used at each quadrant of the inner part of the lumen (white) and the layered pattern used for the boundary layer (red). The last panel shows a detail of a tetrahedral/prismatic grid and one lumen section with tetrahedral cells inside the lumen (white) and layered prismatic cells in the wall (blue).

The geometrical data provided as output after a biplane-angiography examination were used to reconstruct the left coronary tree by means of Bézier splines. These splines reproduced the surfaces of the vessels in which the coronary tree was partitioned with G_1 continuity (Fig. 2.6 and Fig. 2.8 right) and were used to parameterize the surface of each vessel into circumferential and longitudinal coordinates in order to fill the lumen volume with a structured hexahedral mesh. By using two different mesh-blocks, differently-sized elements were placed in the inner and in the outer part of the lumen. In the latter, thinner elements were expected to describe the

flow field with higher accuracy, improving the estimation of the WSS (Fig. 2.10). The cross-sectional nodal distribution was maintained throughout the volume, so that in the presence of a stenosis the number of elements in a cross-section does not decrease, and the mesh is scaled to a narrower section, allowing capturing the high velocity and high shear flows developing in this region [61].

A number of meshes were generated inside the same coronary domain, seven in the HEX series and seven in the TP series (Fig. 2.10). The quality of the mesh, expressed in terms of Qeas was found to be optimal for CFD applications for both mesh series (Table 2.2).

Table 2.2: The HEX and the TP series showed well shaped elements according to the equiangle skew, which was found always lower than 0.81.

Qeas	HEX 1,245,440 cells	TP 1,087,537 cells
0.0-0.25 (excellent)	656,524 (52.72%)	368,278 (33.86%)
0.25-0.50 (good)	585,416 (47.00%)	605,218 (55.65%)
0.50-0.75 (medium)	3,500 (0.28%)	113,930 (10.48%)
0.75-1.00 (poor)	0 (0.00%)	111 (0.01%)
max	0.61	0.81

2.3.2 Mesh performance in a CFD analysis

During the analyses, the residuals of continuity and velocity equations were checked and the simulations were prolonged until plateau values for the residuals were reached ($10^{-15} - 10^{-13}$ for the HEX series and $10^{-15} - 10^{-17}$ for the TP series). Our CFD simulations predict a WSS magnitude in a physiological range and a WSS distribution in line with the patterns reported in previous investigations [76, 80, 81, 101, 102]. Qualitatively, the WSS tends to increase going downstream because of narrowing of the arterial segments and also because a number of minor branches were not present into the original angiographic data [80, 101]. High WSS appears at the location of the stenosis just before the third bifurcation (Fig. 2.11).

The mean WSS computed with the HEX series increases from 2.21 to 2.26 Pa, from the coarsest to the finest mesh, respectively; conversely, the mean WSS computed with the TP series oscillates between 2.17 and 2.36 Pa, without exhibiting a clear converging trend (Fig. 2.12). The WSS_{99} ranges from 11.89 to 13.52 Pa in the considered grids and the finest HEX and TP meshes only differ by 1.9%. The HEX series shows a converging trend as mesh density increases whereas the TP series does not exhibit

a clear converging trend (Fig. 2.13).

The area-weighted-WSS in the BIF-1 and BIF-2 displays convergence for both the series. The coarsest HEX (TP) mesh underestimates the area-weighted WSS with an error of 12% (25%) and 16% (67%) relative to the finest HEX (TP) mesh for the BIF-1 and BIF-2, respectively (Fig. 2.14).

Local values of WSS along a line going from the downstream side of a stenosis to the third bifurcation converge to a qualitatively similar profile in both the TP and HEX series but the finest HEX grid shows a 14% higher peak value with respect to the finest TP. Considering the peak values, the coarsest HEX (TP) mesh provides an error of 24% (166%) relative to the finest HEX (TP) mesh. The WSS plot obtained with the finest meshes shows first a smaller oscillation and then a bigger one. All the grids of the HEX series respect the final profile and gradually approach it quantitatively as the mesh density increases whereas the three coarsest grids of the TP series show a different trend with a bigger oscillation first followed by a smaller one (Fig. 2.15).

From the considered meshes, the minimum number of cells needed to reach grid-independent WSS-based parameters with an error lower than 5% relative to the finest HEX and TP meshes, are $365, 376$ and $2, 096, 115$ for the HEX and the TP series, respectively. Using these resolutions, two CFD simulations have been repeated on the same node of the cluster (4 CPUs, 2.83 GHz, 8 GB of memory) in order to evaluate the CPU run time required to reach the same accuracy of the WSS for the HEX and the TP series. The HEX grid converged after 3 min while the TP grid after 43 min.
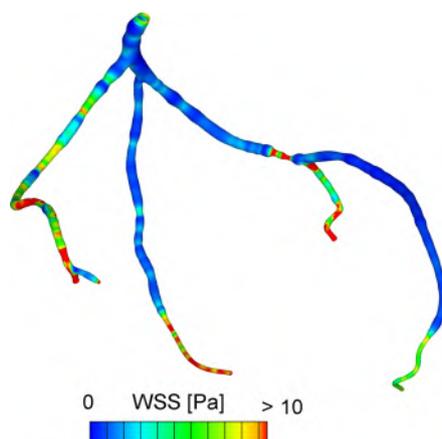
Figure 2.11: Visualization of the WSS of the reconstructed left coronary tree for the finest HEX mesh. Red color means > 10 Pa.
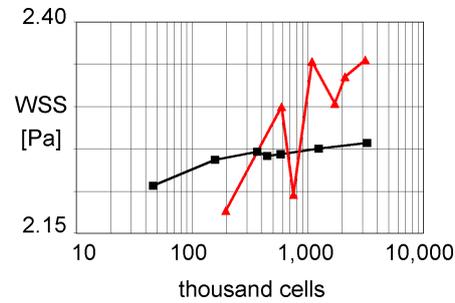
Figure 2.12: Area-weighted WSS (mean WSS) on the entire lumen surface. The black curve with squares represents the HEX series and the red curve with triangles represents the TP series.
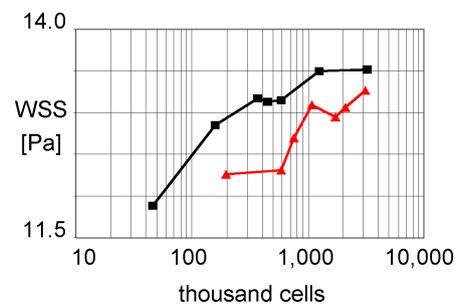
Figure 2.13: WSS_{99} (maximum WSS) on the entire lumen surface. The black curve with squares represents the HEX series and the red curve with triangles represents the TP series.
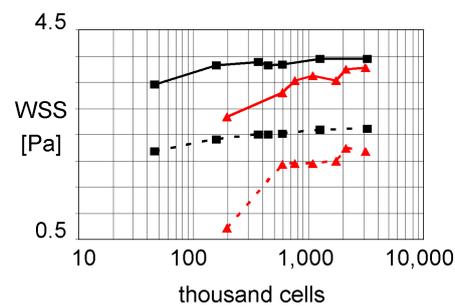
Figure 2.14: Area-weighted WSS on selected regions in the BIF-1 and BIF-2 (see Fig. 2.9). The black curves with squares represent the HEX series and the red curves with triangles represent the TP series. The solid and dotted line represent the first and the second bifurcation, respectively.
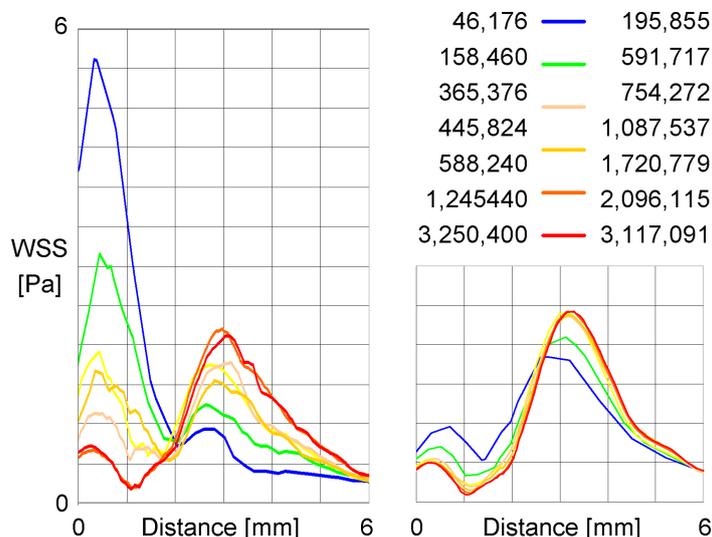
Figure 2.15: Local values of WSS along a line going from the downstream side of a stenosis to BIF-3. The surface line is indicated in Fig. 2.9. The left diagram displays the WSS computed with the 7 meshes of the TP series whereas the right diagram displays the WSS computed with the 7 meshes of the HEX series. Note the large change in the profile with different resolutions of the TP series and the small adjustement produced by high resolution meshes of the HEX series.

2.4 Discussion

In this study we present a new methodology to create a parametric structured hexahedral mesh from biplane coronary angiography. To the authors' knowledge, this represents the first attempt to generate a computational hexahedral mesh in the coronary tree. By taking advantage of the automatic segmentation provided by the angiographic technology, the coronary surface was reconstructed and parameterized by means of Bézier splines and then filled with a structured volume mesh using a 3D mapping transformation. The new strategy enables the generation of a high quality structured mesh for CFD analysis. The quality of the mesh is very high in terms of skewness, the cells are generally oriented with the predominant flow (approximated by centerlines) and are parallel to the boundary surface next to the wall. The generated mesh is equivalent to a sweeping-based mesh, as the cross-section of the vessel maintains the same topology in all branches: a butterfly pattern [103].

In order to assess the added value of the new meshing method with respect to commonly used and automatically-generated tetrahedral-prismatic

meshes, a comparative analysis was performed. Seven structured meshes and seven unstructured meshes with increasing resolution were generated and used for the computation of the WSS by means of CFD. The elements-to-nodes ratio in TP meshes was found to be around 3 while for tetrahedral-only meshes it was found to be around 6 (see Chapter 1). This difference can be explained with the presence in the TP meshes of a prismatic sub-mesh, which can be considered an intermediate mesh type between a structured and an unstructured mesh. The mean WSS and the 99 area-weighted percentile were calculated as global parameters over the entire surface, the area-weighted WSS in two bifurcations as regional parameters and the WSS along a line as a local parameter. The mean WSS computed using the HEX series shows a low mesh-dependence, suggesting that very coarse meshes are adequate to evaluate an average hemodynamic condition, while the mean WSS computed using the TP series shows a high mesh-dependence and oscillates without indicating a clear converging trend. The maximum value of WSS, approximated by the 99 area-weighted percentile, increases together with the number of cells and stabilizes to a similar value with both the mesh series. Nevertheless, a HEX mesh requires less cells to give a similar accuracy of the maximum WSS. The two area-weighted WSS magnitudes in the bifurcations show a converging trend for both the HEX and the TP series. Again, the values predicted by the coarse HEX meshes are closer to the asymptotic value as compared to coarse TP meshes. The HEX and the TP series significanlty differ in the prediction of the WSS along a line. The coarsest HEX series (46,176 cells) already starts with a WSS profile which is qualitatively similar to the finest mesh with a difference at peak value of 24%. The TP series starts with a WSS profile which is quantitatively and qualitatively wrong, with the peak value in a wrong position if the number of cells is lower than 1 million.

All the considered values (mean WSS, 99 area-weighted percentile, regional WSS and peak value along a line) in the two finest HEX meshes (1,245,440 - 3,250,440) differ only by 0.2% against a 3 times higher grid density. Conversely, the two finest TP meshes (2,096,115 - 3,117,0914) differ 4.1% against a 1.5 times higher grid density. Thus, both the HEX and the TP series reach mesh-independent WSS values with less than 5% error relative to the finest HEX and TP meshes but with a HEX mesh of 365,376 cells and a TP mesh of 2,096,115 cells. These two meshes have been used to evaluate the computational effort (CPU run time) required to reach the same accuracy of the results. The computational time is 14 times smaller for the HEX mesh (3 min and 43 min for the HEX and the TP mesh, respectively).

Our results clearly indicate that HEX meshes converge better than TP meshes and, for the same accuracy of the results, 6 times less cells and 14 times less CPU time are required. Longest and Vinchurkar report that a

HEX mesh needs 3.5 times less CPU time than a TP (tetrahedral-prismatic) mesh with comparable degrees of freedom [104]. In our case, we have found that a factor 14 relates the number of cells of HEX and TP meshes of similar accuracy of the WSS. This more pronounced difference may be the result of the combination of the faster calculation and the lower number of cells required for the accurate WSS estimation. Prakash and Ethier investigated the effect of the grid resolution using unstructured tetrahedral-only meshes in coronary arteries and found that non-adaptive meshes could achieve a mesh-independent velocity field but failed to provide a mesh-independent WSS [91]. This matches with our observation, even if we have used a combination of tetrahedral and prismatic elements in the unstructured meshes (TP). Other authors report a relative error in the WSS calculation in coronary arteries of 5% using tetrahedral/prismatic meshes [6, 82]. For the local WSS estimate using the two finer meshes of each series, our simulations predict an error of 4.1% using unstructured meshes and 0.2% using hexahedral structured meshes. Moreover, we have penalized the HEX meshes by choosing a difference of 3 times the number of elements between the two finest HEX meshes and 1.5 times the number of elements between the two finest TP meshes.

The CFD analysis of the coronary flow aimed at comparing different mesh types rather than depicting the realistic hemodynamic scenario. To model coronary flow, one would have to complicate the model by including a pulsatile flow and moving walls in response to both the fluid-structure interaction and the extravascular compression produced by the pulsating cardiac muscle (most of the coronary flow occurs during diastole).

Antiga and collaborators suggest that since the blood motion in arteries is highly directional, the use of computational meshes with well organized elements along the main flow direction contributes to provide more accurate numerical solutions compared to unstructured meshes [61]. A good computational mesh should accurately resolve both the complex geometry and the physiologically relevant flow features [91]. The geometry of arterial districts is tubular with a longitudinal dimension much larger than the radial dimension, requiring high grid resolution circumferentially and low grid resolution longitudinally, with the exception of bifurcations, stenosis, aneurysms and highly curved regions. In a tubular vessel, resembling a long straight axial-symmetric tube, the velocity gradient is much smaller in longitudinal and circumferential direction as compared to the radial direction. Therefore, a good mesh for long straight arterial segments should have good resolution both circumferentially (for the geometry) and radially (for the flow) but not longitudinally. In order to accomplish this feature, hexahedral meshes with cells aligned longitudinally can be stretched in the longitudinal direction without degrading the shape of the elements in terms of skewness. This is generally not the case for TP meshes because stretching

an unstructured mesh produces element distortion (change of the angles between the edges of the cells) which in turn introduces errors in the CFD analysis, as shown in Fig. 2.16.

Hexahedral structured meshes with cells aligned along the centerlines flow have gridlines (cell edges) aligned with the predominant flow while tetrahedral meshes generally cannot provide alignment of the edges with the flow. It is known that a good alignment between mesh edges and flow (like in structured hexahedral meshes) reduces the computational errors due to numerical diffusion. On the other hand, unstructured meshes with randomly oriented cells are reported to introduce relevant numerical diffusion in the flow solution, especially in mainly unidirectional flow systems [103, 104].
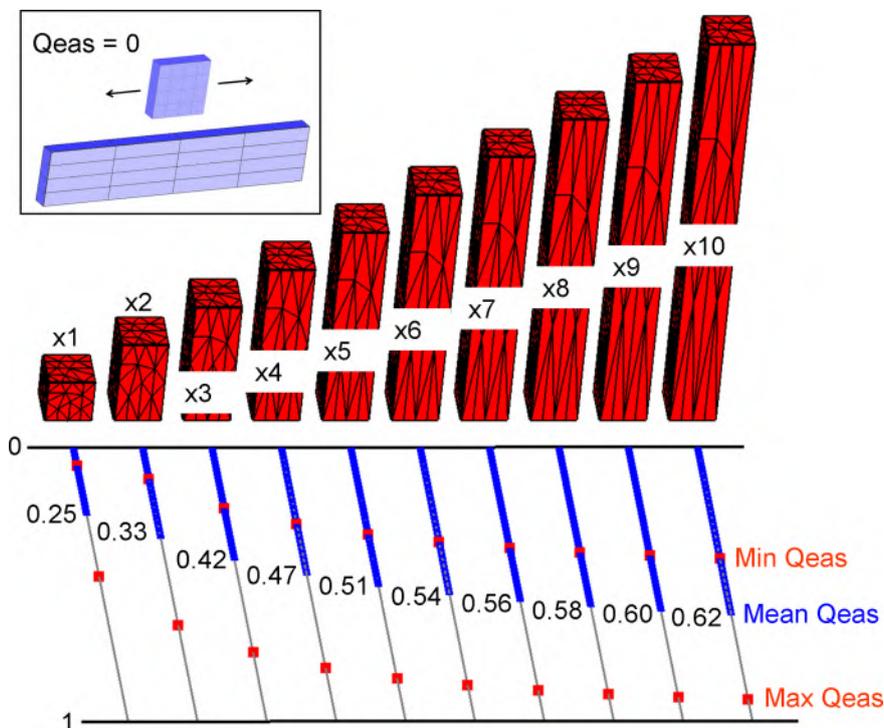
Figure 2.16: An unstructured and a structured block are stretched in one direction. (Outside the box) The mesh of the unstructured block degrades with stretching and its skewness becomes critical (Qeas > 0.4, according to [74]) already after tripling the block length. The minimum, mean and maximum Qeas of the unstructured mesh are plotted for 10 steps of stretching and show that mean and maximum Qeas are very sensitive to stretch. (In the box) A structured block keeps the original quality after stretching (if the stretch is performed along the direction of the edges) because the angle between two edges (90°) is not sensitive to stretch, enabling the use of geometrically-anisotropic meshes in CFD.

2.5   Conclusions

Hexahedral meshes are often thought to provide the highest quality solution but are generally more difficult to generate and the associated operator interaction time can be prohibitively expensive [39]. Our approach enables the hexahedral mesh generation in patient-specific vascular districts, resulting in well shaped elements suitable for CFD applications and superior in terms of accuracy and performance to mesh generated using automatic meshing strategies. However, some important limitations remain: (1) our angiogram consists of circular sections while, in general, a triangulated surface provides a more accurate geometrical representation; (2) vascular regions often include trifurcations and other complex structures, such as aneurysms, which cannot be meshed using the described approach; (3) the procedure of topological decomposition of the arterial tree requires a long operator intervention. To overcome these limitations, Chapters 3 and 4 present versions of the mesh generation framework dedicated to either automate or generalize the procedure.

Chapter 3

Bifmesh: hexahedral mesh generation in a nearly-planar vascular bifurcation

IN this chapter we deal with the generation of a structured and conformal hexahedral mesh from a triangulated surface model of a nearly-planar arterial bifurcation. In Chapter 2, we have demonstrated the advantages of using a structured mesh with respect to an unstructured mesh for the computation of the arterial WSS using image-based CFD, both in terms of result accuracy and computational run time. A meshing strategy applicable to arterial lumen models described by series of circular sections was developed and tested for biplane-angiography-based CFD analysis of coronary flow. When a vessel is accurately scanned using CT, MRI or US, the vessel model, obtained from the image segmentation, should be preserved during the mesh generation process. Converting the surface model into a series of circular sections would result in a significant degradation of the geometrical details. Therefore, we present an extension of the meshing tool, firstly applied to circular sections, to triangulated surface models and implement a robust, fast and automatic methodology (the Bifmesh) to generate a structured hexahedral mesh of the lumen and wall of a nearly-planar arterial bifurcation. The mesh of the lumen (CFD mesh) can be used to analyze the flow whereas the mesh of the wall (FEA mesh) can be used to analyze the structure. Together, the CFD and FEA meshes can be integrated for an FSI analysis, as shown in Chapter 5[1].

---

[1] The content of this chapter was published in the journal, Computer Methods in Biomechanics and Biomedical Engineering:
Patient-specific computational haemodynamics: generation of structured

3.1   Introduction

Starting from the original medical images, a number of steps need to be performed to assess the patient-specific hemodynamics. Software packages such as the Vascular Modelling Toolkit (VMTK) [47], 3D Slicer [105], OsiriX [106] and Mimics [48], offer advanced segmentation tools to reconstruct the lumen surface, usually as a triangulated surface model (STL file format), by segmenting a medical image (3D angiography, CT, MRI). The lumen volume delimited by this surface needs to be discretized into a computational mesh for the numerical integration of the Navier-Stokes equations. Volume discretization (i.e. mesh generation) is a critical step in image-based analysis because the accuracy of the computational solution (e.g. velocity or WSS) is affected by (i) the mesh resolution, (ii) the mesh-element type (tetrahedral, prismatic or hexahedral) and (iii) the mesh topology (structured or unstructured). Because of the geometrical complexity of the blood vessels, which include bifurcations and stenoses, most of the patient-specific CFD investigations have relied on automatically-generated unstructured tetrahedral meshes, often in combination with prismatic boundary layers. Unstructured-mesh generators allow the user to fill the lumen volume with a limited interaction, by means of the Delaunay tetrahedralization [107], respecting the surface model obtained with the segmentation. In Chapter 2, we have compared the performance of structured and unstructured meshes and we have found that tetrahedral-prismatic meshes required about 6 times more cells to reach a mesh independent WSS (with a tolerance of the WSS measures below 5%) and 14 times longer run time as compared to structured hexahedral meshes. Moreover, by further refinement, the mesh-dependent error did not decrease below 5% with unstructured meshes, as indicated by oscillations of the WSS estimates, whereas it decreased *progressively* with structured meshes [73].

In this chapter we describe a robust automatic tool, referred as the vascular BIFurcation MESHer or 'Bifmesh', to generate a conformal structured hexahedral mesh from an STL surface of a bifurcating vessel, by combining a spline reconstruction of the luminal surface with a cubic isoparametric mapping operation. The vessel bifurcation needs to be nearly-planar, meaning that there is at least one direction (usually the bifurcation axis) such that all possible lines oriented in that direction intersect the vessel in none or one single cross-section. In addition to the arterial lumen, a facility to generate the arterial wall is developed. The external surface of an arterial wall is often invisible in a medical image and needs to be reconstructed based on

---

the local lumen size. The Bifmesh allows reconstructing the external wall surface and then generating a mesh inside the arterial wall. The purpose of this implementation is to provide a comprehensive graphical environment (Graphical User Interface, GUI) in order to facilitate the generation of high-quality meshes by a non-expert user in a matter of minutes. In the next section, the implementation of the Bifmesh, as integrated in the pyFormex GUI, is described using a patient-specific carotid artery bifurcation as an example.

3.2   Materials and methods

A carotid artery of an 83 year old patient was scanned using CT angiography. The 3D image in DICOM file format was segmented using Mimics [48] in order to generate a triangulated manifold mesh representing the lumen surface. This surface, which included the vasculature situated between the aortic arch and the lower cerebral arteries, was first cropped to define the carotid artery (Fig. 3.1) and then deprived of the secondary branches (Fig. 3.2). The Bifmesh was applied to this surface model to generate a structured and conformal hexahedral mesh in the carotid bifurcation, using a dedicated GUI implemented in pyFormex [75].

The Bifmesh requires three steps to generate a volume mesh from the surface model obtained with the image segmentation:

1. the triangulated surface is converted into six series of semi-slices, applying a predefined topology to the patient-specific surface model;

2. using couples of semi-slices, a set of longitudinal splines is constructed around each branch of the bifurcation;

3. a 3D mesh is mapped in the bifurcation volume by seeding the splines with control points.

If the external surface of the wall is also segmented from the medical images, the same procedure described for the CFD mesh can be applied to the arterial wall. Otherwise, if this surface is not available, it can be artificially reconstructed by scaling the lumen sections (step 1) according to the wall thickness. By repeating the steps 2 and 3 on the wall, as already done for the lumen, a quadrilateral mesh of the internal and external wall surfaces is produced. These surfaces are then connected to generate a hexahedral mesh in the arterial wall. The workflow for the mesh generation is summarized in Fig. 3.3 [108].
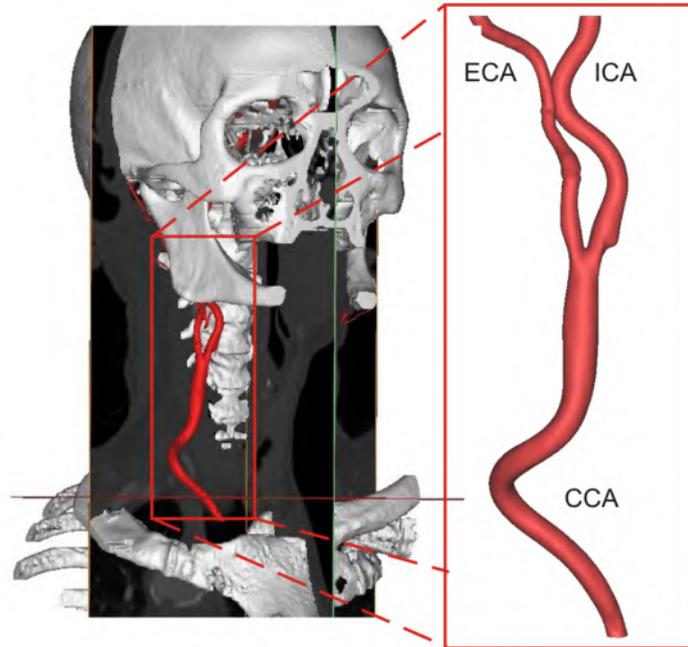
Figure 3.1: With the segmentation, boundary surfaces are extracted from the 3D image and cropped to the regions of interest (ROI). By filtering out the minor branches in the ROI, the carotid bifurcation is extracted (in the box) for the mesh generation. The three branches, common carotid artery (CCA), internal carotid artery (ICA) and external carotid artery (ECA) are indicated.
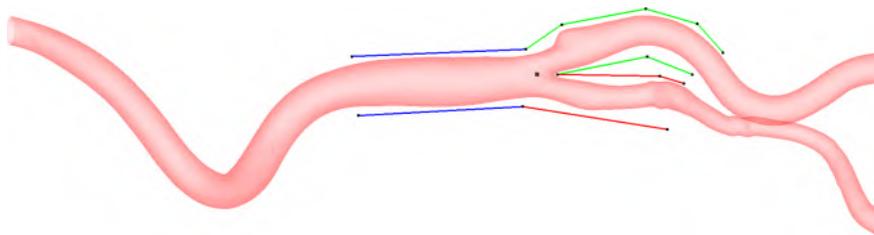
Figure 3.2: After orienting the carotid artery surface along the principal axes of inertia, the user selects a set of 2D points (by clicking on the monitor) to define six helper lines around the bifurcation and a bifurcation center.
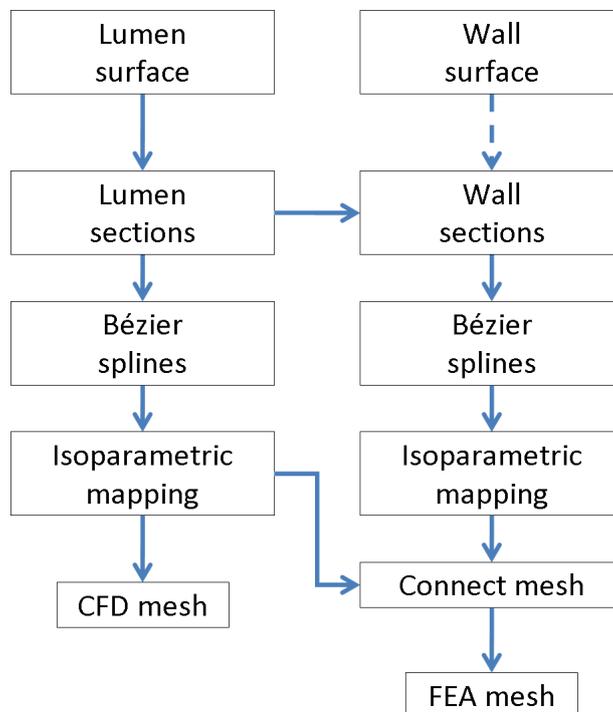
Figure 3.3: Procedure to generate a structured hexahedral mesh of the lumen and wall of an arterial bifurcation from a triangulated surface model. The wall sections can be reconstructed either by slicing the wall surface, if available (dotted line), or by scaling the lumen sections based on average anatomical data.

3.2.1 Lumen sections by slicing a triangulated surface mesh

When the bifurcation is oriented along the principal axes of inertia, with the bifurcation plane perpendicular to the z-axis, the user can select a set of 2D (x and y) points on the monitor along each side of the branches. These landmarks (at least 9), together with an extra point which identifies the bifurcation center, define the region of interest (ROI) and the bifurcation branching topology (Fig. 3.2), and are used to automatically orient and position three series of slicing planes. After cutting, the centers of a series of slices approximate the centerline of a branch, as shown in Fig. 3.4.
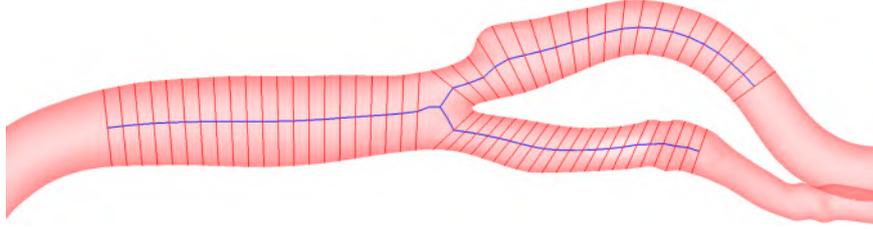
Figure 3.4: On each branch, helper lines guide the slicing planes, returning a series of slices, the center of which approximate the branch's centerline.

The three centerlines and the six helper lines previously defined by the user (Fig. 3.2) guide three sets of biplanar knives to slice the bifurcation. With respect to the first slicing operation (Fig. 3.4), this second slicing acts also on the central portion of the bifurcation. The slicing operation returns six series of cross-sectional polylines (semi-slices), two per branch, with three semi-slices at the bifurcation center interconnecting the branches (Fig. 3.5). A higher number of knives would return a more accurate longitudinal representation of the surface.
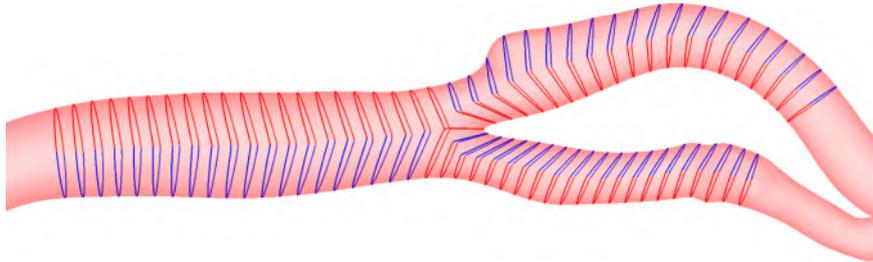
Figure 3.5: The six helper lines and the three centerlines define three sets of biplanar knives which slice the entire bifurcation, including the central region. The three branches are modelled with six series of semi-slices and interconnected by three semi-slices.

3.2.2   Bezier splines to reconstruct and parameterize the surface

From a series of semi-slices 13 longitudinal Bezier Splines are generated on a semi-branch [60], using the implementation described in Chapter 2. Splines of contiguous semi-branches are interconnected by keeping G_1 continuity (the splines describe continuous paths with a continuous tangent between two flow boundaries, i.e. inlet to outlet or outlet to outlet), except for three splines at the top and at the bottom of the bifurcation, which intersect the bifurcation axis. As a result, a branch is modelled by 24 splines around one

centerline, and can be partitioned in quarters (7 splines on the boundary and one centerline define a quarter as shown in Fig. 3.6).
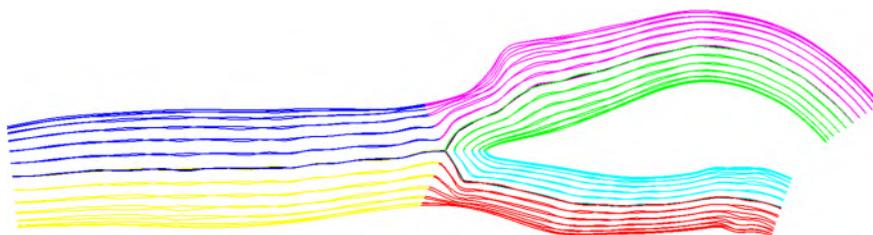
Figure 3.6: The longitudinal splines (inlet to outlet and outlet to outlet) span the surface with G_1 continuity except at the top and at the bottom centers, which join three splines.

The boundary of a branch may be far from a circular section, requiring a flow extension to facilitate the application of the boundary conditions. If needed, few extra sections, with the same area of the last slice of the ROI (Fig. 3.5), can be added outside a branch in the direction of the centerline, prolonging the surface with cylindrical extensions, as shown in Fig. 3.7 [39]. In the rest of the chapter, flow extensions are not taken into account, to facilitate a geometrical comparison between the final mesh and the original surface.
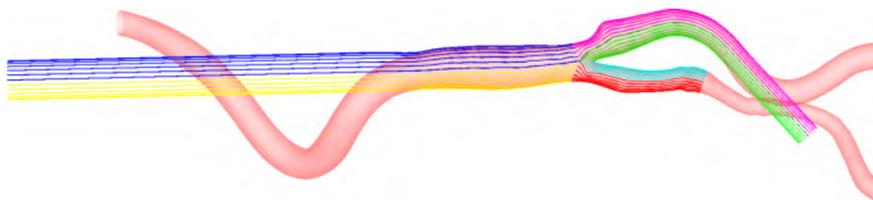
Figure 3.7: By adding slices in the direction of the centerlines, the branches are prolonged with cylindrical flow extensions. In the example, only the CCA and the ICA are equipped with flow extensions because an extension of the ECA would intersect the extension of the ICA.

3.2.3 Isoparametric mapping

The longitudinal splines describing the bifurcation are sampled with control points of an isoparametric transformation for the mesh mapping. First, the centerline splines are seeded with a number of points, setting the longitudinal resolution of the final mesh. A different number of points can be chosen

for each branch (na, nb, nc) and a shorter distance between two seeds can be set in the proximity of the bifurcation to increase the longitudinal mesh resolution (Fig. 3.8). Then, through each centerline's seed, a curved knife is used to cut the splines, generating a number of curved slices. With respect to a cutting plane, the use of a curved knife allows accommodating the connection between two semi-slices, improving the visual appearance and quality of the final mesh (Fig. 3.9).
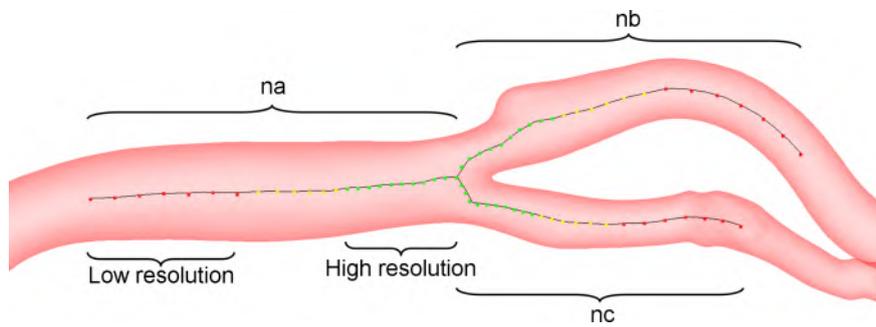
Figure 3.8: The three centerlines are seeded with points to set the longitudinal mesh resolution: na, nb and nc on the CCA, ICA and ECA, respectively. Differently spaced points can be set on a centerline in order to design a finer mesh in the region of the bifurcation (green points) and a coarser mesh in the straight portion of a branch (red points), with a transition between the two.
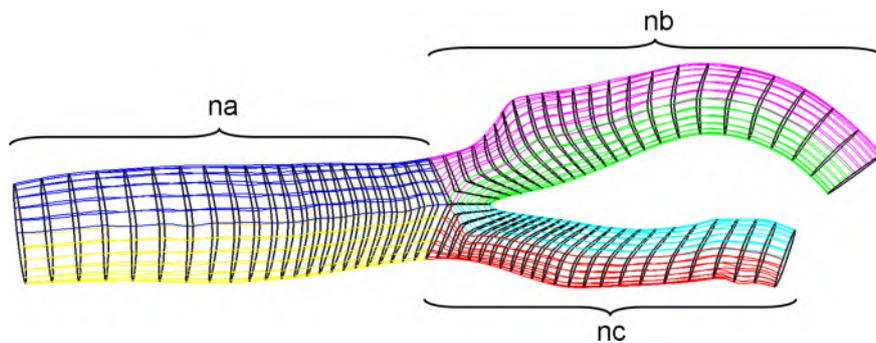
Figure 3.9: The slices, obtained by cutting the bifurcation with curved knives, provide smoother circumferential gridlines as compared to the cutting semi-planes displayed in Fig. 3.5.

The points on the splines obtained after cutting are sorted longitudinally and grouped in sections. In each quarter of a section, 7 points on the lumen

and a point on the centerline are interpolated to create 5 sets of 16 control points: one set of points is located in the inner side the quarter, two sets are located in an intermediate position and two other sets on the outer side of the lumen (boundary layers). These sets of points are used to control an isoparametric transformation which maps a planar quadrilateral surface onto a cubic surface according to the coordinates of 16 control points. Three different planar quadrilateral surfaces (2D Cartesian grids) are mapped on the 5 sets of points, in order to allow differentiating the cross-sectional mesh resolution along the radial direction: three integers, a, b and c, are used to parameterize a quarter of the vessel cross-section, which contains $a(a + 2b + 2c)$ quadrilateral faces (Fig. 3.10).
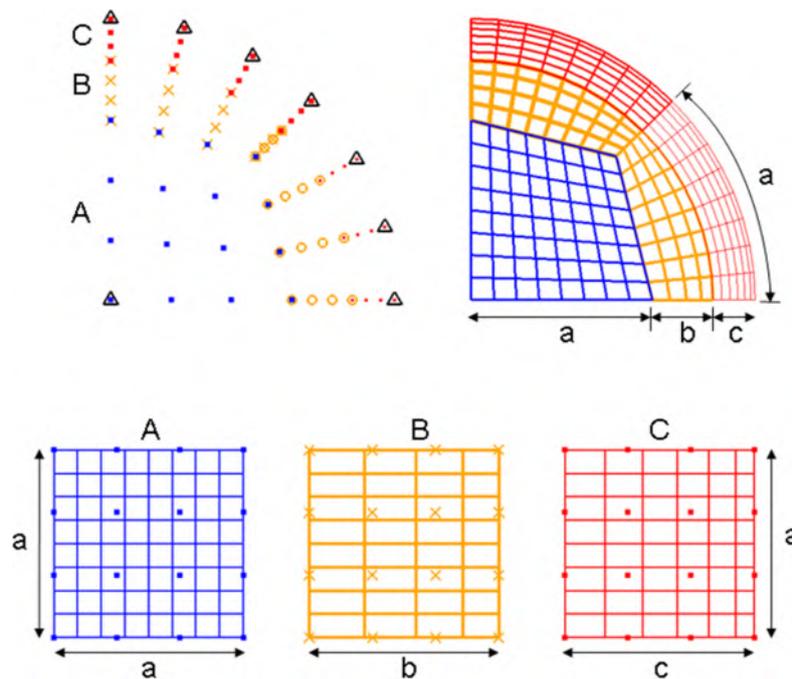
Figure 3.10: Seven points on the boundary and a single point on the centerline describe one quarter of a section. Based on these initial points (triangles), 5 sets of 16 points each are created (colored points). Three parametrically defined quadrilateral patterns (A, B, C) are mapped into the 5 regions by using an isoparametric transformation. Three parameters (a, b, c) describe the number of cells in the inner squared pattern (blue, a^2 cells), in the two transition regions (yellow, $2ab$ cells) and in the boundary layer (red, $2ac$ cells), setting the cross-sectional mesh density. The cells become gradually thinner moving towards the wall, in order to better resolve the near-wall flow for the calculation of the WSS.

As a result, a stack of 3D quadrilateral surface meshes populates a branch. By connecting these surfaces (sweeping), a structured hexahedral mesh is generated (Fig. 3.11).
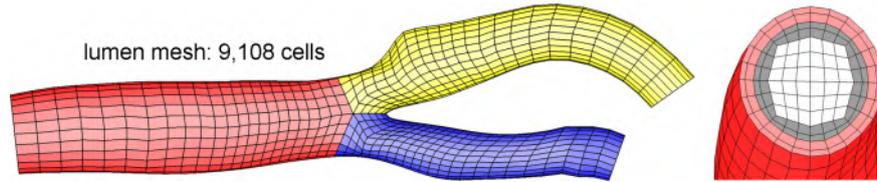
Figure 3.11: Using the control points, a structured quadrilateral mesh is mapped on each slice. By connecting the quadrilateral surfaces in order, a structured hexahedral mesh is generated. The parameters to obtain this coarse mesh are listed in Table 3.1.

Table 3.1: The mesh resolution is determined by the cross-sectional, longitudinal and radial parameters, according to Eq. 3.1 for the CFD domain and Eq. 3.2 for the FEA domain. The meshes with the different resolution are displayed in Figs. 3.11, 3.16, 3.17 and 3.18. The geometrical accuracy can be improved by increasing the number of slices but up to a treshold. The element quality is high for both CFD and FEA meshes.

Mesh	Low resolution	Medium resolution	High resolution
Number of slices	20	40	60
Cross-sectional parameters: a, b, c	3, 2, 2	6, 4, 5	13, 10, 10
Longitudinal parameters: na, nb, nc	23, 23, 23	71, 56, 45	151, 122, 93
Radial parameter: nr	1	3	4, 3, 2
			in three layers
Cells in CFD mesh	9,108	99,072	1,008,696
Cells in one layer	1,656	8,256	38,064
Cells in FEA mesh	1,656	24,768	342,576
Accuracy (μm)	5.33/164.6	2.65/54.9	2.62/64.0
			mean/max
Qeas	0.05/0.27/0.74	0.03/0.024/0.75	0.02/0.25/0.75
Scaled Jacobian	0.18/0.81/0.99	0.21/0.86/1.00	0.19/0.88/1.00
			min/mean/max

3.2.4 Wall surface generation

The mesh generation strategy for the lumen of a bifurcation can be extended to the vessel wall. If the external wall surface is available from medical images, the procedure described for the lumen surface can be repeated for the wall surface. Then, by connecting the internal and external quadrilateral surface meshes, a structured hexahedral mesh is generated in the wall. If the external wall surface is not available, it needs to be reconstructed using anatomical data. In general, the wall thickness of a healthy vessel depends on the local vessel size (local radius). A linear relation between the local radius (the local distance from centerline) and the wall thickness has been reported for coronary arteries and assumed in this study [109]. In the example case, the external wall surface was created by scaling with a factor 1.33 a subset of the lumen sections generated for the CFD mesh (Fig. 3.5). The sections corresponding to the stenotic region were not included, in order to model a thicker wall at the diseased location, as shown in Fig. 3.12 [52].
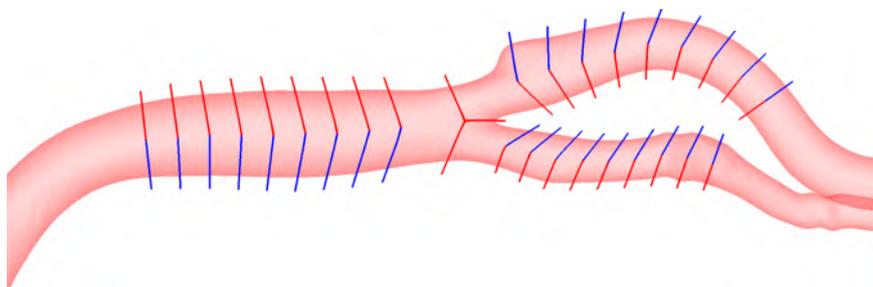
Figure 3.12: When the external vessel wall surface is not available, the sections of the inner surface can be scaled, reproducing a realistic wall thickness based on anatomical data.

Longitudinal Bezier splines can be constructed from the wall sections and, by using the same centerline seeds and the same cross-sectional parameters as for the lumen (Fig. 3.13), a volume mesh can be generated inside the outer surface of the wall (Fig. 3.14).
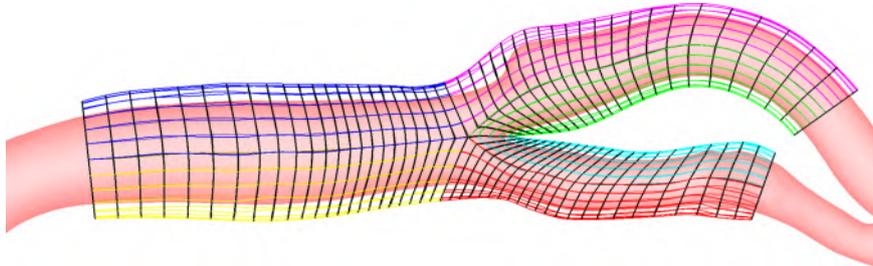
Figure 3.13: Spline reconstruction of the outer surface of the vessel wall. Note the thicker wall in the region of the stenosis and the smaller thickness in smaller vessels.

The boundary of this mesh and the boundary of the CFD mesh represent two topologically-equivalent quadrilateral meshes of the outer (wall) and inner (lumen) surfaces (Fig. 3.15).
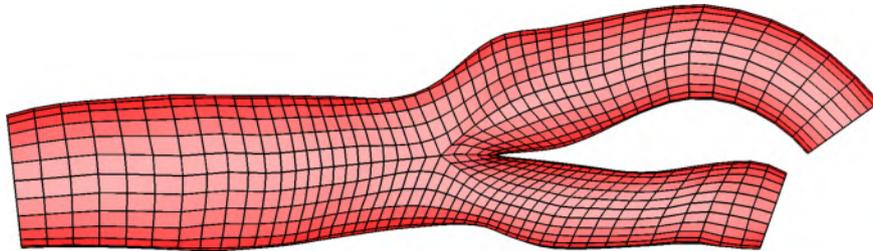
Figure 3.14: Volume mesh inside the outer wall surface (the union of the lumen and wall).

By connecting the inner and outer surfaces, a structured hexahedral mesh of the vessel wall (FEA mesh) is generated (Fig. 3.16). If more layers are needed in the radial direction, to resemble the typical multi-layered arterial wall structure (intima, media and adventitia) or to have multiple elements through the wall thickness, a number of intermediate surfaces, nr, can be generated by interpolation between the inner and outer surfaces.
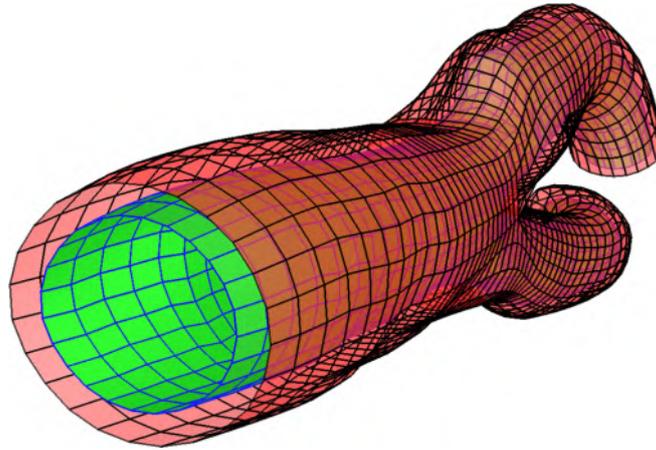
Figure 3.15: Inner and outer wall surface meshes have the same connectivity.

wall mesh: 1,656 cells
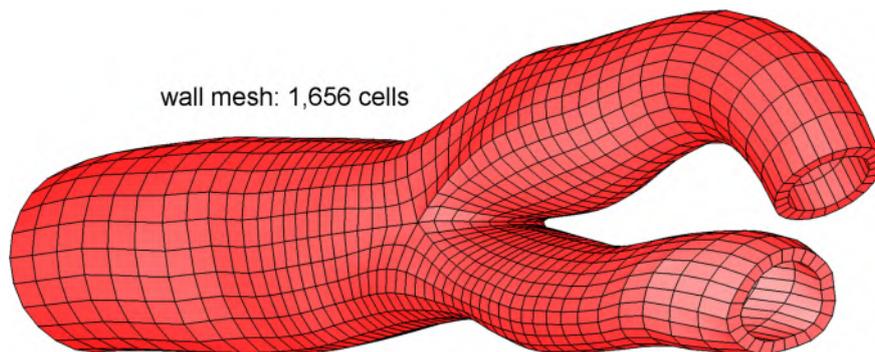
Figure 3.16: By connecting the inner and outer quadrilateral meshes, a structured hexahedral mesh of the vessel wall is generated. The parameters to obtain this coarse mesh, with one hexahedron through the wall thickness, are listed in Table 3.1.

3.2.5   Model accuracy and mesh quality

The geometrical accuracy of the computational mesh can be measured by comparing the lumen surface of the hexahedral mesh (target surface) to the original lumen surface (reference surface), constructed from the segmentation. The distance of the points of the target surface from the cells (triangles) of the reference surface is taken as a measure of accuracy [39]. A high distance between the mesh points and the original surface should be avoided because it indicates that the mesh generation process has strongly distorted the patient-specific geometry.

The quality of the mesh was evaluated using the equi-angle skewness for the CFD mesh [73], and the scaled Jacobian for the FEA mesh [71], as described in Chapter 1.

3.3   Results

3.3.1   Geometrical anisotropy

From a triangulated surface of the lumen of a patient-specific carotid bifurcation, a conformal structured hexahedral mesh is generated in the arterial lumen and wall. The computational mesh is build with differently-sized elements, both in the cross-sectional and longitudinal arrangement. Evaluating the CFD mesh from a cross-section view (radial/circumferential hexahedrons' faces) reveals the change of the element size: by moving away from the centerline to the lumen boundary, large isotropic quadrilaterals become thin and anisotropic quadrilaterals, with the radial edges shorter than the circumferential edges. Evaluating the mesh from a longitudinal view (axial/circumferential hexahedrons' faces) reveals a different length of the longitudinal edges, with longer edges in the tubular regions of the branches and shorter edges inside the bifurcation domain (Fig. 3.11 and 3.16. The possibility of changing the length of the hexahedrons' edges is a property of structured meshes: stretching a hexahedron along the direction of its edges does not degrade the element shape (orthogonal edges remain orthogonal), as shown in Chapter 1, enabling geometrical anisotropy.

3.3.2   Parametric resolution

The CFD mesh is generated using a three-branch topology with the longitudinal resolution defined a priori with the centerlines' seeding parameters (na, nb, nc) and a cross-sectional resolution specified with the quadrilateral pattern parameters (a, b, c). Meshes with higher resolution (Fig. 3.17) can be generated according to the equation:

$$\text{CFD cells} = 4\, a\, (a\, +\, 2\, b\, +\, 2\, c)\, (na\, +\, nb\, +\, nc) \qquad (3.1)$$
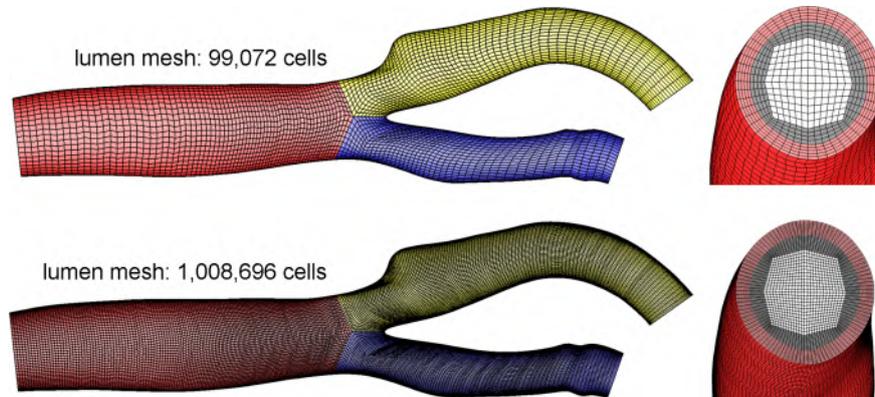
Figure 3.17: By increasing the longitudinal and cross-sectional parameters, the mesh resolution increases. A medium and a high resolution mesh (displayed at the top and at the bottom) are obtained with the sets of parameters listed in Table 3.1.
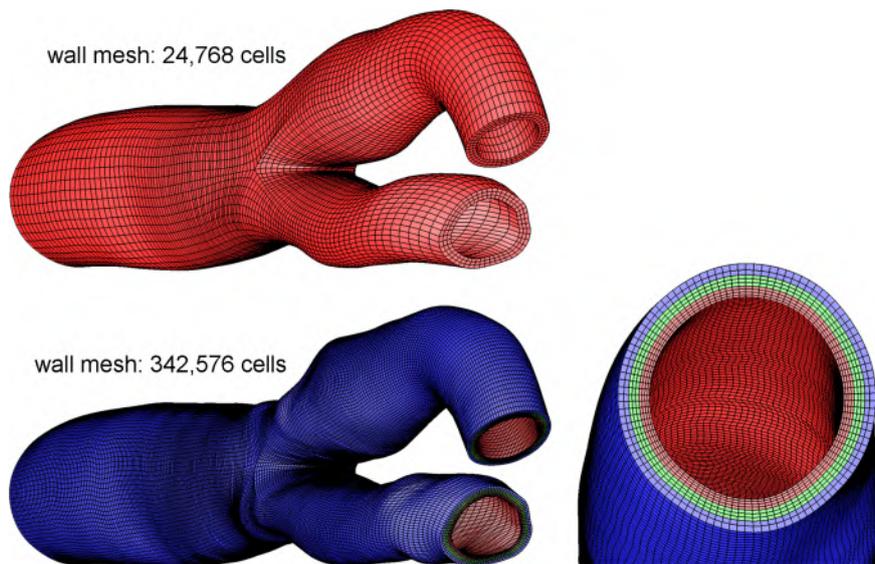
Figure 3.18: (top) Medium-resolution arterial wall meshed with multiple layers of elements in one single structure. (bottom) High-resolution arterial wall meshed with multiple layers of elements divided in layered structures, reproducing the intima, media and adventitia with layer-specific material properties (different layers are coloured by different colors). The sets of parameters to generate these meshes are listed in Table 3.1.

For the FEA mesh, na, nb and nc determine the longitudinal resolution,

a the circumferential resolution and nr the radial resolution, according to the equation:

$$\text{FEA cells} \; = \; 8 \, a \, nr \, (na \, + \, nb \, + \, nc) \qquad (3.2)$$

The number of faces on the wall surface can be calculated with the same equation taking $nr = 1$. By setting the nr parameter, the arterial wall can be discretized with a single layer or with multiple layers (Fig. 3.16 and Fig. 3.18).

3.3.3   Model accuracy and mesh quality

The accuracy of the model, measured using the distance between the triangulated surface and the volume mesh boundary, is on average three orders of magnitude smaller than the vessel diameter, with a maximum of 164.6 μm (2% of the smaller vessel radius). The peak distance is found on the shoulder of the stenosis located on the outer edge of the ICA, which is a highly curved region (Fig. 3.19). By increasing the number of semi-planes used to slice the surface, the accuracy improves (distance lower than 54.9 μm, 0.7% of the smaller radius) but up to a threshold, because of the fixed number of splines used to reconstruct the vessel branches (24 splines around one cross-section) .
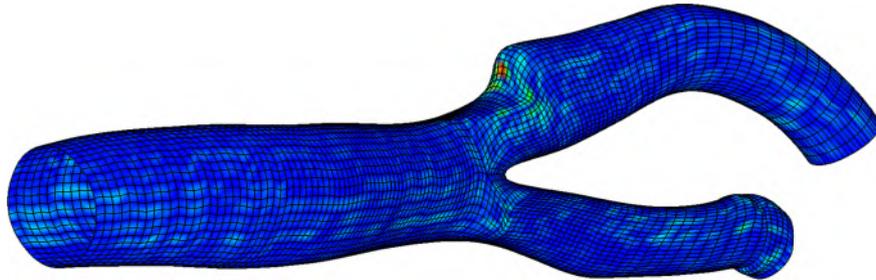
Figure 3.19: The average distance between the nodes of the mesh surface and cells of the original triangulated surface is in the order of micrometers. The highest difference is located on the proximal side of the stenosis. The displayed surface is the boundary of the medium-resolution hexahedral mesh with blue and red corresponding to the values reported in Table 3.1.

The skewness of the CFD mesh is on average below 0.25, which is optimal for the computation using hexahedral meshes (a hexahedral cell is optimal if the

Qeas < 0.4 [110]), and the scaled Jacobian of the FEA mesh is on average above 0.8, meaning that elements' distortion is low. Worst elements in the lumen and wall are still adequate for the computational analysis (maximum skewness 0.75 and minimum scaled Jacobian 0.18, see Chapter 1).

3.4 Discussion

The Bifmesh, a straightforward approach to generate a conformal full-hexahedral mesh of the arterial lumen and wall from a triangulated surface model, is implemented and tested on the lumen and wall of a carotid artery bifurcation. The mesh boundary accurately reproduces the patient-specific geometry and matches the original triangulated surface model with micro-metric accuracy. The elements have high shape quality, enabling accurate CFD and FEA investigations.

With respect to the mesh generated in Chapter 2, which applies to surface models consisting of series of circular sections, the Bifmesh applies to trian-gulated surface models (STL file format) obtained with the most common segmentation algorithms. Comparing structured meshes with unstructured meshes has shown that structured meshes are beneficial for the accuracy of the results and the computational costs. When cells are oriented along the direction of the predominant flow (alignment of the mesh gridlines with the streamlines) the computational error, owing to the numerical diffusion occurring during the integration of the flow equations, is reduced, thus providing higher accuracy of the results [73, 103, 104].

In FEA, a structured mesh of the arterial wall allows using anisotropic elements with a lower radial dimension as compared to longitudinal and circumferential dimensions. Stretched elements are preferred for the stress analysis in case of pressurized tubular structures like arteries [52]. Addi-tionally, the arrangement of the elements in longitudinal, circumferential and radial direction enables to define triad axes in each hexahedron which are coherent with the global shape of the vessel and can be used to define a material structural anisotropy, including the effect of counter-rotating helices of collagen fibers with layer-specific pitch angles [50].

Despite their limitations, mainly unstructured meshes have been used in patient-specific CFD and FEA, because they can be automatically gen-erated in nearly any geometry (using common software packages such as Abaqus CAE, Gambit, TGrid and Tetgen [107, 110, 111]). Generation of hexahedral meshes is more difficult and generally requires extensive opera-tor interaction which can be prohibitively time-consuming [39]. A strategy for structured mesh generation in the carotid artery lumen based on longi-

tudinal splines was developed by Long et al., [60] and by Antiga et al. [61]. In 2005, an original automatic hexahedral meshing tool for the lumen of vascular bifurcations has been developed by Verma and collaborators [62]. This method requires a preliminary unstructured mesh generation in the arterial lumen for the numerical solution of heat-conduction problems. Then, a structured mesh is generated using the thermal iso-surfaces to define the structure. A drawback of this approach is that it requires solving a simulation on unstructured grids, requiring an external solver and, therefore, adding computational time to the mesh generation. In the same year, Wolters and colleagues have shown that hexahedral mesh generation in an aortic bifurcation could be performed by fitting an original template inside the vessel surface. They used centerlines for an initial fitting of a pre-meshed structure, Laplacian smoothing to improve the element shapes, and an incremental procedure to deform the mesh to the real vessel surface [56]. With respect to the above described meshing strategies, in our study we have extended the mesh generation to the wall and improved the circumferential arrangement of the cells (smooth connections of the gridlines from the two semi-slices in each branch). However, the main novelty of the Bifmesh is the GUI which allows a non-expert user to mesh the vessel lumen and wall in a timescale of seconds, with only few clicks required, following a standard procedure documented in a tutorial (see a demonstrative movie on YouTube [112]).

Thanks to the pure geometrical construction of the mesh, the Bifmesh is a simple and robust tool and has the potential to serve for large population and longitudinal image-based investigations. The user can design the mesh based on the expected solution, increasing the resolution of the mesh where higher accuracy is needed by altering a set of parameters (e.g. higher radial resolution near the wall and higher longitudinal resolution in the central region of the bifurcation).

On the one hand, the fixed topology consisting of six semi-branches enables a fast and graphical mesh generation procedure. On the other hand, it reduces the applicability of the Bifmesh to bifurcating vessels. In case of a vessel with multiple bifurcations, the Bifmesh could still be effective if the domain is split into single-bifurcations. However, general topologies, such as trifurcations, cannot be meshed using the Bifmesh. A second limitation is the limited geometrical accuracy. We have shown that the geometrical accuracy of the mesh is adequate for the computational analysis (mesh-to-surface distance is in the order of micrometers), but it cannot be decreased below a threshold, owing to the fixed number of splines used to reconstruct the vessel surface circumferentially.

A more general and accurate mesh generator is presented in Chapter 4, where the surface cutting and spline reconstruction are replaced by the

block mapping and nodal projection. Nevertheless, more general tools also require higher expertise and longer meshing time. Applications of the Bifmesh tool will be presented in Chapter 5, including modelling carotid and coronary artery stenting, investigating the flow in an arterio-venous graft and an aortic arch, and simulating the fluid-structure interaction in a carotid artery with a compliant wall.

Chapter 4

Treemesh: multi-block hexahedral mesh generation in a complex vascular tree

THE feasibility of structured mesh generation for image-based analysis in vascular applications has been demonstrated in the previous chapters: a vascular tree with multiple bifurcations and tubular branches (i.e. a coronary artery modeled as a sequence of circular sections reconstructed from biplane angiography) was the subject of Chapter 2 and a full graphical implementation of the mesh generation in case of a nearly-planar bifurcation (i.e. a carotid artery modeled as a triangulated surface reconstructed from CT angiography) was the subject of Chapter 3. Despite some differences (in the first case the surface file format already provided the cross-sections whereas in the second case the cross-sections were extracted by slicing the surface), a sweeping-based mesh, topologically equivalent to sweeping a quadrilateral section along a path, was generated in both cases. However, the sweeping-based approach is restricted to specific vascular topologies (a single vessel, a bifurcation, or a combination of the two). As such, the problem of meshing a (complex) vascular region remains unsolved.

This Chapter presents a novel approach to mesh generation which does not rely on sweeping and can be applied to mesh both the lumen and wall of complex vascular geometries, such as bifurcations, trifurcations, and stenotic and aneurysmatic regions. The vascular-tree mesher (abbreviated as 'Treemesh') integrates a centerline-based description of the vascular network with a multi-block mesh construction. The robustness of this tool with respect to the complexity of the vascular geometry will be tested on challenging cases of interest in biomedical research both in this chapter and

Chapter 5[1].

4.1   Introduction

Direct access to local blood flow and vessel wall stress in vivo is difficult because of the limited spatial and temporal resolution offered by the current imaging modalities. Image-based analysis is an indirect approach to compute accurate spatial and temporal data in vivo by modeling the physical system of interest with a set of partial differential equations, in which the computational domain is reconstructed from medical images (CT, MRI, US) and the boundary conditions are measured on the patient or assumed from average physiological data. Mesh generation is a critical step in image-based modelling and a standard meshing procedure is not yet established.

In Chapter 2 we have investigated on a real case the trade-off existing between the simplicity of the mesh generation and the computational performance of a mesh in terms of accuracy and computational run time [73]. An automatic mesh generator allows the user to easily fill the computational domain with tetrahedrons and prisms in an unstructured fashion. However, such a mesh does not take into account the physics that needs to be modeled and may introduce numerical inaccuracy. A structured mesh is difficult to generate but can be tailored on the simulated physics. For example, modeling blood flow in arteries using CFD benefits from the alignment between the computational cells (and gridlines) and the predominant flow because of a lower numerical diffusion error; similarly, modelling the pressure load and stent expansion in an arterial wall using FEA benefits from a mesh constructed as a series of concentric layers because of a better resolution of the stress gradients along the wall thickness. As a result, a hexahedral structured mesh significantly improves the computation and, when feasible, should be preferred to an unstructured mesh.

To facilitate the generation of a structured mesh in a vascular domain, we have developed a general tool, the Treemesh, which combines the vessel centerlines with multi-block structured meshing. The efficacy and the flexibility of the Treemesh are proven on two cases, an aortic arch and an abdominal aortic aneurysm, with a specific focus on the elements' quality and the mesh-generation time.

---

[1] The content of this chapter was published in the journal, Medical Engineering & Physics:
Full-hexahedral structured meshing for image-based computational vascular modeling
G. De Santis, M. De Beule, K. Van Canneyt, P. Segers, P. Verdonck, and B. Verhegghe
in press (available online)

4.2 Materials and methods

Two open-source software packages, the Vascular Modeling Toolkit (VMTK) [47] and pyFormex [75], are used for the implementation of a four-step procedure (subsections 4.2.2 4.2.3 4.2.4 4.2.5), required to generate a volume mesh of the lumen and wall, starting from a triangulated surface of an image-based vascular model. The method is explained in detail on a human aortic arch, imaged with MR angiography, and then applied to an abdominal aortic aneurysm, imaged with CT angiography.

Figure 4.1: A triangulated surface model of an aortic arch obtained by segmenting an MR angiography image.

4.2.1 Image segmentation

An ostensibly healthy aortic arch imaged with MR angiography is segmented in VMTK, generating a triangulated surface model (Fig. 4.1). After clipping the surface, cylindrical extensions are added in the direction of the centerlines in order to provide circular borders for the applications of the boundary conditions and enable flow development (Fig. 4.2) [39].
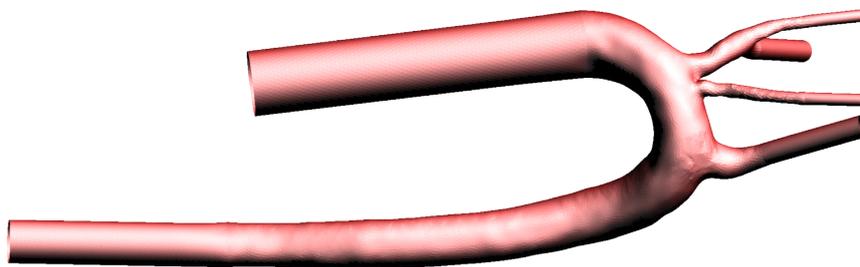
Figure 4.2: Cylindrical surface extensions are attached to all boundaries in the direction of the centerlines.

4.2.2   Centerline-based synthetic geometrical descriptors

The aortic model with the flow extensions (STL format) is analyzed in VMTK in order to extract three synthetic descriptors of the 3D structure: centerlines, radii and parallel transport normals. The vessel centerlines associated to a vessel surface describe the longitudinal evolution of the vessel branches (tube-like structures) and were computed in Chapter 3 by slicing the surface and storing the centers of the slices. However, there is no unique implementation of the centerlines. In VMTK the centerlines are determined as the paths on the Voronoi diagram that minimize the integral of the radius of the maximal inscribed spheres along the path (i.e. the shortest paths in the radius metric). Each point of the centerline is then equipped with a local radius, which is the radius of the maximal inscribed sphere, and a triad axes (local reference system). The local axes are the abscissa (unit vector tangent to the centerline), the normal (a vector perpendicular to the centerline) and the binormal, which can be calculated as the cross product of the abscissa and normal.While the definition of the abscissa is straightforward, the normal in a set of curved and interconnected lines cannot be calculated using the local curvature (Frenet theory), as it would result undefined on straight segments and would experience abrupt changes in its orientation whenever the osculating plane changes (the osculating plane of a curve in a point is the plane that approximates the curve in the neighborhood of that point with second order contact). According to the implementation inside VMTK, the normal is defined as a parallel transport normal, being a unit vector perpendicular to the centerline which rotates on the osculating plane of an angle equal to the change of orientation of the centerline tangent while walking along the centerline. This iterative procedure defines an angular orientation along each centerline (i.e. circumferential position) without introducing artificial torsion. Each centerline's normal is then rigidly rotated to match the normals of the adjacent centerlines, using the first bifurcation as a landmark. This procedure provides the geometrical and topological descriptors of the vasculature, is automatic and applies (among others) to highly non-planar geometries which are difficult to slice. For these reasons, it has been selected as a preliminary step for the mesh generation (Fig. 4.3).

4.2.3   Block-structures in the lumen

The synthetic descriptors of the vasculature (centerlines, equipped with maximal inscribed-sphere radii and parallel transport normals), are processed in pyFormex to build a number of block-structures. The centerlines are first down-sampled because only few points per vessel branch are sufficient for the construction of the blocks. The triad axes and the local radius

of a point are used to construct a square around the vessel aligned normally with respect to the centerline tangent. The result is a series of squares that twist according to the curvature of the vessel (computed with the method of the parallel transport normal) and scale according to the local radius (Fig. 4.4).
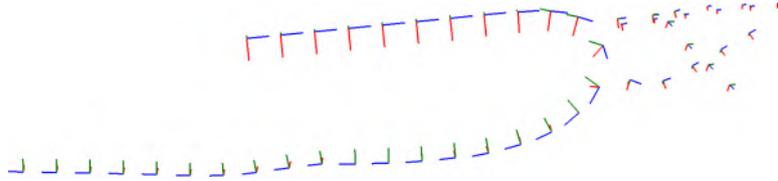
Figure 4.3: When moving along the centerlines, the triad axes (blue, green and red lines correspond to abscissa, parallel transport normal and binormal) twists according to the rotation of the centerline tangent. The vectors representing the triad axes are scaled according to the local vessel radius.
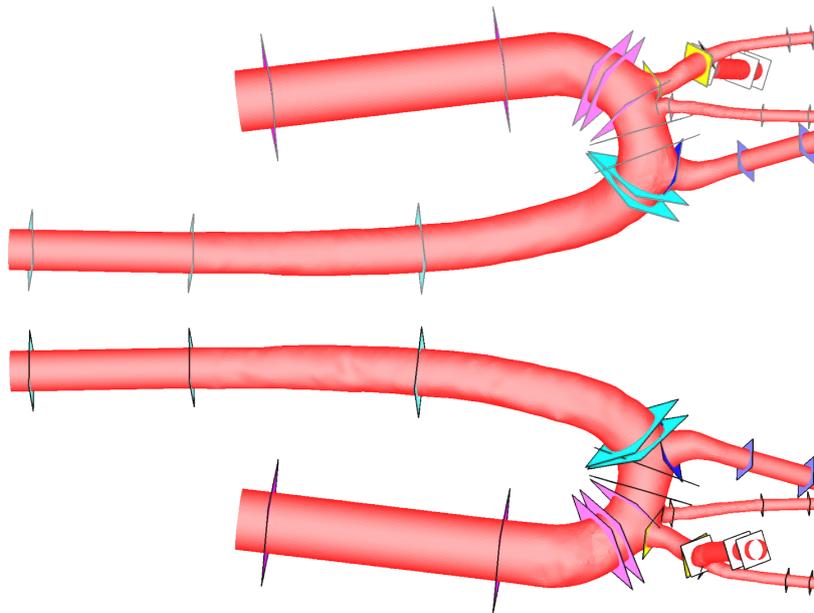
Figure 4.4: Front (ventral) and back (dorsal) side of the aortic arch with a series of squares constructed around the surface using the centerline-based synthetic descriptors of the vasculature.

By interconnecting the squares of a branch and joining the branches, a number of block-structures are obtained. Because the centerlines describe the vessel as a series of tubular branches without taking into account the

geometrical detail of the vessel surface, the block-structures conform to the vessel surface where the vessel is nearly tubular and curved with high radius of curvature, but may intersect the surface in more complex regions. For example, on the back side of the aortic arch, the vessel torsion, the combination of multiple bifurcations and the different radii of the branches produce few distorted blocks that intersect each other or intersect the vessel surface, as shown in Fig. 4.5. In this event, the user needs to displace few points to manually adapt the block-structures to the surface.
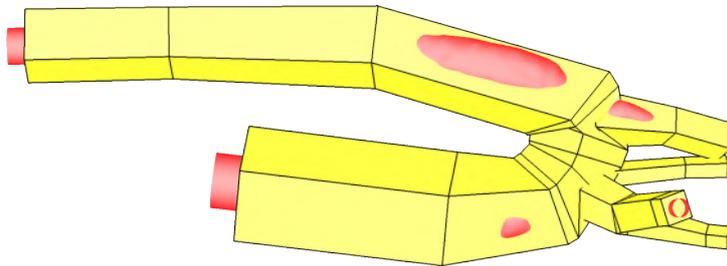
Figure 4.5: In the regions of branching the block-structures obtained by connecting the squares (in yellow) intersect the surface (in red), requiring manual correction.

The user separates the block-structures into a set of Nrb blocks, corresponding to the real domain, and a set of Nxb blocks, corresponding to the flow extensions. The number of daughter vessels, Ndv, is a parameter related to the vascular tree and characterizes the topology of the block-structures (Fig. 4.6).
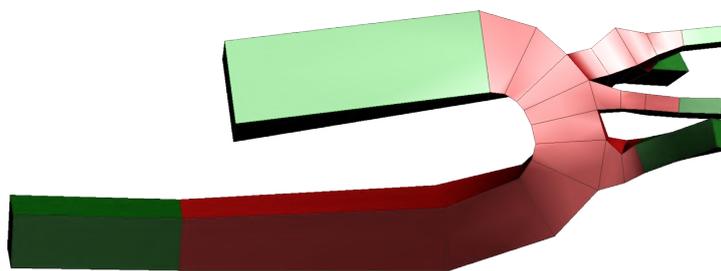
Figure 4.6: The block-structures are grouped into real domain ($\mathsf{Nrb} = 20$, in red) and flow extensions ($\mathsf{Nxb} = 6$, in green). From the main vessel (the aorta) four daughter vessels originate ($\mathsf{Ndv} = 4$).

By scaling the external block-structures, internal block-structures are constructed in the volume between the vessel surface and the centerlines. The two sets of block-structures (internal and external) are topologically-equivalent and are converted into quadratic blocks by inserting an additional node in the middle of all edges.

4.2.4 Projection and lumen mesh generation

The outer surfaces of the internal and external block-structures represent two sets of quadratic quadrilateral patches. The external patches (outer surface of the external block-structures) can be projected towards the corresponding inner patches (outer surface of the internal block-structures) onto the triangulated surface model of the vessel. As a result, a quadrilateral mesh of the lumen surface is generated (Fig. 4.7).
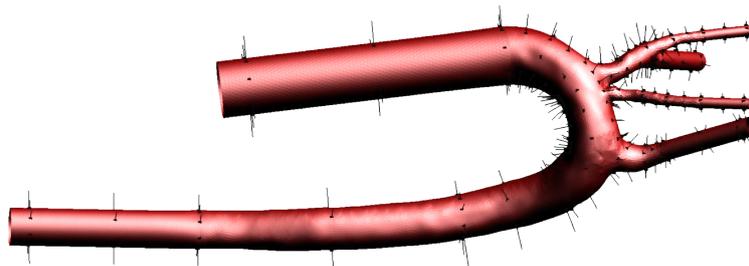
Figure 4.7: By point-to-point projection, the external patches are projected onto the patient-specific triangulated surface, generating a quadratic quadrilateral surface mesh of the vessel.
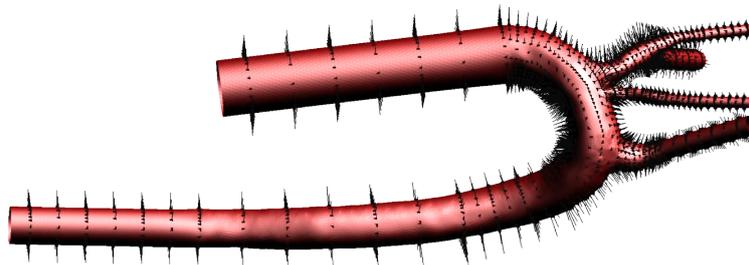
Figure 4.8: The number of patches projected from the external surface mesh onto the triangulated model is increased with a factor Pbe = 3, as compared to the patches used in Fig. 4.7, in order to improve the geometrical accuracy of the final mesh.

To decrease the distance between the quadrilateral surface mesh and the original triangulated model, improving the geometrical accuracy, a higher number of patches (and projection points) can be set by isotropically splitting with a factor `Pbe` all the block-structures before projecting (Fig. 4.8).
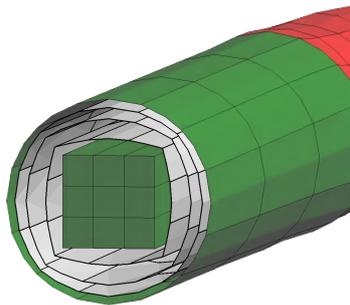
Figure 4.9: Between the surface of the internal blocks and the lumen surface, a number of layers (`Pbl`) can be generated, designing the cross-sectional near-wall mesh resolution.

To fill the volume between the internal blocks and the surface of the vessel, the quadrilateral mesh of the lumen surface is connected to the topologically-equivalent surface of the internal blocks, generating new block-structures. These new blocks, arranged in groups of four blocks around one internal block, can be refined in the radial direction by adding `Pbl` layers, to have a finer near-wall mesh (Fig. 4.9). As a result, a quadratic hexahedral mesh of the vessel lumen is obtained (Fig. 4.10). The quadratic volume mesh of the lumen can then be converted into a linear mesh of desired resolution by isotropic refinement, using a factor `Pil`, and then exported for the CFD calculation.
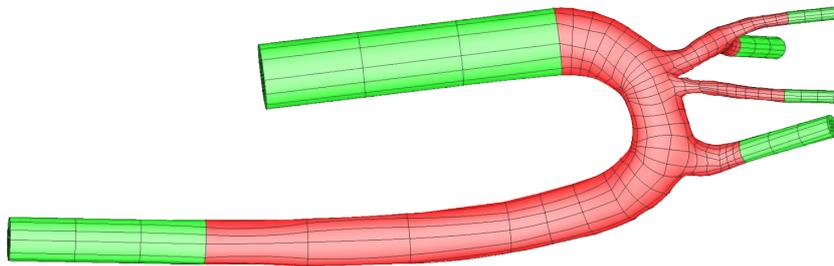
Figure 4.10: The union of the quadratic internal block-structures and the quadratic near-wall block-structures represents a quadratic structured hexahedral mesh of the vessel lumen.

4.2.5   Vessel wall reconstruction and mesh generation

After meshing the lumen, the mesh in the arterial wall can also be gener-
ated. When the (outer) wall surface is provided, it is trivial to construct a
quadratic quadrilateral surface mesh of the external wall surface by repeat-
ing the projection described in section 4.2.4. However, in most cases the
entire wall surface is not available and needs to be reconstructed by either
assigning a constant wall thickness or, more realistically, by assigning a
radius-dependent wall thickness, computed from the local surface distance
from the centerline (Fig. 4.11) [8, 52, 113]. The wall surface can be obtained
by displacing the nodes of the quadrilateral lumen surface towards the
nodes of the surface of the outer blocks of a distance equal to the wall
thickness (constant or radius-dependent). For the aorta, a factor 1/3 was
chosen as a ratio between the local wall thickness and the local radius of
the aortic arch, following the anatomical data reported in literature [114]
(Fig. 4.12).
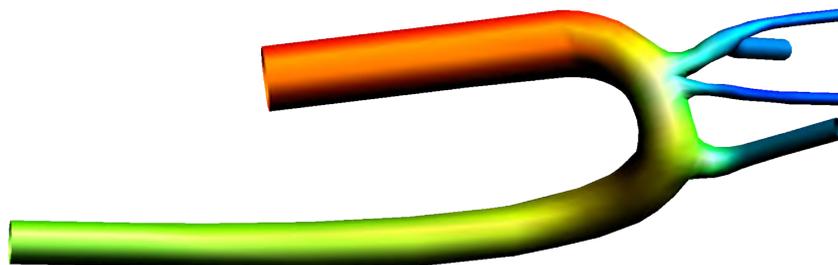
Figure 4.11: The local distance of the surface nodes from the centerline (local
radius) is plotted on the surface (blue and red indicate minimal and maximal
radii, respectively).

From the topological equivalent lumen and wall surface meshes (with the
wall reconstructed either from medical images or using anatomical data) a
volume mesh can be generated by surface mesh connection. The quadratic
surfaces can be refined with a factor P_{sw}, before connecting them. Addi-
tionally, by interpolating a number P_{rw} of layers between the inner and
outer surfaces, a multi-layered hexahedral mesh can be generated, repeat-
ing the operation shown in Fig. 4.9 and described in section 4.2.4. The
concentric layers can be then grouped in three sets, to resemble the layered
vessel-wall structure (intima, media and adventitia). The quadratic volume
mesh of the wall can be converted into a linear mesh of desired resolution
by isotropic refinement, using a factor P_{iw}, and then exported for FEA
calculations.
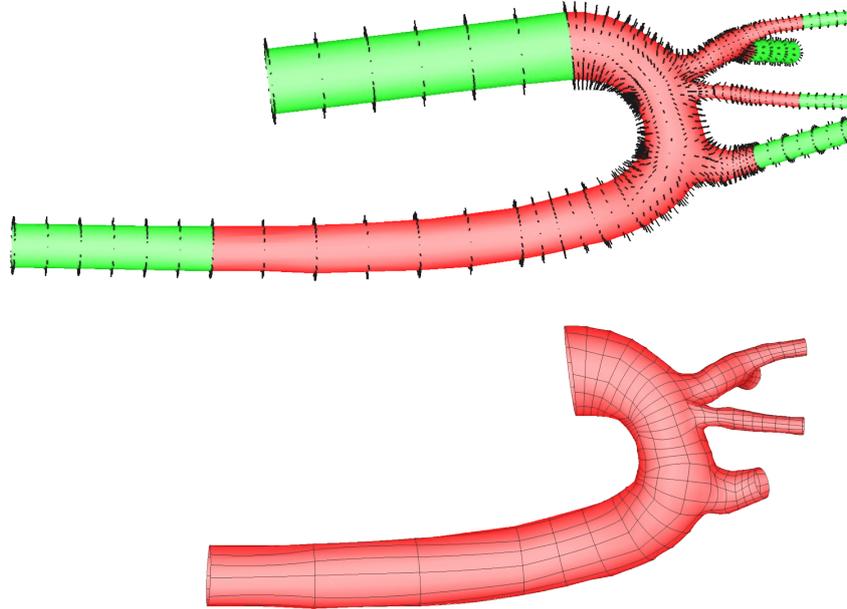
Figure 4.12: By displacing the nodes of the quadrilateral lumen surface outward of a distance equal to 1/3 of the local vessel radius, the wall surface is artificially reconstructed. The flow extensions are removed from the wall surface because they are usually not needed for a structural analysis.

4.2.6 Remesh

The parameters used for the mesh generation of the lumen and wall are listed in Table 4.1. The topological parameters $(\mathsf{Nrb}, \mathsf{Nxb}, \mathsf{Ndv})$ depend both on the vessel topology and on the way the block-structures are constructed. The projection parameter (Pbe) determines the number of patches to project, influencing the geometrical accuracy. The other parameters are specific for the mesh resolution in the lumen $(\mathsf{Pbl}, \mathsf{Pil})$ and in the wall $(\mathsf{Prw}, \mathsf{Psw}, \mathsf{Piw})$. By keeping the same topological parameters (keeping the same block-structures) and changing the other parameters, new meshes with different accuracy and resolution can be generated. Thanks to the structured nature of these meshes, the number of elements can be calculated from the sets of parameters using the equations reported in Table 4.2.

After generating an initial mesh, new meshes can be generated by remeshing (refining or coarsening) either before projection (modifying the Pbe) or after projection. The difference between the two approaches is first shown on a simple model (a sphere) and then on the aortic arch.

Table 4.1: Parameters used to design the mesh of a blood vessel. The capital letters in the third column (Description) indicate the letters used in the abbreviations. N = number, P = parameter.

Type	Abbreviation	Description
Topology	Nrb	N of Blocks in the Real domain
Topology	Nxb	N of Blocks in the flow eXtensions
Topology	Ndv	N of Daughter Vessels
Projection	Pbe	P for isotropic refinement BEfore projection
CFD	Pbl	P for Boundary layers of the Lumen
CFD	Pil	P for Isotropic refinement of the Lumen
FEA	Prw	P for Radial layers of the Wall
FEA	Psw	P for Surface refinement of the Wall
FEA	Piw	P for Isotropic refinement of the Wall

The geometrical accuracy of the final mesh is evaluated as the distance between the points of the mesh surface and the faces of the triangulated surface model. The quality of the mesh is measured using the equiangle skew for the lumen and the scaled Jacobian for the wall, as described in Chapter 1. As an additional application of the Treemesh, a mesh is generated in an abdominal aortic aneurysm reconstructed from a CT angiography.

Table 4.2: The number of projected patches and the mesh resolution can be calculated a priori by setting some parameters. N = number.

Mesh resolution	Equation
N of projected patches in the real domain	$(4\,\mathrm{Nrb} - \mathrm{Ndv})\mathrm{Pbe}^2$
N of projected patches in the flow extensions	$(4\,\mathrm{Nxb})\mathrm{Pbe}^2$
N of cells in the real lumen	$(\mathrm{Nrb}\,\mathrm{Pbe}^3 + (4\,\mathrm{Nrb} - \mathrm{Ndv})\mathrm{Pbe}^2\,\mathrm{Pbl})\mathrm{Pil}^3$
N of cells in the flow extensions	$(\mathrm{Nxb}\,\mathrm{Pbe}^3 + 4\,\mathrm{Nxb}\,\mathrm{Pbe}^2\,\mathrm{Pbl})\mathrm{Pil}^3$
N of cells in the wall	$(4\,\mathrm{Nrb} - \mathrm{Ndv})\mathrm{Pbe}^2\,\mathrm{Psw}^2\,\mathrm{Prw}\,\mathrm{Piw}^3$
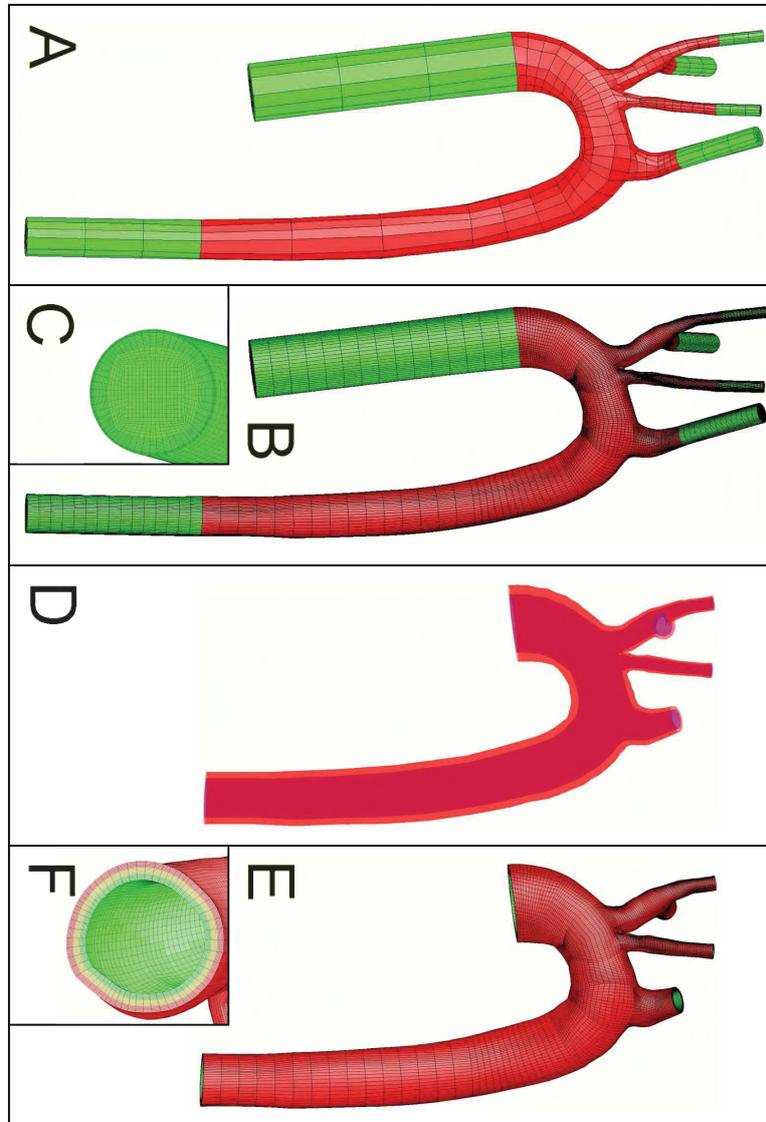
Figure 4.13: From a triangulated surface model of the lumen of an aortic arch, a structured hexahedral mesh is generated in the lumen and wall. An initial quadratic mesh with the real domain and flow extensions separated into two different element sets (A) is converted into a finer linear mesh (B), with a butterfly arrangement of the cells in the cross-section (C). By computing the surface distance form the centerline, the nodes of the vessel surface are equipped with the local radius of the maximal inscribed sphere (a measure of the local vessel size, D). By displacing the lumen surface by a fraction of the local radius, the mesh in the wall is generated (E), with multiple layers, resembling the arterial tunicae (F).

4.3 Results

4.3.1 Multi-block mesh generation

Using the Treemesh, a structured hexahedral mesh was generated inside the lumen of a human aortic arch, by arranging a central block surrounded by four lateral blocks on a cross-section, as displayed in Fig. 4.13 C. In order to separate the aortic domain from the artificial extensions, the elements of the aortic lumen were grouped in two sets (Fig. 4.13 A, B). To generate a mesh of the arterial wall, the outer surface of the wall could not be extracted from the medical image, and needed to be reconstructed from anatomical data: distal-to-proximal tapering was taken into account by assigning a wall thickness equal to 1/3 of the local radius (Fig. 4.13 D, E). The wall mesh in the aortic arch model included three layers resembling the intima, media and adventitia (Fig. 4.13 F), with the same longitudinal and circumferential topology of the mesh in each layer. As a result, a conformal match between the mesh of the lumen and wall was achieved (Fig. 4.13 C, F).
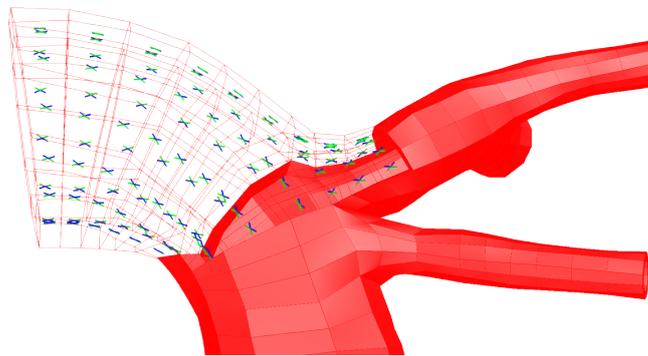
Figure 4.14: The directions of the collagen fibers in the arterial wall can be defined based on the orientation of the elements in a structured mesh. Two systems of helices rotate clockwisely and counter-clockwisely around a branch's centerline.

Each element of the aortic wall was equipped with longitudinal (distal to proximal), circumferential (counterclockwise rotation around the centerline) and radial (inner to outer) directions, by using the vectors connecting the centers of opposite faces of each hexahedron. Using this hexahedron-specific cartesian coordinate system constructed from the cylindrical coordinate system of the vessel, the direction of counter-rotating helical collagen fibers inside the wall could be defined, as previously reported by Mortier et al. [50].

As an example, Fig. 4.14 displays the helices produced using an opening angle of 70 degrees from the circumferential vector on the plane normal to the radial direction).
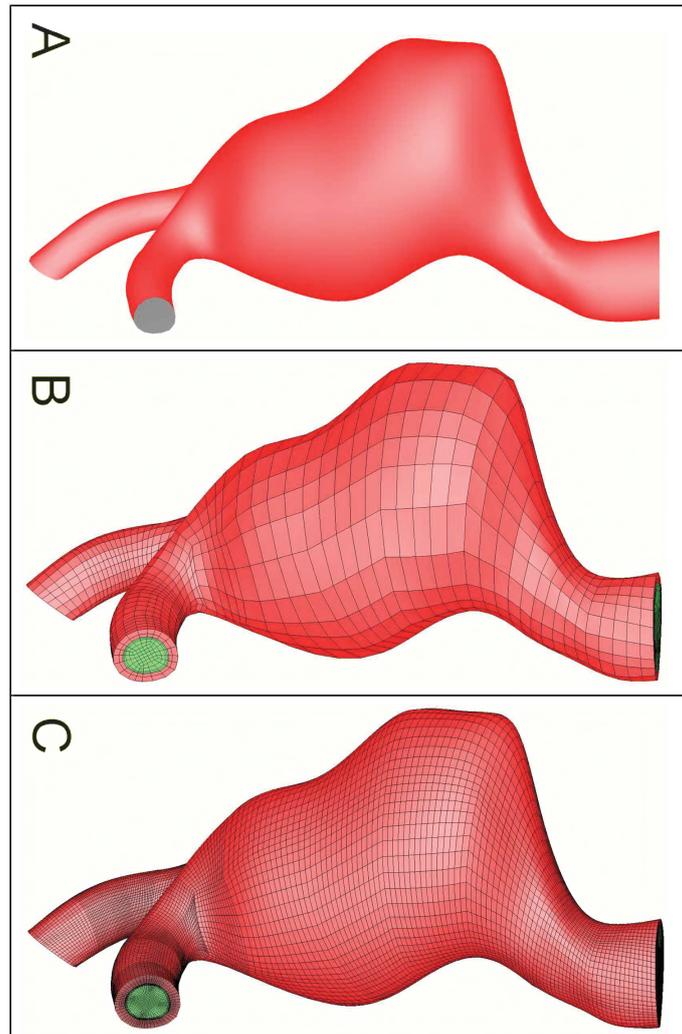
Figure 4.15: From the lumen surface of an abdominal aortic aneurysm (A), a coarser mesh (B) and a finer mesh (C) are generated in the lumen and in the wall.

The mesh generation procedure described in detail for the aortic arch was

repeated for an abdominal aortic aneurysm. With respect to the mesh generated for the aortic arch, flow extensions were not added to the lumen (Nxb = 0), the aneurysmatic wall was reconstructed without layers, the tapering was not taken into account and a constant thickness of 1 mm was assigned to the entire wall. This choice was motivated by the pathological radius of the aneurysm, which would have produced an abnormally thick wall (Fig. 4.15).

4.3.2 Parametric mesh resolution

The volume mesh inside the lumen was generated with a combination of mapping, projection and refinement operations. By selecting the number of patches to project and the refinement after projection, the accuracy of the final mesh with respect to the original surface could be regulated. The difference between the pre-projection and post-projection re-meshing can be illustrated on a perfect spherical surface (Fig. 4.16 A), discretized into a coarse triangulated model (Fig. 4.16 B). Such a model is meshed with the same number of elements but using two sets of parameters, reported in Table 4.3, one set prescribing a refinement before projection (Fig. 4.16 C) and the other prescribing a refinement after projection (Fig. 4.16 D). A visual evaluation suggests that the mesh refined before projection does better resemble the triangulated sphere, inheriting the sharp edges of the triangles, while the mesh refined after projection does better resemble the original ideal sphere.

Table 4.3: Parameters to mesh a sphere with a refinement before and after projection. While a single branch has 0 daughter vessels, the sphere has Ndv = -2 for the calculation of the resolution because it misses both an inlet and an outlet.

Parameters	Refined before projection	Refined after projection
Nrb	1	1
Ndv	-2	-2
Pbe	24	2
Pbl	12	1
Pil	1	12
N of projected patches	3,456	24
N of projected points	10,370	74
N of cells	55,296	55,296
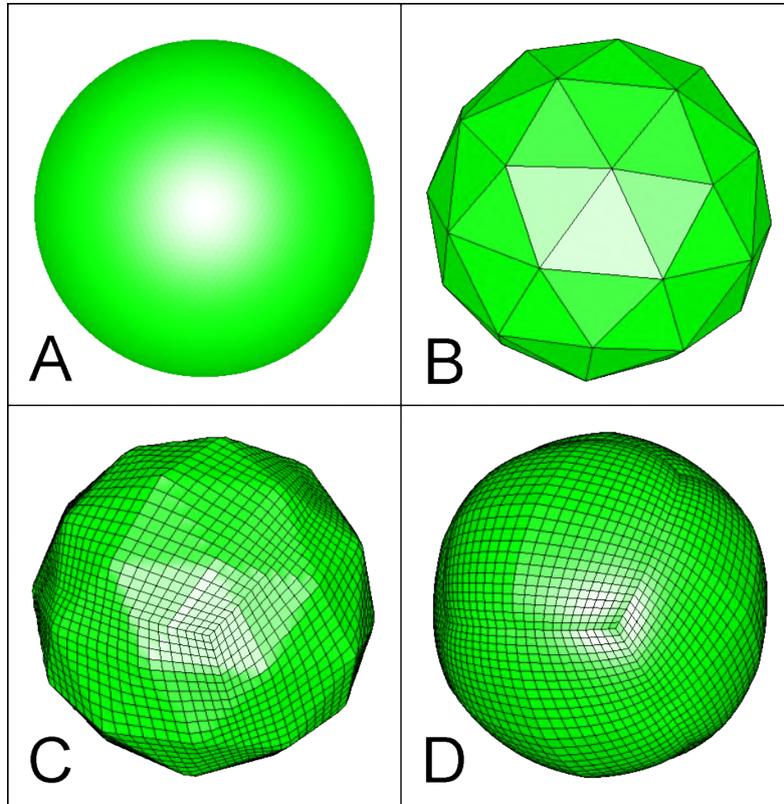
Figure 4.16: In the Treemesh curved (parabolic) patches are projected on the triangulated (linear) surface model (B) of an object (A). If the patches are larger than the surface triangles the projected patches reproduce the curvature of the object and such a curvature remains after an arbitrary refinement of the projected patches (refinement after projection, D). If the patches are smaller than the surface triangles the projected patches are straightened on the triangles and the curvature is lost (refinement before projection, C). In this case, the mesh inherits the edges of the coarse triangulated model (finite angles between adjacent triangles), as visible in (C).

4.3.3   Mesh refinement

Two meshes of the lumen and wall of an aortic arch and an abdominal aortic aneurysm have been generated starting from the same blocks (same topology) and the same number of projections, but different CFD and FEA sets of parameters (different refinement after projection), as listed in Table 4.4. In all meshes, the (local) geometrical error, quantified as the distance between the surface nodes of the meshed lumen and the original

triangulated surface, was lower than one micron, thus close to the numerical (round-off) error of the computation infrastructure. The average equiangle skew of the lumen was below 0.4 (Fig. 4.17), which is optimal for CFD applications [61], and the average scaled Jacobian of the wall was higher than 0.8, which is optimal for FEA applications [71] (Fig. 4.18).
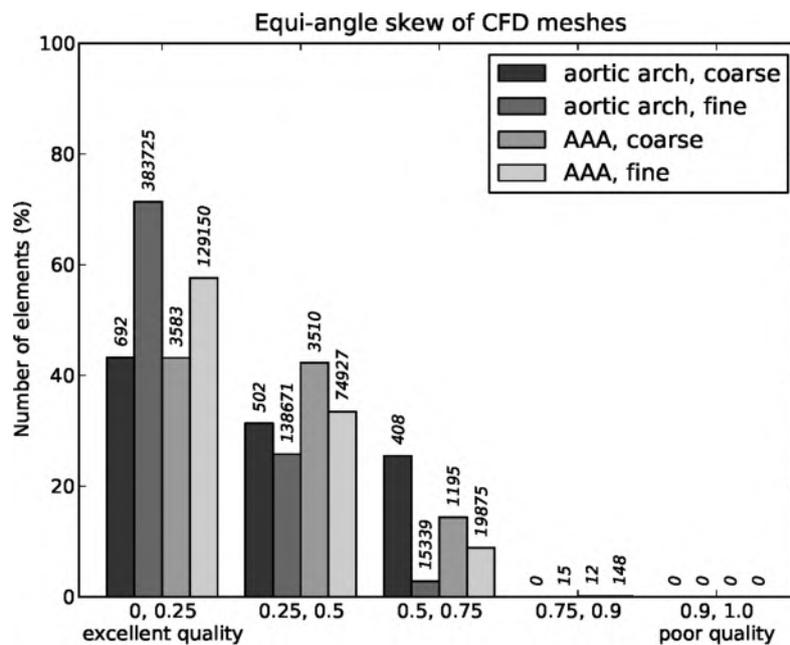
Figure 4.17: Distribution of the equiangle skew for the meshes of the lumen of the aortic arch and abdominal aortic aneurysm (mesh features reported in Table 4.4).

The initial mesh generation required 4 hours for the aortic arch and 0.5 hours for the abdominal aortic aneurysm, and most of the time was spent to adjust the block-structures in the regions of high curvature and branching. For comparison, the segmentation process required one day work for the aortic arch and few hours for the abdominal aortic aneurysm. After the first mesh generation, the parametric nature of the structured mesh allowed a re-meshing without altering the mesh topology (recycling the previously generated blocks) in a matter of minutes. To increase the mesh density, the block-structures could be refined before projection or after projection. In the former case, the finer mesh was expected to improve the surface representation but degrade the element quality whereas in the latter case the finer mesh was expected to corrupt the geometrical accuracy but preserve

the element quality. The difference in accuracy using the two strategies was found not to be relevant: increasing the number of elements by two orders of magnitude (multiplying the number of elements by a factor 256 corresponds to shortening the elements' edges by a factor 8) by refinement after projection, preserved the geometrical accuracy below one micron.
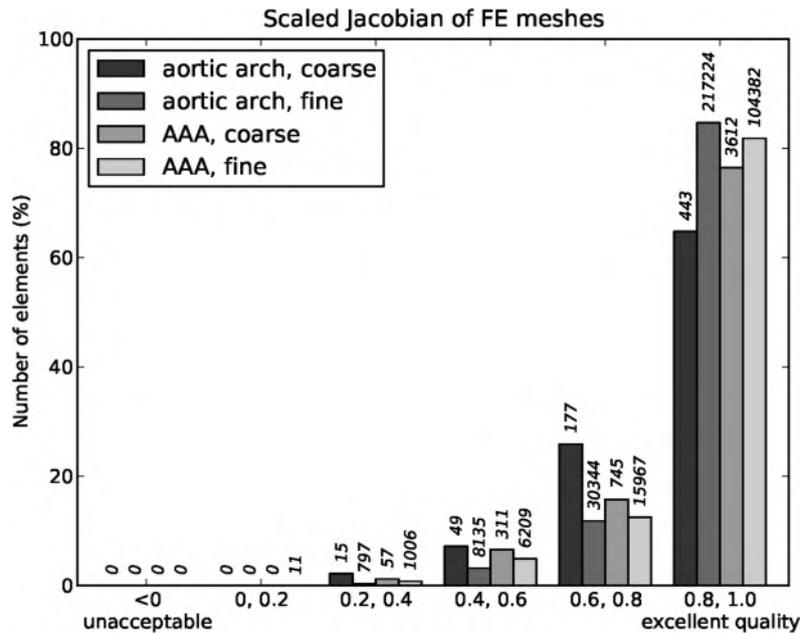
Figure 4.18: Distribution of the scaled Jacobian for the meshes of the wall of the aortic arch and abdominal aortic aneurysm (mesh features reported in Table 4.4).

To test whether a refinement before projection would compromise the mesh quality, we have generated a third mesh of the aortic arch by increasing the quadratic patches from 900 to 4,900, thus increasing the number of projected points from 2,768 to 14,864 (generating 769,986 and 301,644 cells in the lumen and in the wall, respectively). The average and maximum value of the equiangle skew did not change (0.195/0.759 and 0.188/0.763 for the lumen reconstructed with 900 and 4,900 patches, respectively) and the average and minimum value of scaled Jacobian was found 0.90/0.27 and 0.90/0.21 for the wall reconstructed with 900 and 4,900 patches, respectively. Thus, only a limited change in the mesh quality was found using the two different re-meshing options. All data regarding the mesh parameters, mesh resolution, generation time, mesh accuracy and mesh quality are reported in Table 4.4.

Table 4.4: An initial mesh is generated in the lumen and wall of an aortic arch and then refined with a refinement before projection and a refinement after projection. A coarse and a fine mesh of the lumen and wall of an abdominal aortic aneurysm are also generated. The parameters determine the resolution of the final mesh, according to the equations reported in Table 4.2. All meshes reproduce the original surface with sub-micrometric accuracy and have high quality elements for computational analysis.

	Aortic arch			AAA	
	Coarse	Refined after projection	Refined before projection	Coarse	Fine
Topological parameters					
Nrb	20	20	20	16	16
Nxb	6	6	6	0	0
Ndv	4	4	4	1	1
Projection parameters					
Pbe	3	3	7	5	5
CFD parameters					
Pbl	1	4	4	4	4
Pil	1	5	3	1	3
FEA parameters					
Prw	1	3	3	3	3
Psw	1	1	1	1	1
Piw	1	5	3	1	3
Projection accuracy					
N of projected patches in the real domain	684	684	3724	1575	1575
N of projected patches in the flow extensions	216	216	1176	0	0
Mesh resolution					
N of cells in the real lumen	1,224	409,500	587,412	8,300	224,100
N of cells in the flow extensions	378	128,250	182,574	0	0
Total N of cells in the lumen	1,602	537,750	769,986	8,300	224,100
N of cells in the wall	684	256,500	301,644	4,725	127,575
Mesh evaluation					
Time to mesh	4 h	132 s	180 s	0.5 h	92 s
Surface accuracy (μm)	< 0.1	< 1	< 0.1	< 1	< 1
Mean Qeas in the lumen	0.32	0.195 max 0.759	0.188 max 0.763	0.30	0.19
Mean SJ in the wall	0.81	0.90 min 0.27	0.90 min 0.21	0.86	0.89

4.4   Discussion

In this chapter the challenge of generating a structured hexahedral mesh for the image-based computational analysis of (generally) complex vascular territories is addressed. In order to simplify the mesh generation, a bottom-up procedure is developed (i.e. the Treemesh). From the vessel centerlines and centerlines' attributes (synthetic description of the vessel as a networks of tubes), a series of blocks is constructed, assigning a structure to the patient-specific vasculature. This multi-block grid, tailored on the vessel topology, is fitted inside the vessel volume, at a distance from the lumen surface. Then, a series of layers is projected from the surface of the grid on the lumen surface, and, if needed, radiated outside the lumen to model the vessel wall.

In Chapter 3, we have solved the problem of structured meshing in a patient-specific carotid artery bifurcation using a combination of surface slicing, spline reconstruction and mapping [52, 108]. Other authors have developed alternative methods effective in case of one single bifurcation or nearly-planar multiple bifurcations [61, 62, 87–89, 104]. However, when the vascular districts appear non-planar, with centerlines evolving out of one single plane, the vessel twisting (twist angle, rotation of the centerline's normal around the centerline's tangent) needs to be taken into account for the generation of a structured mesh. In the above mentioned nearly-planar cases, the twist angle was assumed to be zero by viewing the bifurcation along the bifurcation axis [115].

In the Treemesh, the design of internal and external block-structures with respect to the vessel is guided by synthetic descriptors (centerlines, equipped with normals and radii), generating specific connecting patterns at the branching locations. The surface of the block-structures is then radiated on the lumen surface, filling the entire volume with a structured grid. The projection operation along the surface normals is commonly used in mesh generation algorithms but is not suitable in regions with marked curvature, where negative-Jacobian elements (i.e. negative signed volumes) are produced. To overcome this limitation, each projecting ray is not oriented along the surface outward normal, but directed from a source point to a target point (the source points are the surface nodes of the inner block-structures and the target points are the surface nodes of the outer block-structures). As a result, well-shaped elements are generated not only in the nearly-straight branches, but also in the regions of branching (e.g. in the aortic arch) and marked curvature (e.g. in the abdominal aortic aneurysm). Remarkably, the centerlines are not necessary for the block-structures (the user can construct the blocks from the start), but allow a quick construction of initial blocks, which can then be fine-tuned to

define the final structures, facilitating and speeding up the mesh generation process.

The new approach allows recreating the vessel wall (difficult to image, especially in branching regions) with a constant thickness or, more realistically, using the local vessel size as a surrogate of wall thickness to take into account the distal tapering (thicker wall in larger vessels, which are located more proximally). The source-to-target radiation operation avoids the risk of generating negative-Jacobian elements and ensures that the hexahedrons inherit the orientation of the original block-structures. The local orientation (longitudinal, circumferential and radial directions) allows defining the material anisotropy, such as systems of counter-rotating helices of collagen fibers with layer-specific pitch angles [50]. Lumen and wall meshes are conformal (no hanging nodes and perfect edge/faces matching) and, if needed, can be coupled (same surface mesh at the interface) to enable a one-to-one correspondence between the structural and flow data for FSI applications.

Hexahedral meshes have been generated in a human aortic arch and an abdominal aortic aneurysm, requiring hours for the generation of the initial mesh and minutes for successive refinements. In both cases, the mesh reproduced the original surface with sub-micrometric accuracy and had a high shape quality, independent of the mesh resolution. Using the Treemesh, the maximal mesh-to-surface distance was found to be two orders of magnitudes lower as compared to the mesh generated using the Bifmesh, described in Chapter 3. As an extreme case, if all CFD and FEA parameters are equal to one, all surface nodes are generated by projection, reducing the accuracy-distance to zero. The projection operation in the Treemesh offers higher geometrical accuracy compared to the spline reconstruction after slicing in the Bifmesh. Instead of refining after projection, a finer mesh could also be obtained by refining the block-structures before projection, thus increasing the number of projection rays. We tested the two re-meshing options on the aortic arch but we did not find a significant difference neither in the surface accuracy nor in the mesh quality. This can be ascribed to the fact that the surface representation obtained with the coarse mesh was already adequate. In general, checking the accuracy of the surface representation and the quality of the volume mesh *a posteriori* is recommended before starting a computational analysis. However, in case of a coarse STL model, attention needs to be paid when the resolution of the new mesh reaches the resolution of the original surface model, as the discretization can introduce spurious geometrical edges which, in turn, can generate artifacts in the computational analysis (e.g. stress concentration in FEA and disturbed flow in CFD). Improving the original STL model by repeating the segmentation or by using a smoothing/refining algorithm may help avoiding such effects.

To the authors' knowledge, this is the first successful attempt to generate lumen and wall structured meshes in large image-based vascular districts. General-purpose hexahedral mesh generators have been developed (e.g. spatial twist continuum [116]) but applications to vascular districts are rare mainly because of the strong requirements needed in the vessel structured meshing (e.g. for the lumen, stretched elements in longitudinal direction and closely-layered elements in radial direction to reproduce the expected velocity gradient; for the wall, closely-layered elements in radial direction and triad axes specification in each element to define the material anisotropy). Additional applications of the Treemesh and the implementation of a strategy for a local conformal refinement can be found in Chapter 5.

Chapter 5

Real case applications of the Bifmesh and the Treemesh

CHAPTERS 3 and 4 dealt with methodological advances in structured mesh generation for image-based analysis. After demonstrating the feasibility of structured meshing in complex vascular region, a considerable effort has been dedicated to interface the method with the user, in order to increase the ease of use and provide sufficient versatility with respect to the common cases of interest. This Chapter reports a selection of cardiovascular applications divided according to the physics of the model (CFD, FEA and FSI). For each case, emphasis is given to the objective of the investigation and to the application of the mesh whereas methodological details, other than the mesh generation, and results are omitted, providing the reader with a reference where the application has been published.

One major advantage of using structured meshes with respect to unstructured meshes is the reduction of the computational costs (run time and memory). However, large models and demanding simulations (e.g. FSI) still require long computations and clusters with a high number of cores. To further reduce the computational costs, the mesh can be coarsened outside the regions of interest, reducing the degrees of freedom of the model. The last part of the chapter proposes a strategy for hexahedral conformal refinement for image-based arterial applications.

5.1 Structured mesh generation for CFD applications

5.1.1 Image-based modelling of the hemodynamics in the mouse abdominal aorta

The pathogenesis and history of aortic aneurysm formation is not fully understood. Despite the known systemic risk factors (age, gender, smoking, hypertension, genes), abdominal aortic aneurysms (AAAs) only develop at specific locations, suggesting a possible role of the local hemodynamics in their initiation and development [6, 30, 117–120]. A retrospective investigation of the aortic hemodynamics using image-based CFD may shed light on its role in AAA formation. However, human baseline data are rare because the AAA remains asymptomatic for decades[1].

5.1.1.1 Methods

To bypass the limitation of the AAA investigation in humans, a mouse model has been used. An ApoE knockout mouse continuously infused with angiotensin II by means of an implanted osmotic pump tends to develop an AAA within days or weeks, enabling a longitudinal investigation of the aneurysm formation [121–124]. Image-based analysis of the aortic hemodynamics in the mouse aorta is feasible using contrast-enhanced micro-CT scans to acquire the luminal surface (flow domain) and high-frequency ultrasounds to capture the time-dependent waveforms at the boundaries of the cropped flow domain (boundary conditions) [125]. An angiotensin osmotic pump was implanted in ten mice and mouse-specific data were recorded at baseline (before implantation of the pump, day 0) and at end-stage (after implantation, day 31). Based on the end-stage data, an AAA (either in an early or advanced stage) was found in the abdominal aorta of five out of the ten mice. The aortic hemodynamics at baseline was assessed in the mice with an aneurysm, in order to disclose a link between the local hemodynamics and the aneurysm formation.

The contrast-enhanced micro-CT images were semi-automatically segmented in Mimics to generate a triangulated surface model of the abdominal aorta and its four major branches (celiac, mesenteric, left and right renal

---

[1] The content of this section was published in the journal, Annals of Biomedical Engineering:
An Integrated Framework to Quantitatively Link Mouse-Specific Hemodynamics to Aneurysm Formation in Angiotensin II-infused ApoE -/- mice
B. Trachet, M. Renard, G. De Santis, S. Staelens, J. De Backer, L. Antiga, B. Loeys, and P. Segers
39, 9:2430-2444, 2011

arteries). Using the tool Treemesh, presented in Chapter 4, a conformal structured full-hexahedral mesh was generated in the five baseline abdominal aortas. The geometrical complexity of the abdominal aorta of a mouse resides in the branching of the four side vessels, which originate at different circumferential positions with respect to the aortic centerline, and develop in 3D, complicating the topological reconstruction of the vasculature for the mesh generation. Additionally, in two cases (AAA1 and AAA2), the right renal and the mesenteric artery originated at the same longitudinal position, requiring to model a trifurcation.

5.1.1.2   Mesh generation results

The flexibility of the Treemesh and the use of centerlines facilitated the mesh generation within a time frame of about 3-5 hours. After a mesh-sensitivity analysis, a mesh cardinality of about half-million nodes was found adequate to solve the flow. Remarkably, this resolution is sufficient to solve the flow in a mouse aorta, where the Reynolds number is around 40. In a human aorta, a finer mesh is required because the Reynolds number is about 200 [126, 127], as shown in section 5.1.2. The quality of the computational cells was optimal, with an equiangle skew of 0.16-0.22 on average and below 0.72-0.89 in all mice. A visual representation of the computational meshes is provided in Figs. 5.1 5.2 5.3 5.4 5.5 and a quantitative characterization is reported in Table 5.1.

Table 5.1: In five of the ten original mice an aneurysm was found in an early or advanced stage. After a mesh sensitivity analysis, a mesh of half million nodes and cells was judged adequate to solve the flow. As a comparison, a tetrahedral mesh would require $3, 5$ million cells to provide the same number of nodes, as shown in Chapter 1. N = number.

Mesh	N nodes	N cells	Equiangle skew (mean, max)
AAA1	494,381	470,592	0.16, 0.72
AAA2	519,460	498,375	0.22, 0.89
AAA4	395,084	374,272	0.22, 0.89
AAA6	361,981	346,000	0.19, 0.87
AAA10	416,740	399,375	0.19, 0.83
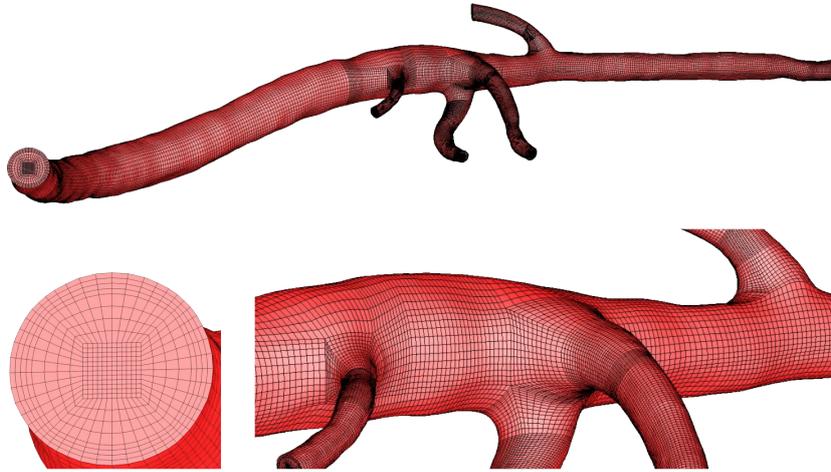
AAA1

Figure 5.1: The abdominal aorta of the first mouse at day 0 includes a trifurcation (aorta, right renal and mesenteric arteries) and two bifurcations and is successfully meshed using the Treemesh. The full aortic domain, a cross-section and the branching region are shown. The mesh of 470,592 cells is a high-quality mesh in term of equiangle skew (average 0.16, maximum 0.72).
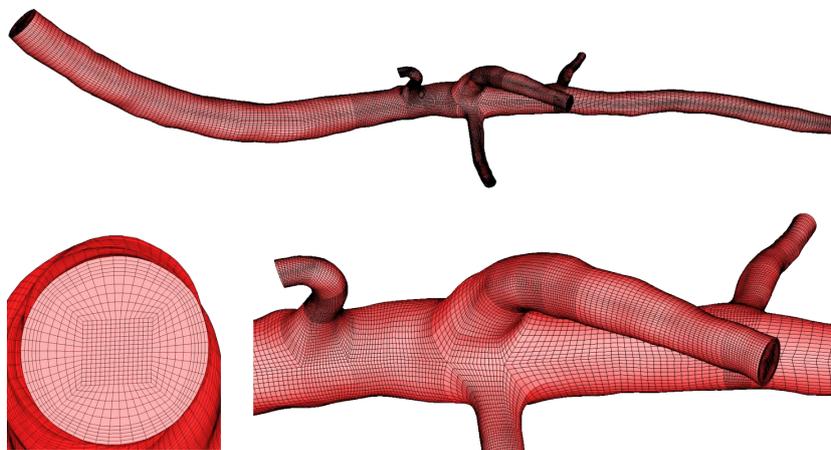
AAA2

Figure 5.2: The abdominal aorta of the second mouse at day 0 includes a trifurcation and two bifurcations and is successfully meshed using the Treemesh. The full aortic domain, a cross-section and the region around the trifurcation are shown.

AAA4
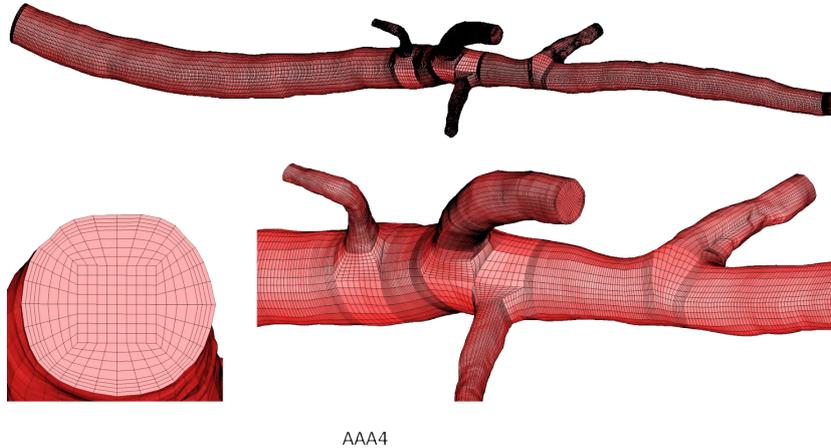
Figure 5.3: The abdominal aorta of the fourth mouse at day 0 does not include trifurcations, but four bifurcations. The right renal and mesenteric arteries are close to each other in longitudinal direction, but form a twist angle of about 90° along the aortic centerline.

AAA6
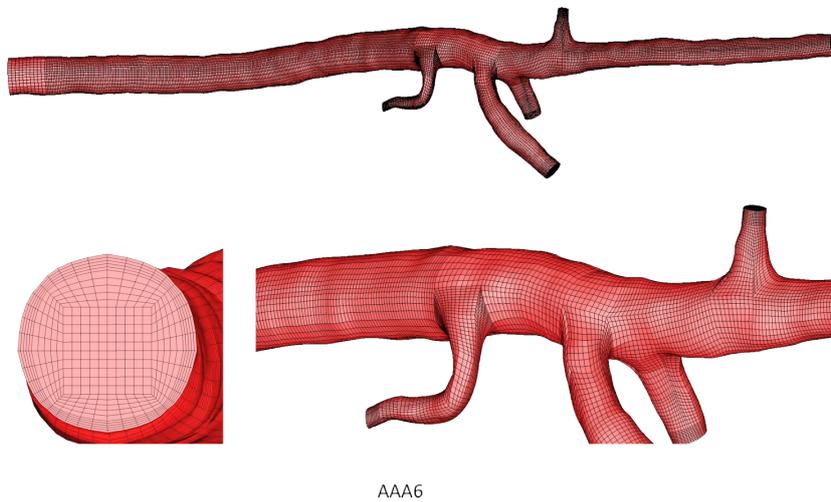
Figure 5.4: The abdominal aorta of the sixth mouse at day 0 does not include trifurcations, but four bifurcations. The right renal and mesenteric arteries are close to each other in longitudinal direction, but form a twist angle of about 60° along the aortic centerline.

AAA10
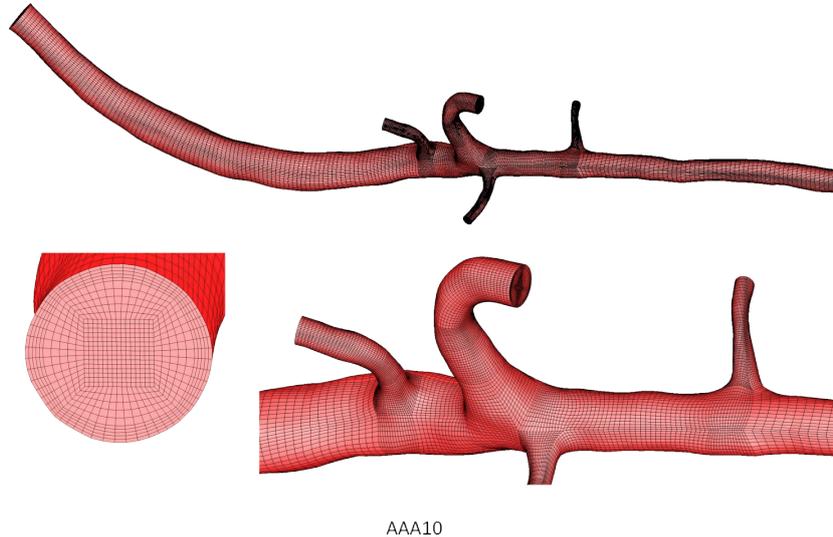
Figure 5.5: The abdominal aorta of the tenth mouse at day 0 does not include trifurcations, but four bifurcations. The right renal and mesenteric arteries are close to each other in longitudinal direction, but form a twist angle of about 120° along the aortic centerline.

5.1.2   Image-based modelling of the hemodynamics in the human aortic arch

It has been widely recognized that flow-induced shear stress is one of the most important hemodynamic factors in the localization of atherogenesis and that the disturbed flow pattern in branching points and sharp curvatures represents the preferential location of atherosclerotic lesions [6, 24, 33]. The aorta is the major blood vessel of complex geometry with such characteristics as branching, twisting, tapering and non-planar curvature. Therefore, accurate assessment of the WSS in the aorta is of paramount importance in order to get further insight into the comprehension of the role played by the WSS in vascular diseases.

In the last decade it has been demonstrated that the coupling of medical imaging and computational fluid dynamics (CFD) allows calculating highly resolved (both in space and time) 4D blood flow patterns in anatomically realistic models of the thoracic aorta, thus obtaining the distributions of the WSS at the luminal surface [41–43, 128, 129]. However, the increasing reliance on CFD for hemodynamic simulations requires a close look at the assumptions that are at the basis of the computational hemodynamics. In particular, much effort has been spent in the past to assess the sensitivity to the assumptions regarding the boundary conditions

(BCs) [36, 45, 130–136]. In order to consider the interaction between the computational domain and the upstream/downstream vasculature, coupling strategies between the computational domain and simpler models have been applied [44, 45, 130, 133, 137–139]. As an example, a multi-scale model of blood flow in a stented carotid artery is described in Chapter 6. However, the identification of the parameters of subject specific simplified vascular models involves both the pressure and flow rate measurements [140] and is based on assumptions on the velocity and pressure profiles in order to make the through-scale coupling consistent [139], thus limiting the reliability of the resulting CFD model with respect to more realistic BCs settings based on measured hemodynamic quantities. In this context, it is clear that the direct imposition of individually-measured hemodynamic quantities (such as the spatial velocity profiles or flow rate waveforms) as BCs in patient-specific simulations should be preferred [134], allowing to overcome the limitations of the coupling strategy when applied to subject-specific studies.

This study analyzes the influence of different strategies of applying PC-MRI measured flow rates as BCs on two subject-specific hemodynamic models of the human thoracic aorta with supra-aortic vessels. For each aortic model, having one inlet section (at the ascending aorta) and multiple outlet sections (at the descending aorta and at three supra-aortic vessels), a total of six flow simulations were carried out applying six different schemes for treating BCs at outlets, as reported in Table 5.2. Time-averaged (mean) blood flow rate distribution at the multiple outlets of the aortic district and three common WSS-based indicators of abnormal flow were considered and the sensitivity of these indicators to the outlet treatment strategy was evaluated. The final aim was to describe the impact that the different choices that can be done when personalized PC-MRI-based BCs are imposed have (1) on the computed flow rates and (2) on the distribution of the WSS-based descriptors[2].

5.1.2.1 Methods

Two ostensibly healthy geometries of the human thoracic aorta (Fig. 5.7 left and center) were reconstructed from 4D Phase Contrast MRI (PC-MRI) images acquired using a 1.5 T scanner (Achieva [92]) and segmented using

---

[2] The content of this section was published in the journal, Annals of Biomedical Engineering:
On the use of in vivo measured flow rates as boundary conditions for image-based hemodynamic models of abnormal flow
D. Gallo, G. De Santis, F. Negri, D. Tresoldi, R. Ponzini, D. Massai, M. Deriu, P. Segers, B. Verhegghe, G. Rizzo, and U. Morbiducci
in press (available online)

VMTK into triangulated surface models.

The finite volume method, which requires a discretization of the domain of interest, was used to solve the governing equations of the unsteady blood flow in the aorta (CFD code Fluent [74]). To solve the velocity field and the continuity equation the discretization of the flow equations on the computational grid was performed by applying a second-order upwind scheme. A linear interpolation was applied for the pressure term, using the SIMPLE pressure-velocity coupling. The unsteady flow was calculated with a time-step size of 0.001 s. From the ECG recordings during PC-MRI acquisitions, the cardiac frequency of the subject was 54 bpm, requiring 1111 time steps per simulated cardiac cycle. Simulations were run for four cycles to damp initial transients and the nodal values of the WSS vectors from the fourth cycle were used for post-processing. Blood was modeled as an incompressible, homogeneous and Newtonian viscous fluid, with density equal to 1060 kg/m^3 and viscosity equal to 0.0035 $mPa \cdot s$. For the sake of simplicity, the arterial wall was assumed rigid and the boundary conditions at the inlet and outlet sections (reported in Table 5.2) were set according to PC-MRI data (Fig. 5.6).

Table 5.2: There is no unique way to apply a set of measured flow and pressures as boundary conditions for the CFD model. In this study, the measured flow rate is applied at the inlet but six different combinations of outflow conditions are applied at the four outlets: stress free (SF), constant outflow ratio (COR) and measured flow rate (MFR). At least one stress free outlet is present in each scheme, in order to satisfy the mass conservation. Brachiocephalic artery (BCA), left common carotid artery (LCCA), left subclavian artery (LSA) and descending aorta (DAo) are indicated in Fig. 5.7.

Outlet Treatment Schemes	DAo	BCA	LCCA	LSA
S1	SF	COR	COR	COR
S2	MFR	SF	SF	SF
S3	SF	SF	SF	SF
S4	MFR	COR	COR	SF
S5	MFR	MFR	SF	SF
S6	SF	MFR	MFR	MFR

To perform the numerical simulation a computational mesh was constructed using the Treemesh facility [141]. The choice of using structured mesh-grids was motivated by the higher performance and accuracy at lower mesh cardinality with respect to the more commonly used unstructured mesh-grids, as described in Chapter 2 [73]. Using the Treemesh implementation, different resolution meshes, from 10000 to 1700000 grid cells, could be generated

on an aortic model (Fig. 5.6 and Fig. 5.7 center) to test the sensitivity of the hemodynamic parameters to the mesh resolution in realistic pulsatile conditions.
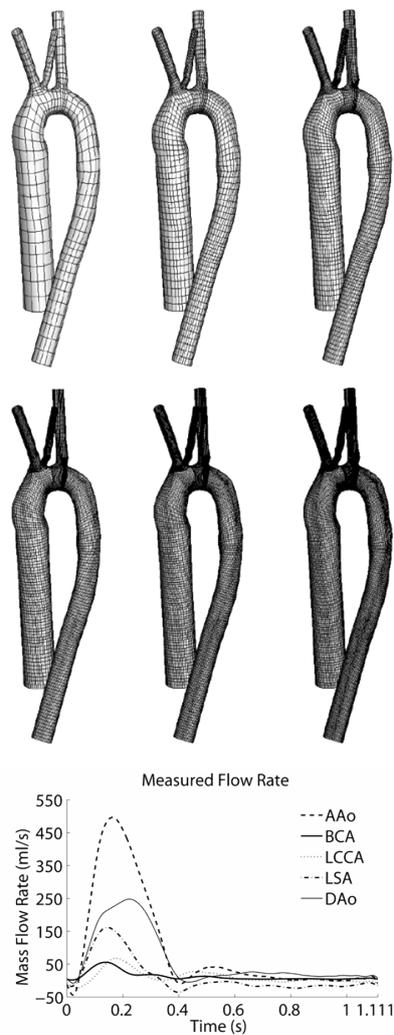
Figure 5.6: (Top) Six structured hexahedral meshes with increasingly smaller cells of the aortic arch with flow extensions ($10, 65, 200, 500, 1000, 1700$ thousand cells). All meshes are generated recycling the same set of topological parameters (the same blocks), as described in Chapter 4. (Bottom) The flow waveforms calculated from PC-MRI at the inlet and outlets (ascending aorta (AAo), brachiocephalic artery (BCA), left common carotid artery (LCCA), left subclavian artery (LSA) and descending aorta (DAo)).

5.1.2.2   Mesh generation results

The fluid domain was divided into about 1 million cells in both geometrical models. The quality of the computational cells was optimal, with equiangle skew of 0.15-0.18 on average and below 0.77-0.80. Instead of using the Treemesh for the mesh generation in an aorta, the Bifmesh could also be used, as shown on a third aortic arch. As anticipated in Chapter 3, the Bifmesh can be applied to vessels with multiple bifurcations if all branches are nearly-planar as in the aortic arch. On the other hand, the Bifmesh would not succeed to mesh highly non-planar vessels like the mouse aorta (in the previous section). A visual representation of the computational meshes is reported in Fig. 5.7 and Fig. 5.8, and a quantitative characterization is reported in Table 5.3.
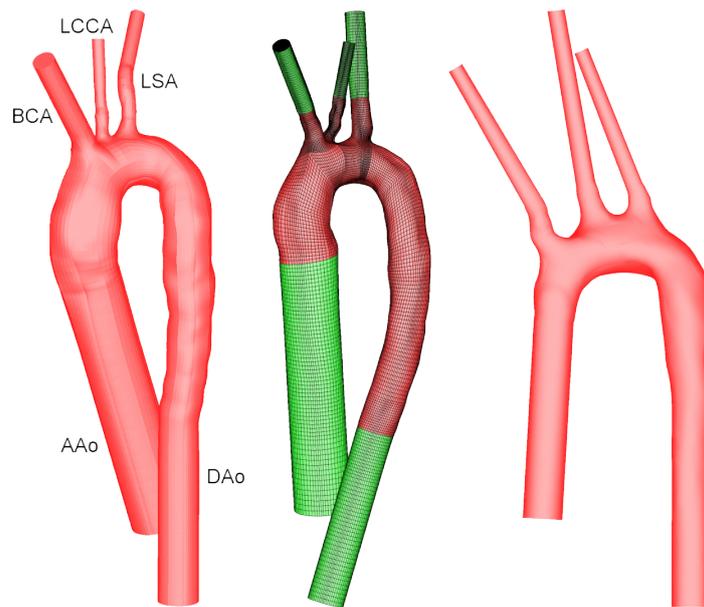
Figure 5.7: Three aortic arches reconstructed from PC-MRI images. The two models meshed with the Treemesh (left and center) and the model meshed with the Bifmesh (right) are displayed. In the center, the mesh of the second model (the model used for the mesh sensitivity analysis with the resolution reported in Fig. 5.6) is shown, with $1,041,976$ nodes and $1,022,625$ cells. In this model, the real domain (in red) has a volume of $139,881.78$ mm^3 and contains $569,250$ cells with edge length of 0.80 mm on average.

Table 5.3: All meshes, generated either with the Bifmesh or the Treemesh, have high quality elements in terms of equiangle skew, and are suitable for CFD analysis. N = number.

Mesh	Mesher	N nodes	N cells	Equiangle skew (mean, max)
Arch 1	Treemesh	1,033,429	997,056	0.15, 0.80
Arch 2	Treemesh	1,041,976	1,022,625	0.18, 0.77
Arch 3	Bifmesh	1,859,557	1,804,032	0.15, 0.80
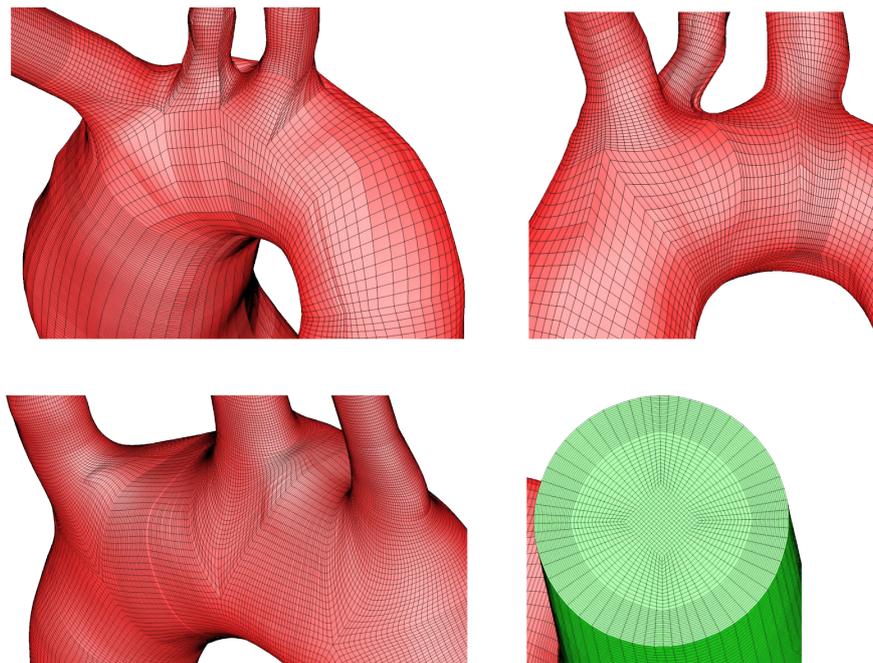
Figure 5.8: (Top) In the two models of aorta meshed with the Treemesh the blocks used for the mesh construction are visible on the surface mesh. (Bottom) The model of aorta meshed with the Bifmesh does not exhibit blocks, but sweeping domains (Y-shaped connections between three branches at each bifurcation). In green, a typical cross-sectional mesh, which can be generated either with the Bifmesh or the Treemesh, is displayed.

5.1.3 Parametric design and mesh of a graft model for hemodialysis

Constructing an arterio-venous graft is one of the choices for long-term vascular access in patients on hemodialysis as renal replacement therapy. This alternative to an arterio-venous fistula (direct connection between an artery and a vein), mostly used in patients with low quality vessels, has, however, a high complication rate. Thrombosis, due to an underlying stenosis, accounts for 80% of the graft failure [142]. This stenosis mostly occurs at the venous anastomosis or in the draining vein and is related to intimal hyperplasia. The hemodynamic phenomenon of flow disturbance is known as an inducing factor [143], which can be linked to low WSS, high oscillatory shear stress [144] or helicity of the bulk flow [145].

The SwirlGraft [146] claims to reduce formation of intimal hyperplasia by adding a swirl to the conventional straight graft. In this study, this statement is evaluated in a full CFD model, including artery, loop graft and vein[3].

5.1.3.1 Methods

A full scale model of an artery and a vein, connected with a conventional straight graft (CG) or a SwirlGraft (SG) in a loop configuration, was considered. An artery with a 4 mm diameter and a vein with a 6 mm diameter, both 115 mm proximal and 45 mm distal length, were connected with a graft with a 45° anastomosis angle. The graft had a diameter of 6 mm and a length of 300 mm. In order to investigate whether a swirling design would increase the helicity content of the flow and in turn improve the hemodynamic situation at the venous anastomosis (Fig. 5.9), the model of the graft was designed with a parametric swirl pattern, using pyFormex [75]. Keeping the swirling amplitude equal to half the graft diameter, four cases of swirling were considered using a pitch (i.e. longitudinal length of the graft required to complete one period) equal to infinite (non-swiriling case), 105 mm, 70 mm (SwirlGraft) and 35 mm, as shown in Fig. 5.10. The mesh was generated using a sweeping approach in the graft and using the Bifmesh tool for the arterial and vein anastomosis. After a robust mesh-sensitivity analysis of the WSS parameters in the region of interest (i.e. the vein anastomosis), four million nodes and cells were judged sufficient to ensure the

---

[3] The content of this section will be part of an article:
   Full CFD investigation of a swirl design of a graft for hemodyalisis.
   K. Van Canneyt, G. De Santis, S. Eloot, P. Segers, and P. Verdonck
   in preparation

mesh independence of the WSS parameters in the region of interest (i.e. the vein anastomosis).
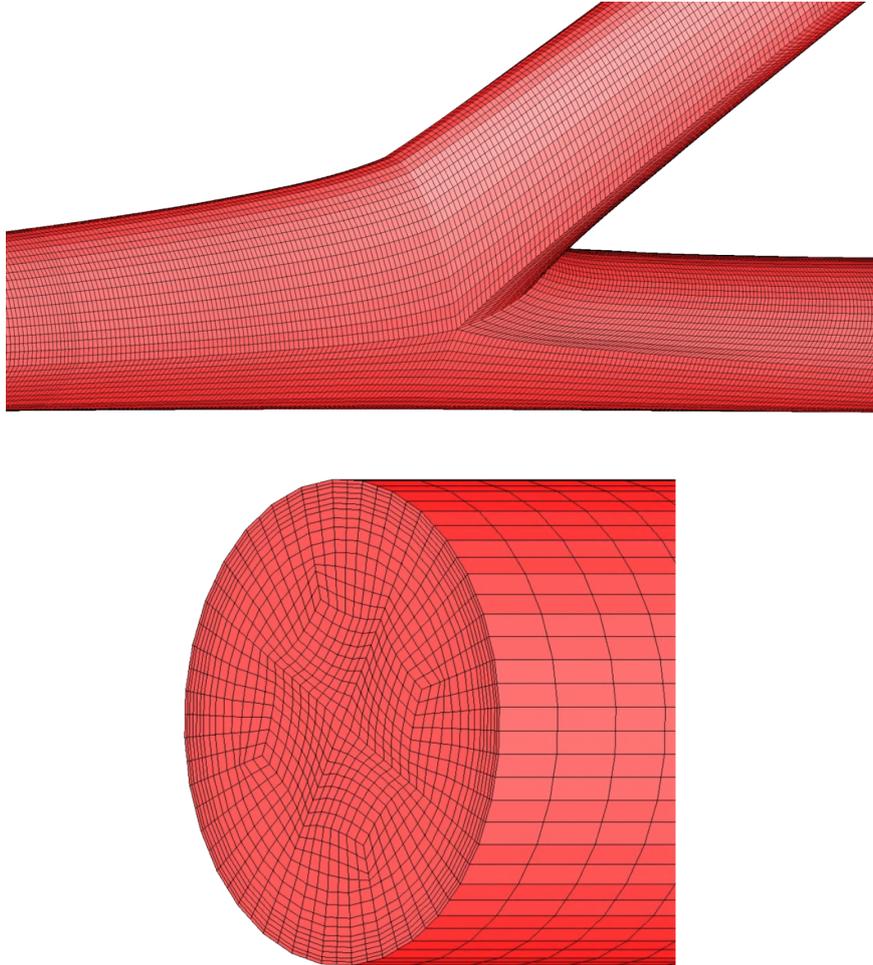
Figure 5.9: (Top) In the vein anastomosis the graft is connected to the draining vein with an angle of $45°$. The two portions of the vein and the graft represent a bifurcation and are connected with a Y-pattern built using the Bifmesh. (Bottom) The cross-section used for the mesh generation shows a very fine mesh near the wall, to capture the high near-wall velocity gradient.

5.1.3.2   Mesh generation results

A very fine mesh of about 4 million nodes was generated for the model of a graft connecting an artery to a vein in four swirling configurations.

Despite the swirling and the bending of the graft and the 45° angle at the anastomosis, the quality of the mesh was optimal, with an equiangle skew of 0.17 on average and 0.82 in the most distorted element (Table 5.4). As such the meshes were suitable for a CFD investigation. Details of the mesh can be visualized in Fig. 5.9.
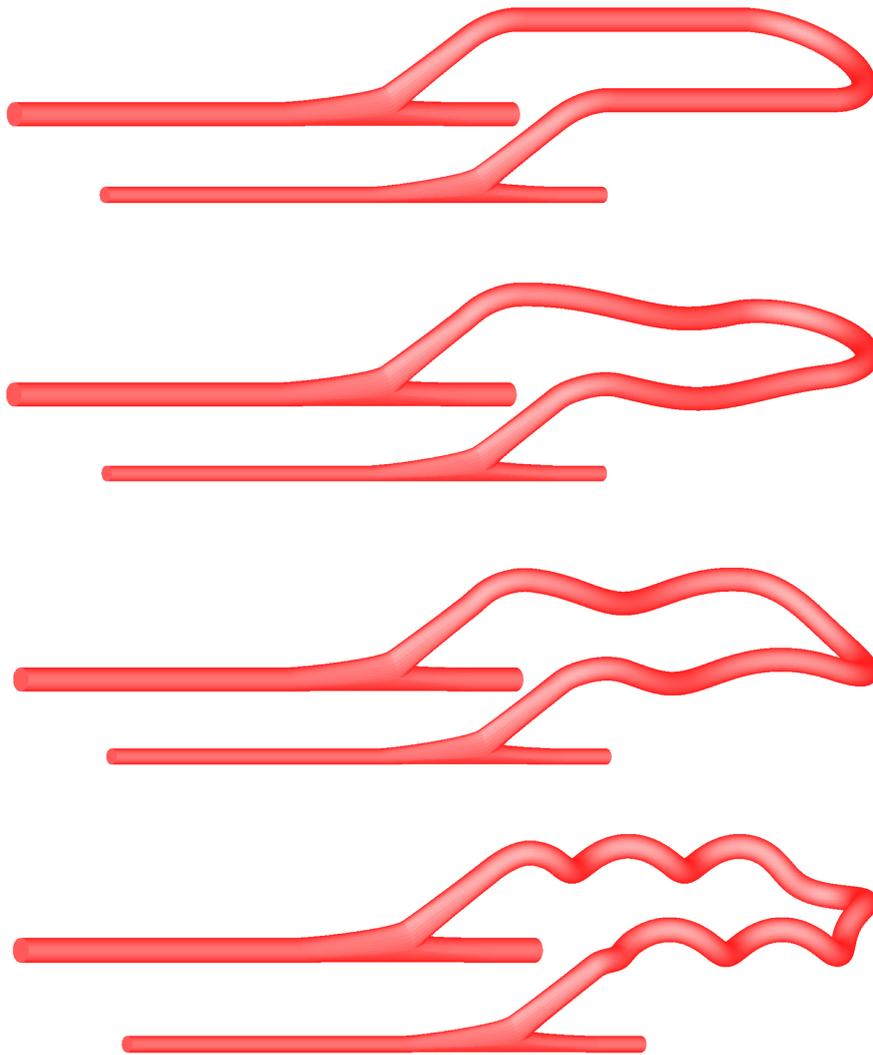
Figure 5.10: From top to bottom, four different designs of the graft: a conventional straight graft (i.e. a swirl graft with an infinite pitch), a low-swirling graft with a pitch of 105 mm, a medium-swirling graft with a pitch of 70 mm (i.e. the SwirlGraft) and a high-swirling graft with a pitch of 35 mm.

Table 5.4: To generate a mesh with 4 million nodes, 4 million hexahedral cells are required. This nodal resolution corresponds to a mesh of about 26 million tetrahedral cells. The equiangle skew is low on average, with a peak of 0.82 in the anastomosis. N = number.

Mesh	N nodes	N cells	Equiangle skew (mean, max)
Straight	3,426,975	3,329,280	0.18,0.80
Pitch = 105	4,500,585	4,372,992	0.17, 0.80
Pitch = 70 (SwirlGraft)	4,495,845	4,368,384	0.17, 0.80
Pitch = 35	4,363,125	4,239,360	0.17, 0.82

5.2 Structured mesh generation for FEA applications

5.2.1 Simulation of patient-specific carotid artery stenting

Twenty percent of all the ischemic strokes and transient ischemic attacks are caused by a narrowing of the bifurcation neck of the carotid artery [147, 148]. While carotid endarterectomy is considered the gold standard treatment for a severe carotid artery stenosis [149], carotid artery stenting (CAS) is emerging as a safe and cost-effective minimally-invasive alternative [150–152]. The clinical outcomes of CAS strongly depend on the operator ability and on the proper selection of the stent device for a specific lesion [153, 154]. An objective criterion to select the appropriate device could standardize the intervention, eventually increasing the success rate[4].

---

[4] The content of this section was published in the journal, Medical Engineering & Physics:
Carotid artery stenting simulation: from patient-specific images to finite element analysis
F. Auricchio, M. Conti, M. De Beule, G. De Santis, and B. Verhegghe
33, 3:281-289
and in the Journal of Endovascular Therapy:
Impact of carotid stent cell design on vessel scaffolding: a case study comparing experimental investigation and numerical simulations
M. Conti, D. Van Loo, F. Auricchio, M. De Beule, G. De Santis, B. Verhegghe, S. Pirrelli, and A. Odero
18, 3:397-406

5.2.1.1   Methods

In the present study, we develop a virtual framework to simulate the implantation of a specific stent device in a specific carotid artery lesion using FEA. From the in silico replica of the real intervention quantitative data regarding the post-implantation stent-vessel geometry and vessel stresses, which are known to be predictive of the long term outcomes of the CAS, are extracted.

A virtual stenting requires generating both the stent design and the patient-specific vessel. A microCT scanner, available at Ghent University [155], has been used to image three stents in detail. After segmenting the images, the stent models, resembling three commercially available designs (laser-cut open-cell, laser-cut closed-cell, braided closed-cell), have been reproduced in pyFormex. Image segmentation has been used to reconstruct the vessel lumen from a DICOM image of a computed tomography angiography (CTA). Afterwards, the Bifmesh method, described in detail in Chapter 3, has been applied to mesh the arterial wall [108]. The outer vessel surface was not clearly visible in the image and was reconstructed using anatomical data [156]. Technically, in the region classified as healthy by visual examination the thickness of the wall was set to 30% of the local vessel radius whereas in the region classified as stenotic the outer wall surface was generated by proximal-to-distal interpolation. Following this approach, a greater wall thickness was attributed to the outer edge of the internal carotid artery in the vicinity of the bifurcation, as shown in Fig. 5.11.
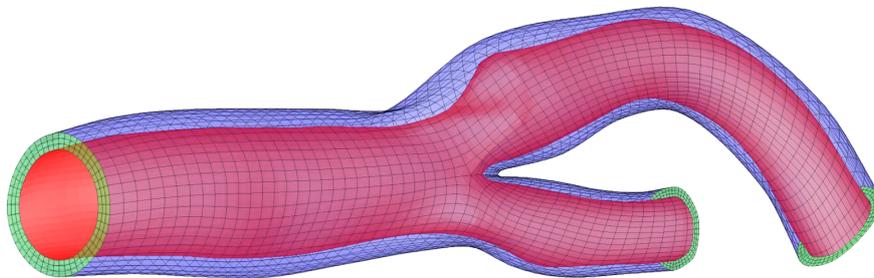
Figure 5.11: From the lumen surface of a carotid artery bifurcation (in red), the outer wall surface is artificially reconstructed (in blue) and the vessel wall is meshed using a structured hexahedral mesh (gridlines), with three layers of elements through the wall thickness (in green). On the outer edge of the internal carotid artery, a mild stenosis is modeled with a thicker wall.

5.2.1.2   Mesh generation results

After a mesh sensitivity analysis, the mesh selected for the simulation of the CAS contained 12,960 hexahedral cells and 17,564 nodes with three layers

of elements through the wall thickness. The scaled Jacobian of the computational elements was 0.84 on average with a minimum of 0.13, indicating that the shape quality of the elements was adequate for the computation. The highest element distortion appeared in the bifurcation apex, where a high curvature surface connected the internal and the external carotid arteries. In Chapter 6 the same carotid artery model will be used for a CFD investigation of the hemodynamics in a stented carotid artery.

5.2.2 Virtual and experimental modelling of coronary stenting

In section 5.2.1, we dealt with virtual CAS based on an in vivo vessel geometry and realistic stent models. However, the discrepancy between the physical case and its virtual replica should be carefully evaluated. Vessel segmentation, stent reconstruction, constitutive model, material and contact parameters are, among others, sources of uncertainty and may potentially corrupt the predictive power of the computational framework. In this investigation, an experimental case of stent deployment is modeled in order to provide an objective validation and quantify the accuracy of the finite element replica of vessel stenting[5].

5.2.2.1 Methods

A silicon mock bifurcation reproducing a stenosed coronary artery was built and a commercially available stent model was inserted. Using a microCT scanner, the inner and outer surfaces of the mock vessel were extracted as triangulated surface models. From these surfaces, the arterial wall was reconstructed using the Treemesh facility.

5.2.2.2 Mesh generation results

The inner and outer surfaces were needed in order to reproduce the coronary stenosis located in the main branch, opposite to the side branch. Both surfaces are shown in Fig. 5.12 and a detail of the mesh in the bifurcation region is displayed in Fig. 5.13. The structured mesh was generated using 67,797 elements and 91,040 nodes. The shape of all elements was optimal for FEA, with a scaled Jacobian of 0.94 on average and 0.40 for the most distorted element. It is interesting to notice that the ratio between the

---

[5] The content of this section was published in the journal, Interventional Cardiology:
Improved understanding of stent malapposition using virtual bench testing
P. Mortier, Krabbendam-Peters I., M. De Beule, H. M. M. Van Beusekom, B. Van Der Smissen, G. De Santis, J. M. Ligthart, B. Verhegghe, and W. J. Van Der Giessen
6, 2:106-109

number of cells and the number of nodes in a multi-layered mesh of a tube, such as the arterial wall, is lower compared to a non-tubular structure, such as the sphere described in Chapter 1.
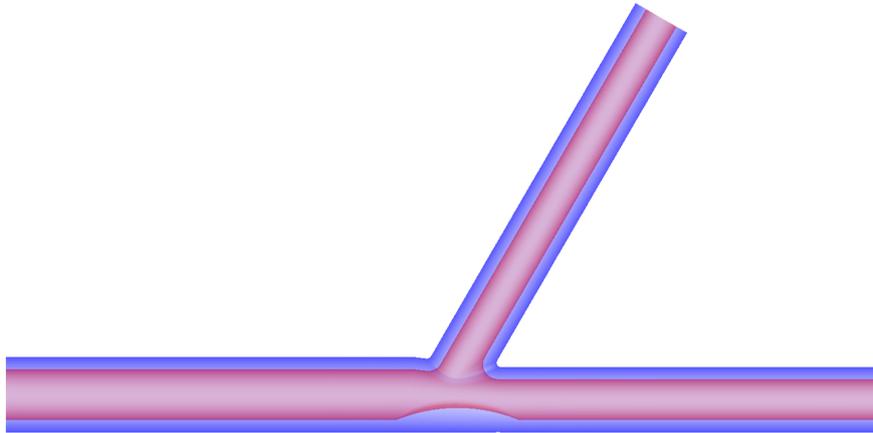
Figure 5.12: From a microCT scan of a silicone model of an 80° coronary bifurcation, the lumen (in red) and wall (in blue) surfaces are extracted. A stenosis is located in the main branch, on the opposite side of the daughter branch in the bifurcation region.
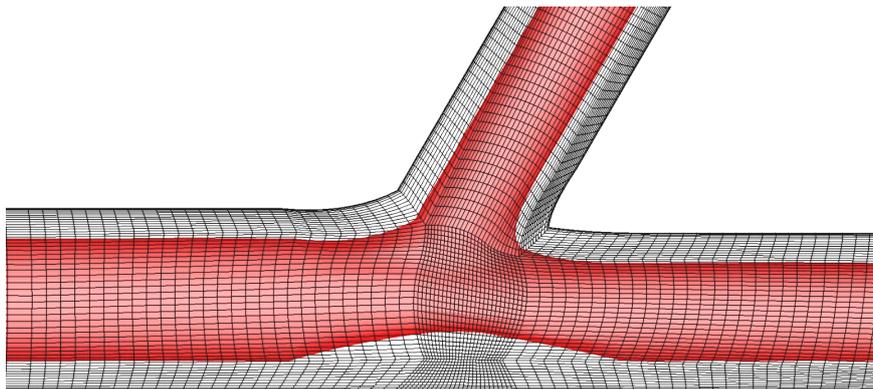
Figure 5.13: From the surface of the structured mesh generated in the coronary bifurcation model with the Treemesh facility the blocks used for the mesh construction can be recognized. Smaller high quality elements are located at the center of the bifurcation that connects the three branches.

5.2.3 Coronary stent design evaluation using a parametric vessel model

Finite element simulations can be incorporated in the design process of new devices to perform virtual prototyping and design optimization. This virtual approach can lead to a reduced time-to-market and a better performing device because it avoids the need to manufacture and test every single design iteration and provides a better understanding of the device mechanics, especially when the device dimensions are small as in the case of stents.

Coronary bifurcation lesions are generally treated following the provisional approach [157]. However, a number of challenges remains: (i) floating struts at the ostium of the side branch can complicate the access to the side branch with a guide wire and balloon catheter to perform the final kissing balloon inflation; (ii) a lower strut density improves the side-branch accessibility but negatively affects the drug delivery and tissue scaffolding; (iii) if the proximal or distal main branch diameter is used to determine the stent diameter, then the stent will be over-expanded in the bifurcation region where the vessel cross-section is much larger, leading to a lower strut density in the bifurcation region as compared to the proximal and distal segments, resulting in a suboptimal tissue scaffolding and drug delivery. This obviously leads to conflicting design requirements with respect to the side branch accessibility [158]. In order to minimize the previously mentioned limitations, the feasibility of a novel dedicated stent design and procedure for provisional stenting were investigated [159][6].

5.2.3.1 Methods

The CAD model of the novel stent was imported into pyFormex and subsequently discretized with a hexahedral mesh. To generalize the evaluation of the stent with respect to a broad anatomical scenario, a parametric bifurcation model was generated in pyFormex. The reference bifurcation model had a proximal main branch diameter of 3.5 mm, a distal main branch diameter of 2.8 mm and a side branch diameter of 2.4 mm which is in accordance with the anatomical analysis of Finet et al. [161]. The outer diameter was determined as 1.6 times the inner diameter [8]. The bifurcation angle was changed parametrically from 30 to 120° using steps of 30°. All vessel models were discretized with a structured hexahedral mesh using the Bifmesh facility (Chapter 3) [108].

---

[6] The content of this section was part of an investigation carried out as a consultancy project for Boston Scientific, reported in detail in the PhD Thesis of P. Mortier [160]

5.2.3.2   Mesh generation results

All meshes had the same mesh topology and therefore differed only because of the coordinates of the nodes, sharing the same element connectivity. The different configurations are shown in Fig. 5.14, with the side branch angle increasing from 30 to 120°. The mesh quality is the highest when the side branch is perpendicular to the main branch, the lowest when the side branch is at 30° with respect to the main branch, and intermediate with angles of 60 and 120°. Nevertheless, all meshes are optimal for FEA (Table 5.5). The branching angle influences the mesh quality because of the connection pattern between the branches, which is Y-shaped using the Bifmesh, and would ideally fit a planar bifurcation with all equally-sized branches at 120° from each other.
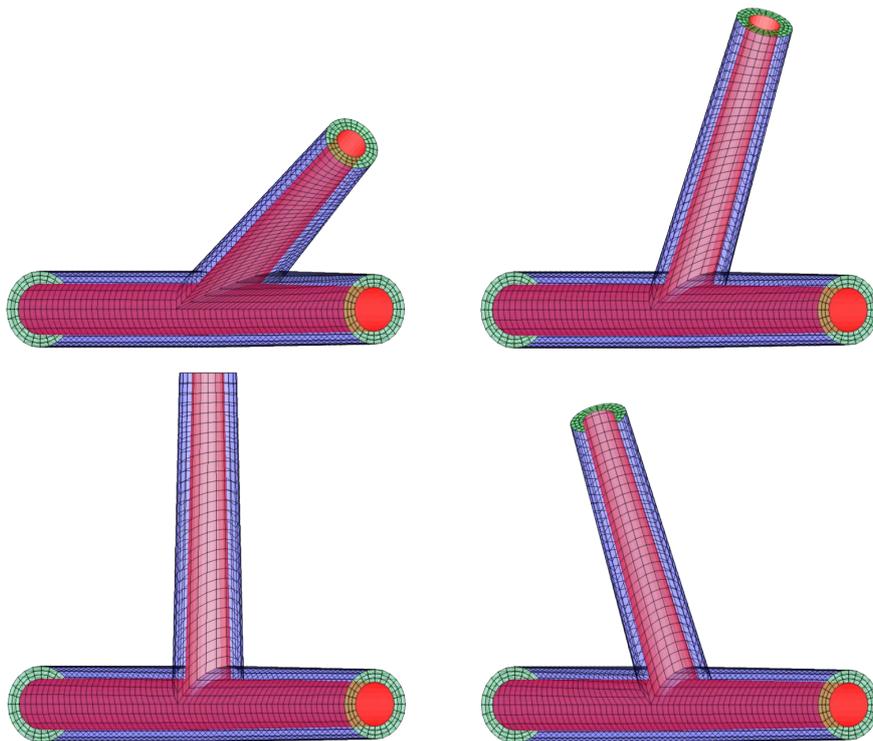
Figure 5.14: Using the Bifmesh an idealized coronary bifurcation is generated. By changing the coordinates of the nodes, and maintaining the same element connectivity, four side branch angles are modeled, allowing assessing the performance of a stent and a stenting procedure in different anatomically realistic configurations.

Table 5.5: A different angle between the main branch and the side branch produces a different mesh quality. The configurations with an angle of 60 and 120° differ because of the different vessel diameters, but show a similar mesh quality. While the 90° configuration gives the highest mesh quality, the 30° configuration gives the lowest, but the mesh is still suitable for the computation according the guidelines provided in Chapter 1. N = number.

Mesh	N nodes	N cells	Scaled Jacobian min, mean
Angle 30	8,780	6,480	0.11, 0.80
Angle 60	8,780	6,480	0.35, 0.87
Angle 90	8,780	6,480	0.60, 0.89
Angle 120	8,780	6,480	0.34, 0.87

5.3 Structured mesh generation for FSI applications

5.3.1 Assessment of the carotid artery wall motion

Ultrasound imaging (US) is a common procedure for the diagnosis of atherosclerotic lesions in the carotid artery. From a technological view, the accuracy of the US data strongly depends on the imaging algorithms. Optimization of such algorithms is often difficult, due to a lack of ground truth information, using both in vitro and in vivo testing. A virtual replica of the carotid artery mechanics can be a convenient bench test for US imaging algorithms. Swillens and colleagues have developed a full computational framework to (1) reproduce a realistic arterial flow with a moving wall and (2) test the US algorithms against the computational model, taken as a ground truth. In order to replicate the arterial flow and the wall motion, an FSI simulation is required [162]. Then, based on the flow and structural data, a simulation of the US imaging can be performed simulating the virtual US probe[7].

---

[7] The content of this section was published in the journal, IEEE Transactions on Medical Imaging:
Accuracy of carotid strain estimates from ultrasonic wall tracking: a study based on multiphysics simulations and in vivo data
A. Swillens, G. De Santis, J. Degroote, L. Lovstakken, J. Vierendeels, and P. Segers
in press (available online)

5.3.1.1 Methods

For an FSI simulation, both the lumen and wall of a carotid artery need to be reconstructed. Using patient-specific data of an 83 year old volunteer the carotid artery lumen was segmented. The vessel was cropped to the bifurcation region to reduce the computational costs and flow extensions were added to facilitate the imposition of the boundary conditions. Using the Treemesh (in section 5.2.1 the Bifmesh was used on the same geometry), the lumen and wall were meshed using hexahedral elements. The carotid artery was then embedded in a cylinder resembling the soft tissue that surrounds the carotid arteries in the neck. This extra structure had a low mechanical performance with respect to the vessel wall, but provided a stabilizing effect in the FSI simulation. To mesh the surrounding tissue an automatic tetrahedral mesh generator was used (Gambit [74]). Because of the different element types used to mesh the carotid artery and the surrounding tissue, a fully conformal interface could not be generated. Nevertheless, the nodes of the two meshes were shared at the interface. This nodal match was achieved by splitting the quadrilateral faces of the surface mesh of the carotid artery wall into triangles and forcing the tetrahedral mesh generator to respect the boundary mesh.

Table 5.6: The structured hexahedral meshes of the lumen and wall are suitable for an FSI investigation, having a low equiangle skew and a high scaled Jacobian. N = number.

Mesh	N nodes	N cells	Equiangle skew mean, max	Scaled Jacobian min, mean
Lumen	92,489	87,552	0.17, 0.66	0.28, 0.94
Wall	39,955	31,680	0.15, 0.84	0.19, 0.94

5.3.1.2 Mesh generation results

The carotid artery lumen was meshed with 87,552 cells and the wall with 31,680 cells organized in four layers to increase the mesh resolution through the wall thickness. The use of structured meshes in such applications is crucial in order to reduce the computational resources and time. As a reference, an FSI simulation of 2 cardiac cycles executed on 8 cores for the flow solver, 8 cores for the structural solver and 1 core for the coupling software (two Intel Xeon 2x Quad-core Intel Xeon processors, 2.66 GHz) required one week's time. The evalution of the mesh revealed that both the lumen and wall had high quality, both in terms of equiangle skew and scaled Jacobian. Therefore, the two meshes were adequate for an FSI simulation

using a partitioned approach. Details of the carotid artery mesh are reported in Table 5.6 and a view of the entire mesh is displayed in Fig. 5.15.
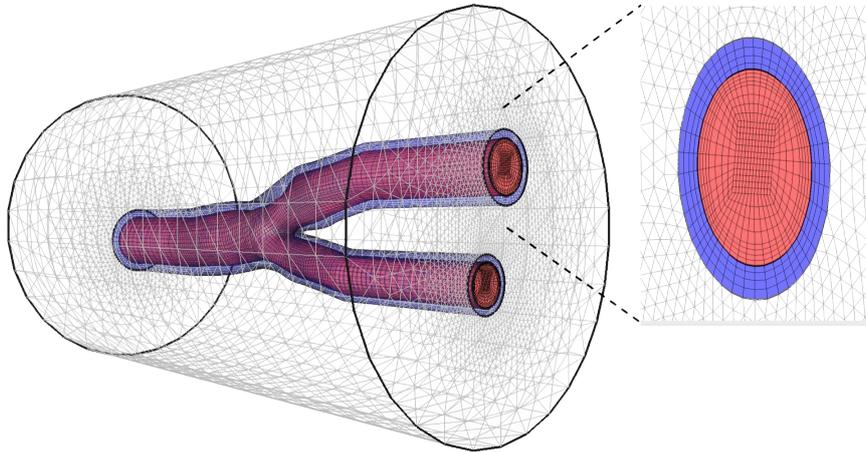
Figure 5.15: Starting from the lumen surface of a carotid artery, a structured hexahedral mesh is generated in the lumen and wall. Around the wall, the surrounding tissue is constructed as a cylinder and meshed with tetrahedrons. The nodes of the wall and the nodes of the surrounding tissue are shared at the interface, as shown in the enlarged detail.

5.4   Local refinement of a hexahedral mesh

A number of examples have shown that the use of hexahedral meshes is feasible in image-based computational investigations. To reach the same number of nodes, a linear tetrahedral mesh (with or without a prismatic boundary layer) would require several times more cells than a hexahedral mesh, as shown in Chapter 1 and Chapter 2 [73], thus increasing the CPU time and memory. Nevertheless, modeling a large domain or performing a demanding computation such as a multi-physics simulation (FSI) can restrict the applicability of the numerical analysis to one single case because of the computational time and resources required. For example, the simulations described in section 5.1.2, 5.1.3 and 5.3.1 required 1 or 2 weeks' time.

A straightforward solution to reduce the computational cost while still keeping the same accuracy of the result is to reduce the number of elements by differentiating the mesh resolution inside and outside the region of interest. This is not trivial in case of a structured mesh because the topology of the refinement needs to be defined a priori and is strongly constrained, e.g., it is not possible to create a transition from one block to two blocks (i.e., the typical case of a bifurcation) halving the cell volume. A pattern to

create a transition from one block (8 nodes, Fig. 5.16 a, d) to three blocks is available using four transitional blocks (16 nodes, Fig. 5.16 b, e). By combining this transition in two directions, a transition from one block to nine blocks is possible using 13 transitional blocks (32 nodes) (Fig. 5.16 c, f), as proposed by Tchon [163]. The lateral surface of this transition pattern has a 90° periodicity (the four lateral sides have the same face's topology, as shown in Fig. 5.16 c), enabling its use inside a tubular domain. The original 1-to-3 pattern has a 180° periodicity (the two pairs of parallel block sides have two topologically different faces, as shown in Fig. 5.16 b), and therefore, it cannot be used to mesh a tubular domain, because it would produce hanging nodes. However, the 1-to-3 pattern can be used to refine the mesh of the vessel wall. Remarkably, these transitions did not alter the local triad axes of the elements, which were inherited from the original block (hexahedrons' local axes are highlighted in Fig. 5.16 d, e, f using red, green and blue lines for the x, y and z axes).
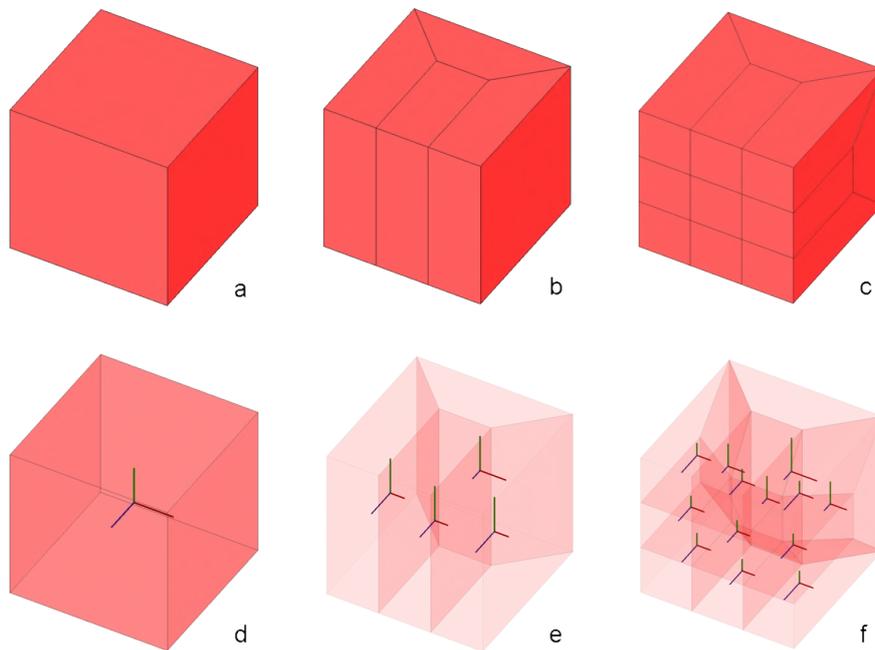
Figure 5.16: A block (a, d) can be split into smaller blocks to enable mesh size transitions. Four blocks are necessary to build a one-to-three transition (b,e) while 13 blocks are necessary to implement a one-to-nine transition (c,f). The latter may be used to topologically refine the region of interest.
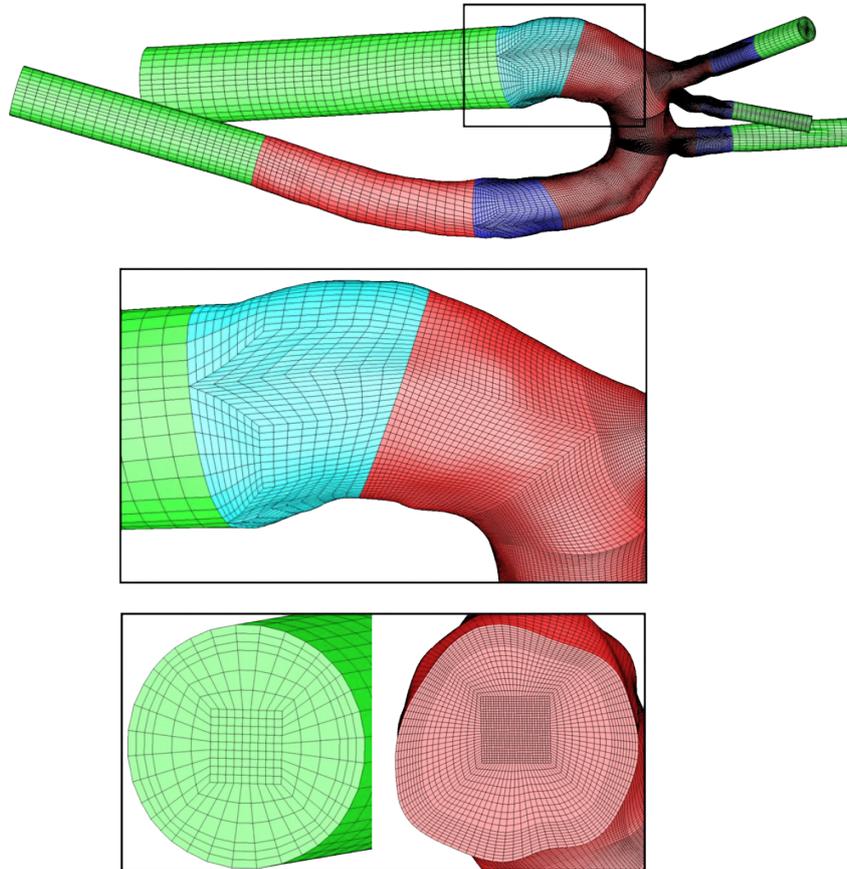
Figure 5.17: The aortic arch of section 5.1.2 is meshed using a conformal refinement produced with 1-to-9 transitional blocks. The region of interest (arch in dark red) is meshed with fine elements whereas the flow extensions (in green) and a portion of the descending aorta (in light red) are meshed with coarse elements. Light and dark blue elements indicate the 1-to-9 and 9-to-1 transition blocks, where the most distorted elements appear. In the middle and on the right, a longitudinal and a cross-sectional detail of the transition between the ascending aorta and the arch is displayed.

To prove the feasibility of conformal refinement of a structured mesh in real case, an aortic domain used in section 5.1.2 was chosen as an example. All branches other than the arch were considered to be outside the region of interest. Transitional blocks were positioned between each coarse-meshed region and the fine-meshed region: one 1-to-9 transition between the ascending aorta and the arch, three 9-to-1 transitions between the arch and the supra-aortic branches and one 9-to-1 transition between the arch and the descending aorta. The transition patterns produced a grid refinement

(three-times finer mesh) both in the circumferential and radial direction, thus increasing the cross-sectional mesh resolution by a factor nine. Such a cross-sectional refinement was combined with a three times denser mesh in the longitudinal direction, to keep the same cell size proportion, thus reducing the cell volume by a factor 27 on average (Fig. 5.17). With respect to the non-refined case, the maximal skewness increased from 0.77 to 0.91, because of the distorted cells in the transition patterns. The average skewness also increased from 0.16 to 0.27 but this should not be attributed to a general lower mesh quality, but to the localization of the finer mesh, which increased the weight of the arch (after refinement the arch contained 27 times more and more distorted elements as compared to the straight tubular branches). As a result, only few elements showed slightly high distortion and were located in the transition region whereas the elements in the refined region (region of interest) maintained the original pre-refinement quality.

By distributing the elements according to the desired local accuracy, the refinement of a hexahedral mesh has the potential to speed up highly-demanding computations (e.g. multi-physics simulations) on large arterial territories (e.g. human aorta).

Chapter 6

A computational investigation of the hemodynamics after carotid artery stenting

$\mathcal{C}$AROTID artery stenting (CAS) is a minimally-invasive intervention to treat a carotid artery stenosis. The local hemodynamics established after CAS may drive a tissue reaction which can influence the long-term success of the intervention, as anticipated in Chapter 1. To assess the local hemodynamics in a stented artery one would have to reconstruct the stented lumen from a medical image and perform an image-based computational fluid dynamics (CFD) analysis. However, this would not improve the treatment because a stent cannot be removed once implanted. Moreover, the lower resolution of the medical image as compared to the stent strut size would corrupt the geometry (and the flow) at the stent-vessel interface, which is the location where the shear forces impact the arterial endothelium and modulate a mechano-biological response from a cellular to a tissue level. Instead of evaluating the impact of CAS *a posteriori*, the post-stenting hemodynamics can be predicted from an in silico replica of the CAS intervention, starting from a medical image of the diseased vessel and the stent model.

In this Chapter, first, a patient-specific and stent-specific finite element analysis (FEA) of CAS is performed, predicting a realistic configuration of the stented vessel. Then, after a surface manipulation, the stent volume is subtracted from the vessel lumen, returning a 'negative' of the structural

domain, which represents the physical domain in which the blood would flow after stenting. Finally, the blood flow in the stented artery is simulated using a CFD analysis for the carotid artery and an impedance model for the vascular circuit from which the carotid artery is isolated. On the one hand, imposing such impedance-based boundary conditions complicates the computation, prolonging the simulation time. On the other hand, it provides a more realistic flow in the common carotid artery (CCA) and in the daughter vessels, the internal carotid artery (ICA) and the external carotid artery (ECA), as compared to imposing in vivo flow/pressure data measured in the pre-stenting configuration (the shape of the lumen can change significantly after stenting). From this in silico replica, the shear forces that would act on the carotid artery endothelium can be estimated and the local hemodynamics can be evaluated using the model of atherogenesis described in Chapter 1[1].

6.1   Introduction

Stenting is one of the options for the treatment of a carotid artery stenosis. This minimally-invasive intervention increases the vessel patency, by pushing the stenosis away from the lumen, and reduces the hydraulic resistance at the diseased location in order to restore the cerebral flow to a physiological level. Large population clinical studies have reported a limited long-term success of CAS, mainly due to thrombo-embolic events and in-stent restenosis [164–167]. Stent thrombosis may develop on the basis of in-stent restenosis, which is a consequence of prolonged inflammatory processes in the stented vessel wall with excessive myointimal proliferation [168, 169]. In turn, in-stent restenosis has been associated, among others, to blood flow disturbances established after stenting [170–172]. As such, extensive research has been devoted to (i) disclose the physical link between an adverse post-interventional biological response and the mechanical impact of a stent and to (ii) explore better design/material possibilities.

Most research focused on the performance of a stent *per se* (e.g. radial stiffness, flexibility) [173], the stent-vessel interaction from a structural perspective (e.g. vessel stress, lumen gain) [52], or the effect of a stent on the vessel flow from a fluid dynamic perspective [174]. However, investigating

---

[1] The content of this section was published in the journal, Computer Methods in Biomechanics and Biomedical Engineering:
Hemodynamics impact of stent-vessel (mal)apposition following carotid artery stenting: mind the gaps !
G. De Santis, M. Conti, B. Trachet, T. De Schryver, M. De Beule, J. Degroote, J. Vierendeels, F. Auricchio, P. Segers, P. Verdonck, and B. Verhegghe
in press (available online)

the stented-vessel hemodynamics ideally first requires a structural analysis, to obtain the post-implantation domain, followed by a fluid dynamic analysis [175] or a fluid-structure interaction analysis [168]. Recently, a geometrical algorithm to reproduce the post-stenting configuration has been proposed [176]. However, such an approach neglects the structural impact of the stent on the diseased vessel, which introduces large deformations in the vessel and imperfect stent-to-vessel apposition, due to the compliance mismatch between the stiff metal stent and the soft arterial tissue.

In this Chapter we provide a full-scale approach to integrate a FEA and a CFD analysis to predict the impact CAS on the patient-specific hemodynamics. As a first step, a stent is virtually implanted in a mildly-stenosed carotid artery using FEA (the same vessel described in Chapter 5 is used); then, the stented lumen is virtually perfused reproducing a realistic blood-flow condition using CFD. A critical step in this work is the development of a strategy to convert a finite element model of a stented artery (structural domain) into a finite volume model (flow domain) without losing geometrical details.

6.2   Materials and methods

Modeling the stented vessel hemodynamics starting from medical images of the unstented configuration requires four serial steps: image-based stent deployment, computational model conversion, vessel perfusion and separated post-processing, as described below.

6.2.1   Image-based finite element analysis of carotid artery stenting

A stent model, reconstructed from a micro-CT scan of a commercially available stent (Acculink, Abbott [177]), was virtually implanted in an image-based stenosed carotid artery using FEA, as previously described in Auricchio et al. [52] and validated against experimental data in Conti et al. [51]. Briefly, from a CT angiographic image, the vessel lumen was extracted and the wall was artificially reconstructed and meshed using the Bifmesh, as described in Chapter 5 [108]. The self-expanding Nitinol stent[2] was inserted in a cylindrical tube (i.e. the sheath). The sheath containing the stent was then shrinked, bent and positioned inside the stenosed vessel using the finite element solver Abaqus/Explicit [111], thus prestressing the stent into a

---

[2] a self-expanding stent, different from a balloon-expanding stent, deploys as a spring when released from a sheath, without the need for balloon-induced plastic deformations.

crimped and curved configuration. The sheath was then gradually released in a quasi-static process, enabling the expansion of the stent against the vessel wall, until an equilibrium configuration was reached (i.e. the post-stenting vessel-stent configuration shown in Fig. 6.1). The vessel tissue was modeled using the isotropic hyperelastic material proposed by Prendergast et al. [178], without differentiating the stenotic region from the rest of the vessel. The arterial tissue was considered unstressed in the pre-stenting configuration. Boundary conditions were applied to the nodes of the ending sections in order to allow only a radial displacement. The superelastic behavior of Nitinol was approximated using a previously described material model, implemented in Abaqus with a user material subroutine [179]. These assumptions were considered acceptable as the scope of the analysis was to obtain a realistic post-stenting shape of the vessel and stent and not to predict the stress distribution in the structures.
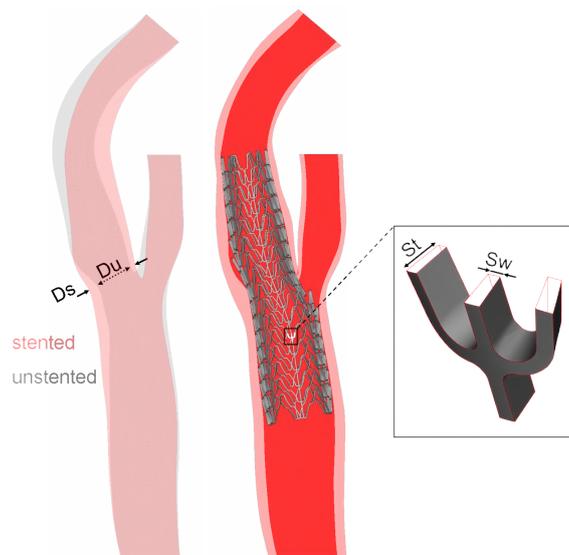
Figure 6.1: (Left) The deployment of a stent in a carotid artery deforms the shape of the vessel by increasing the vessel diameter and straightening the vessel, as shown by superimposing the transparent silhouette of the stented lumen (pink) on the unstented lumen (gray). The indicated chord measures 4.2 mm before stenting (Du) and 5.6 mm after stenting (Ds). The struts are not shown for clarity. (Centre) The open view of the arterial wall (pink), lumen surface (red) and stent struts (gray) after the CAS reveals the occurrence of an imperfect apposition of the struts on the vessel endothelium near the stenosis and the ostium of the ECA. (Right) A detail of the stent is enlarged. The dimensions used for strut thickness (St) and strut width (Sw) are 240 and 100 µm, respectively (different dimensions with respect to the commercial model were assigned to the struts).

6.2.2   Conversion of the structural domain into the flow domain

After the finite element simulation of the CAS, the meshes of the virtually deformed vessel and stent were separately exported into pyFormex to build a model suitable for a CFD analysis of the blood flow. The inner vessel surface, extracted from the arterial wall using a feature angle separation[3], and the stent surface represented the two boundaries of the blood flow domain.
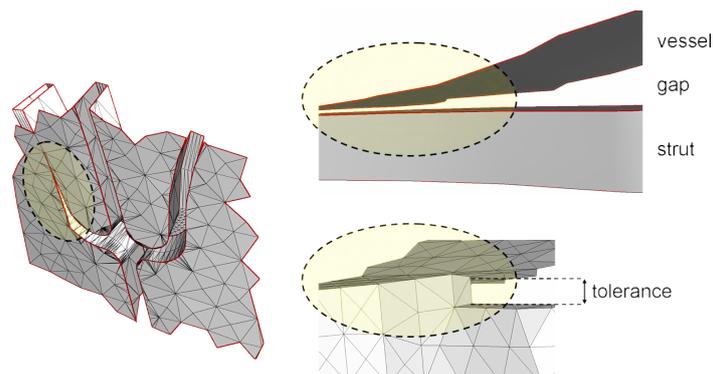
Figure 6.2: (Left) Where the stent struts are close to the vessel, the surface generated from a direct Boolean subtraction includes a smooth surface transition from a perfect contact to a gap, which results in a non-meshable volume. (Right) When a stent strut is at a non-zero distance from the vessel surface (i.e. a gap), computational cells should fill the gap. However, because of the numerical truncation, the gap should be bigger than a threshold in order to be filled with computational cells. A surface triggering allows correcting the transition from non-contact to contact (top), returning a surface suitable for the mesh generation (bottom).

---

[3] If the angle between two adjacent faces' normals is higher than the chosen feature angle, the common adjacent edge identifies a geometrical edge; closed loops of geometrical edges can be used to partition a surface.
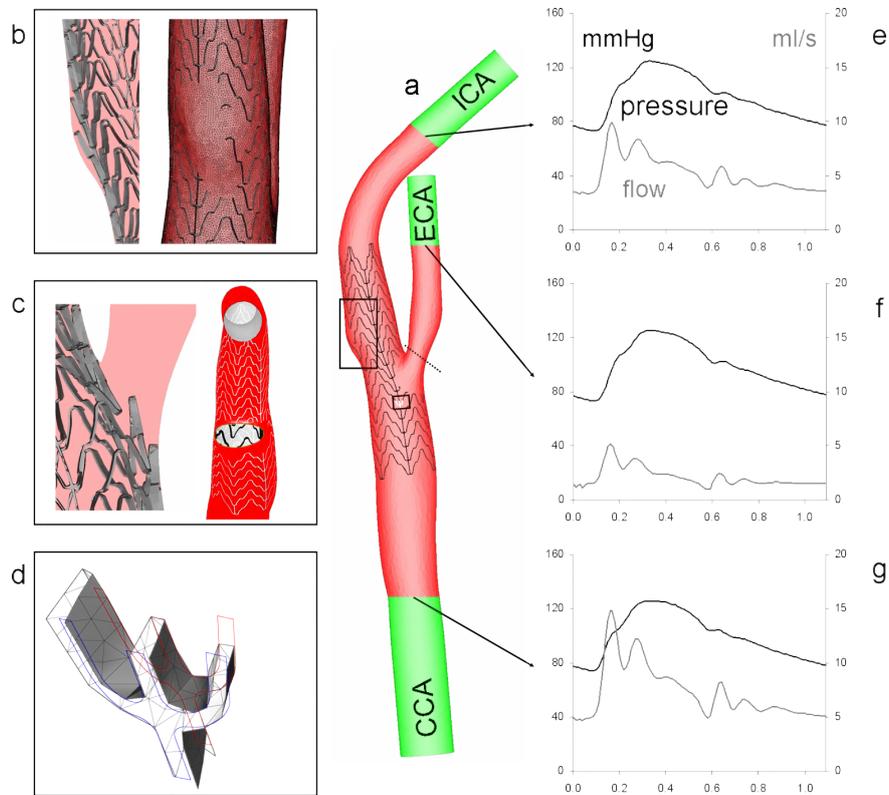
Figure 6.3: (a) The carotid artery lumen reconstructed from the FEA of CAS is defined by a wet vessel surface (in red), a wet stent surface (in gray) and flow extensions (in green). After deployment the stent does not entirely conform to the vessel surface, leaving zones of malapposition (panel b, right), fish scaling (panels b and c, left), and unapposed struts that partially occlude the orifice of the ECA (panel c, right). The stent struts are accurately reconstructed, as shown in panel d, where the gray surface represents the CFD-mesh of a strut inter-connection while the colored lines represent the contours of the corresponding FEA-mesh. In panel b a detail of the tetrahedral mesh is shown. Time-varying pressure and flow data imposed at the CCA (e), ICA (f) and ECA (g) are drawn with the time scale on the abscissa (in seconds).

The flow domain in the stented artery was extracted by a Boolean subtraction of the post-implantation stent volume from the lumen volume. In practice, this operation produces a surface that does not bind a meshable volume, with non-manifold edges, self-intersecting triangles, and finite gaps. Such spurious features are the results of (i) the numerical approximations occurring in the Boolean operation when the stent surface is close to or in contact with the vessel surface and (ii) the contact algorithm used in the

finite element solver, which generates a contact pressure when the contacting surfaces are at a non-zero distance. Such problems are common when performing Boolean operations on real shapes and can be solved by setting a tolerance or by cleaning the final surface using a smoothing algorithm. Both approaches are not advisable when dealing with stents because they require a geometrical tolerance comparable to the stent strut size, with the risk of losing the cross-sectional strut shape or even filtering out the strut. Therefore, an *ad hoc* approach, based on surface triggering, has been developed to prepare the stent surface before the Boolean subtraction. Briefly, the distance between the outer stent surface and the inner vessel surface was computed and assigned to each stent node. If the distance was found to be lower than a threshold value the node was extruded slightly outside the vessel surface. Due to this operation, the stent surface was triggered with respect to the inner vessel surface, appearing either inside or outside the lumen (modeling a gap or a contact, respectively), but never in the region within the threshold distance from the vessel surface, except at the transitions from non-contact to contact. This triggering operation was performed in two steps, an automatic extrusion in pyFormex and a manual intervention in Mimics [48], but in the future can be fully automated. A Boolean subtraction using the triggered stent surface generated a closed non-self-intersecting surface manifold, without altering the geometrical features of the stent, except for the transition zone from non-contact to contact (Fig. 6.2).

Flow extensions were added to the vessel at the inlet and the outlets in the directions of the centerlines to facilitate the application of the boundary conditions. The surface model, representing only the wet portion of the vessel wall and stent together with the flow extensions, was used to generate an unstructured tetrahedral mesh using Tetgen [107] (Fig. 6.3 a). Despite the proven advantages of using a structured hexahedral mesh over a tetrahedral mesh for the CFD analysis of the arterial flow [73], hexahedral meshing is currently not an option in a complex stented vessel because of the high number of topologically-equivalent blocks that would be needed for the volume decomposition [141].

6.2.3 Computational fluid dynamics analysis of the carotid artery perfusion using an impedance model of the surrounding vasculature

To apply the boundary conditions for the flow in the stented carotid lumen, an impedance model representing the upstream and downstream vasculature was coupled to the CFD analysis. A total pressure was applied at the inlet of the model and the pressure at the outlets was set according to the following convolution integral, previously introduced by Olufsen et al. [130]:

$$p(t) = \frac{1}{T} \int_0^T z(\tau) q(t - \tau) \, d\tau \qquad (6.1)$$

In this equation T is the RR interval of a cardiac cycle (interval from the peak of one QRS complex to the peak of the next as shown on an electrocardiogram), z is an impulse response characterizing the distal vasculature, and q is the flow exiting the fluid domain through the outlet surface at a time instant t.
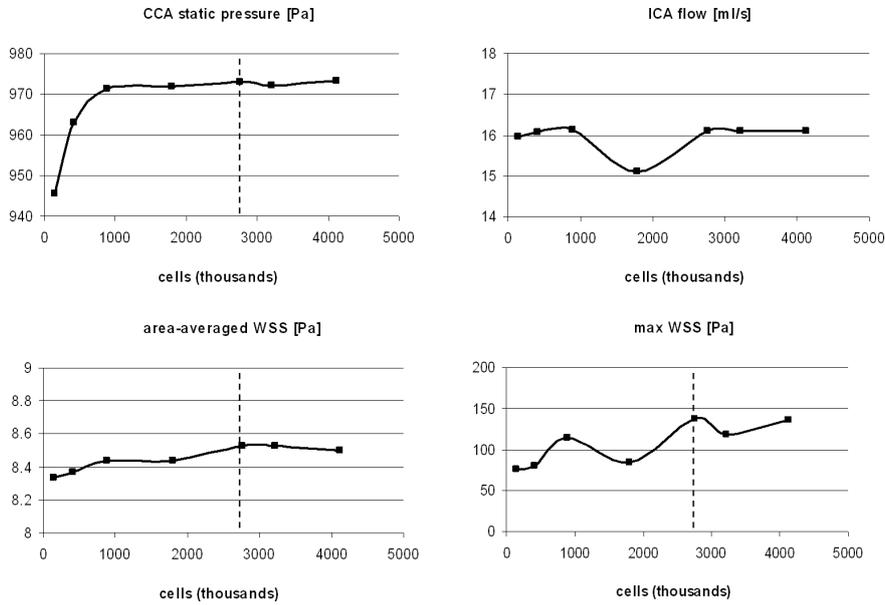
Figure 6.4: (a) From top-left to bottom-right, the area-averaged static pressure on the CCA cross-section, the flow exiting the ICA, the area-averaged WSS on stented-vessel surface and the maximum nodal WSS, obtained with different mesh resolutions ranging from 0.25 to 4.1 million tetrahedrons, are reported. A steady-state flow inlet was imposed at the inlet and zero pressure at the outlets. All values plateau in the three finer meshes, with exception of the maximum nodal WSS which oscillates. Such oscillations have been previously reported and depend on the numerical diffusion error associated to unstructured tetrahedral meshes in the considered range of the mesh resolution [73].

The impulse responses at the ICA and ECA outlets (as well as the total pressure imposed at the CCA inlet) were based on sampled pressure and flow waveforms obtained from the 1D model developed by Reymond et el. [180]. With $P_i(w)$ and $Q_i(w)$ being the Fourier transform of the pressure and flow

waveforms for each outlet i, the impedance spectrum $Z_i(w)$ was defined as:

$$Z_i(t) = \frac{P_i(w)}{Q_i(w)}, \ i = ICA, ECA \qquad (6.2)$$

The vascular impulse response $z(t)$ was then calculated by inverse Fourier transforming $Z_i(w)$, yielding an impulse response which decays to zero for t going to infinity. However, keeping in mind the periodic nature of the problem, this infinite impulse response could be condensed within one period by subsequently adding all periodic frames $t \in [kT, (k+1)T]$; $k = 1, 2, 3 \dots$ to the first T seconds of the impulse response, eventually yielding $z(t)$, the impulse response as it was used here.

The time-dependent simulation was performed using the finite volume solver Fluent 12.0 [74] for the continuity and the Navier-Stokes equations in laminar conditions, using a second-order accuracy in space and time and a double numerical precision. A no-slip condition was applied to the boundary wall and blood was treated as a Newtonian fluid (density $1,050 \ kg/m^3$ and viscosity $0.0035 \ Pa \cdot s$). To implement the impedance numerically, the equation (6.1) was discretized in time, so we write the pressure, p, at time step k as:

$$p(k) = \frac{1}{T} \sum_{j=0}^{N-1} z_j q_{k-j} \Delta t \qquad (6.3)$$

In this equation N represents the number of time steps within a period and Δt a fixed time step.

Ideally one would solve the flow field together with the boundary conditions discussed above in an implicit manner. However, since Fluent was used as a black-box solver, the boundary-condition equations could not be added implicitly and the Jacobian ($\mathbf{J}$) that links the pressure changes (Δp) at the boundaries to the flow changes (Δq) at the outlets had to be estimated at the beginning of each time-step. For the case of two outlets (indices 1 and 2) and one inlet (index 3), the Jacobian equation writes:

$$\begin{bmatrix} \Delta q_1 \\ \Delta q_2 \end{bmatrix} = \begin{bmatrix} \frac{\partial q_1}{\partial p_1} & \frac{\partial q_1}{\partial p_2} & \frac{\partial q_1}{\partial p_3} \\ \frac{\partial q_2}{\partial p_1} & \frac{\partial q_2}{\partial p_2} & \frac{\partial q_2}{\partial p_3} \end{bmatrix} \cdot \begin{bmatrix} \Delta p_1 \\ \Delta p_2 \\ \Delta p_3 \end{bmatrix} = \mathbf{J} \cdot \begin{bmatrix} \Delta p_1 \\ \Delta p_2 \\ \Delta p_3 \end{bmatrix} \qquad (6.4)$$
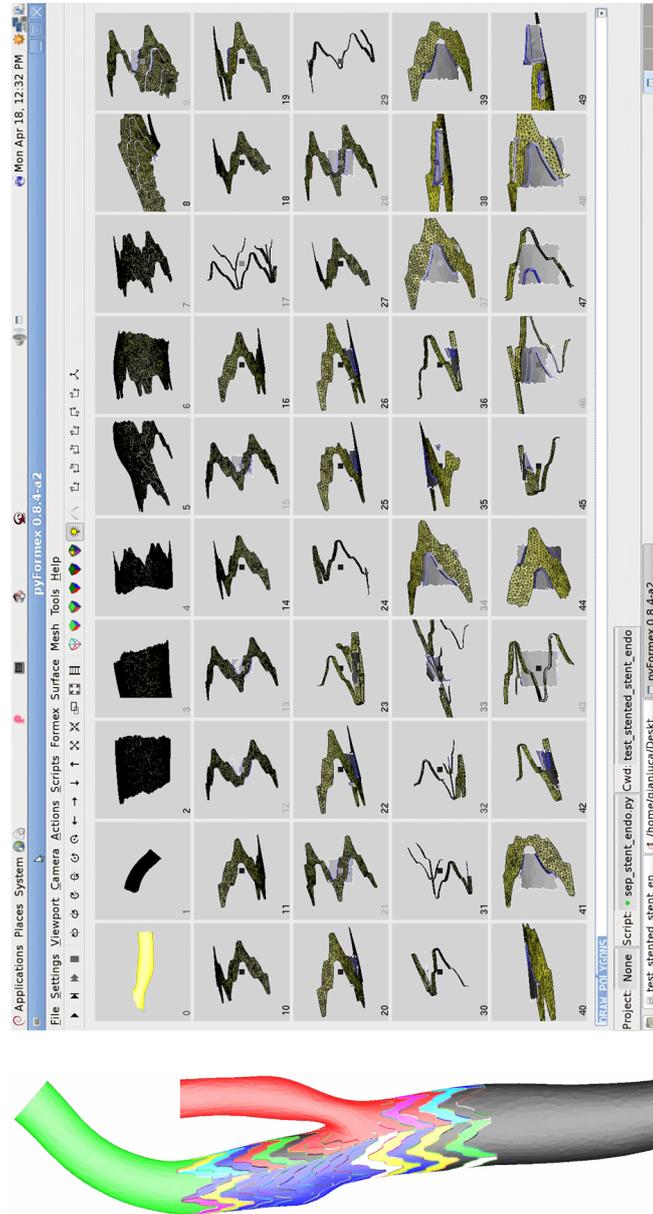
Figure 6.5: If the surface is partitioned using a single feature angle of 60° approximately 1,600 surfaces are generated (different surfaces are identified by a different color). On the pyFormex interface the largest 50 partitions (in yellow) are shown together with the surrounding surfaces (in gray) to facilitate the visual inspection and discrimination between a vessel surface, a stent surface and a mixed surface.

After perturbing the outlet pressures and calculating the resulting flow changes, the Jacobian was estimated through finite differences. Summing the elements on each row of **J** should give zero, since q does not change when the boundary pressures are perturbed uniformly. As a result, the inlet pressure did not need to be perturbed to estimate **J**. The Jacobian equation (6.4) and the BC-equations (6.3) form a closed system of linear equations that was solved for every time step. This iterative procedure required an initialization transitory which was found to disappear within the first cardiac cycle. Four cycles were simulated, using a time-step of 1 ms to ensure the periodicity of the results. On 8 CPUs of type 3.40 GHz, this required one week computational time. A mesh sensitivity analysis was performed under steady-state conditions to reduce the computational time. As the inlet flow that would establish after imposing the total pressure and impedances was not known a priori, a worst case scenario has been set by imposing an inlet flow of 23.6 ml/s (Reynolds number around $1,300$) [181] and stress-free outlets. From seven meshes, ranging from 0.25 to 4.1 million tetrahedrons, a mesh of 2.7 million tetrahedrons was chosen based on the values of the CCA static pressure, ICA flow, area-averaged wall shear stress (WSS) and maximum nodal WSS (Fig. 6.4). We verified *a posteriori* that the peak inlet flow computed using the impedance model (14.9 ml/s) was significantly smaller than the steady-state flow used for the mesh sensitivity analysis, assuring the adequacy of the chosen mesh resolution for the flow computation. The flow at the boundaries and the WSS vectors on the wet wall surface were recorded from the last cycle for post-processing.

6.2.4 Extraction of the hemodynamic parameters on the arterial wall and stent

For the analysis of the WSS the boundary surface needed to be separated into a wet stent surface and a wet vessel surface. The contact between the vessel and stent and the amount of interconnected struts make this a challenging operation. A visual application dedicated to the surface separation was developed in pyFormex, using multiple feature angles and enabling to subdivide a surface into thousands of different parts within minutes. Briefly, a surface is separated using a high feature angle into a vessel surface, a stent surface and a mixed surface (i.e. a surface containing triangles belonging to both the vessel and stent). This operation is then repeated using a smaller feature angle on the mixed surface only, until no mixed surfaces are left (Fig. 6.5). On the separated vessel and stent surfaces, time-averaged descriptors of the WSS vectors (i.e. time-averaged WSS (TAWSS), oscillating shear index (OSI) and relative residence time (RRT)) were computed according to the following equations:

$$TAWSS(\mathbf{s}) = \frac{1}{\mathsf{T}} \int_0^{\mathsf{T}} |\mathbf{WSS}(\mathbf{s}, \mathsf{t})| \, \mathrm{dt} \tag{6.5}$$

$$OSI(\mathbf{s}) = 0.5 \left(1 - \frac{\left| \int_0^{\mathsf{T}} \mathbf{WSS}(\mathbf{s}, \mathsf{t}) \, \mathrm{dt} \right|}{\int_0^{\mathsf{T}} |\mathbf{WSS}(\mathbf{s}, \mathsf{t})| \, \mathrm{dt}} \right) \tag{6.6}$$

$$RRT(\mathbf{s}) = \frac{1}{(1 - 2\,OSI)TAWSS} \tag{6.7}$$

where T is the overall interval of the cardiac cycle and $\mathbf{s}$ is the position on the vessel wall. Low TAWSS values (lower than 0.4 Pa) are known to stimulate a proatherogenic endothelial phenotype [6]. High OSI values identify regions on the vessel wall where the instantaneous WSS deviates from the main flow direction in a large fraction of the cardiac cycle, inducing a perturbed endothelial alignement [182]. RRT is a combination of OSI and TAWSS and is proportional to the residence time of a particle near the wall. Recently, Lee et al. [183] recommended RRT as a robust single metric of low and oscillating shear.

6.3   Results

6.3.1   Geometry of the stent-vessel malapposition

When converting the post-stenting finite element models of the carotid artery and stent (FEA domain) into a single manifold surface (CFD domain), all geometrical features (e.g. strut size and cross-sectional shape) were preserved, except at the locations where the stent-to-vessel distance in the FEA domain was lower than a threshold and contact between the stent and vessel was assumed. The threshold was set to 20% of the stent strut thickness in order to preserve only the major gaps, increase the minimal size of the computational cells in the gaps and reduce the operator time required for the surface manipulation. Of the total stent surface (538.7 mm^2), 15.5% (83.5 mm^2) was located on the outer side and could potentially scaffold the vessel wall but only 8.2% (44.13 mm^2) was actually in contact with the vessel wall. This difference could be attributed (i) to a region of malapposition (imperfect contact between the stent and vessel) occurring distally to the stenosis, due to a limited capability of the stent to conform to the artery

wall (contourability), and (ii) to a number of stent struts obstructing the ostium of the ECA. Moreover, a fish-scaling effect appeared in these regions, with the stent struts oriented transversally with respect to the local vessel surface (Fig. 6.3 b and c).

6.3.2   Arterial wall hemodynamics

During the simulated cardiac cycle, the flow in the CCA was not equally partitioned in the daughter vessels, but a time-dependent flow split ratio governed the perfusion of the ICA and ECA, with the ICA taking from 63.5 to 79.4% of the flow (70.1% on average) (Fig. 6.6).

flow rate ratio (% Qica/Qcca)
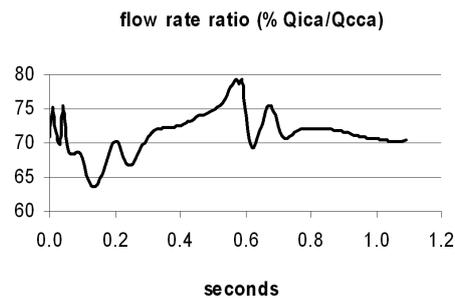
Figure 6.6: The flow rate ratio between the ICA and the CCA shows that during one cardiac cycle 70.1% of the blood flows from the CCA into the ICA.

Following the model of atherogenesis to characterize the wet vessel surface in terms of the WSS metrics (see Chapter 1), a large atherosusceptible region (TAWSS < 0.4 Pa) colocalized with a region of malapposition on the outer edge of the ICA, distally to the stenosis (Fig. 6.8). Moreover, the endothelium located on the proximal side of all the inter-strut connections (stent trifurcations) presented the same atherosusceptible pattern (Fig. 6.7). The OSI was lower than 0.15 throughout the surface, not indicating the presence of atherosusceptible regions *per se* (Fig. 6.9). The distribution of the high RRT repeated the same trend of the low TAWSS, but the pattern of the high RRT around the strut inter-connections attenuated distally (Fig. 6.9).
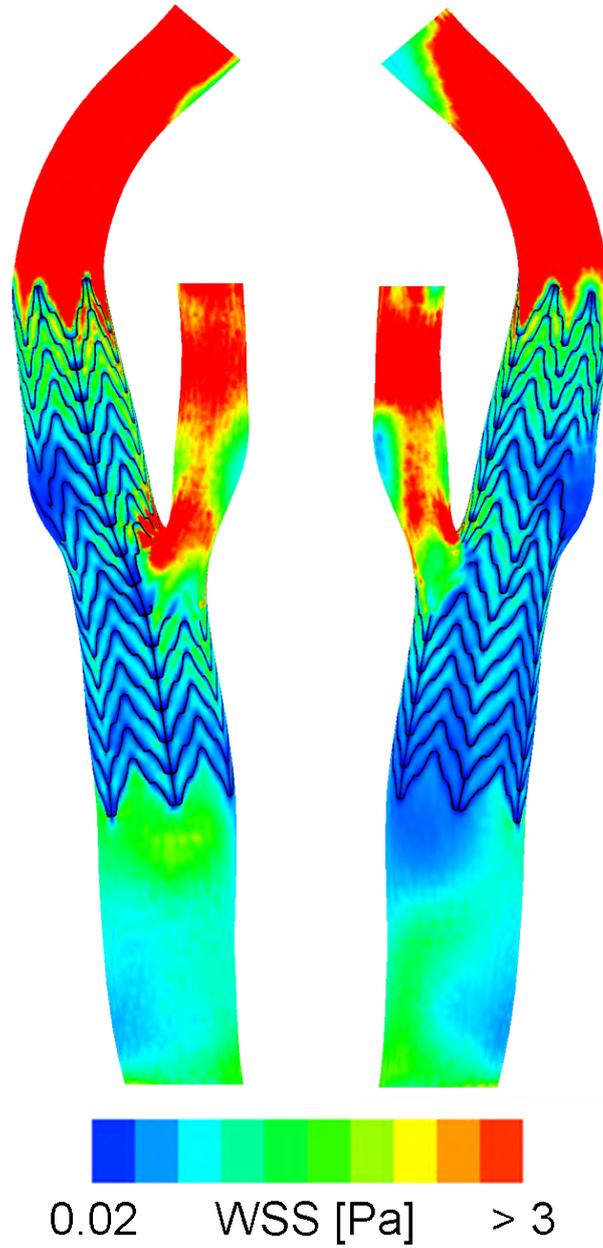
Figure 6.7: The TAWSS is shown on the anterior (left) and posterior (right) side of the carotid artery (the stent is colored in black).
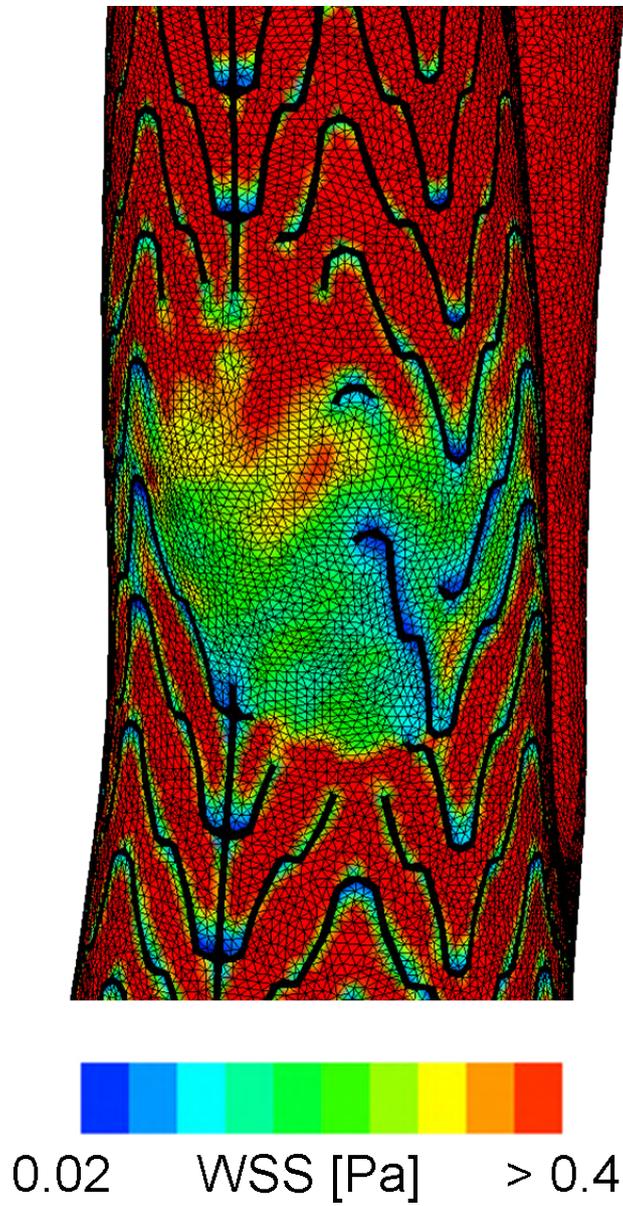
Figure 6.8: The TAWSS is shown on a malapposed region distal to the stenosis (the stent is colored in black).
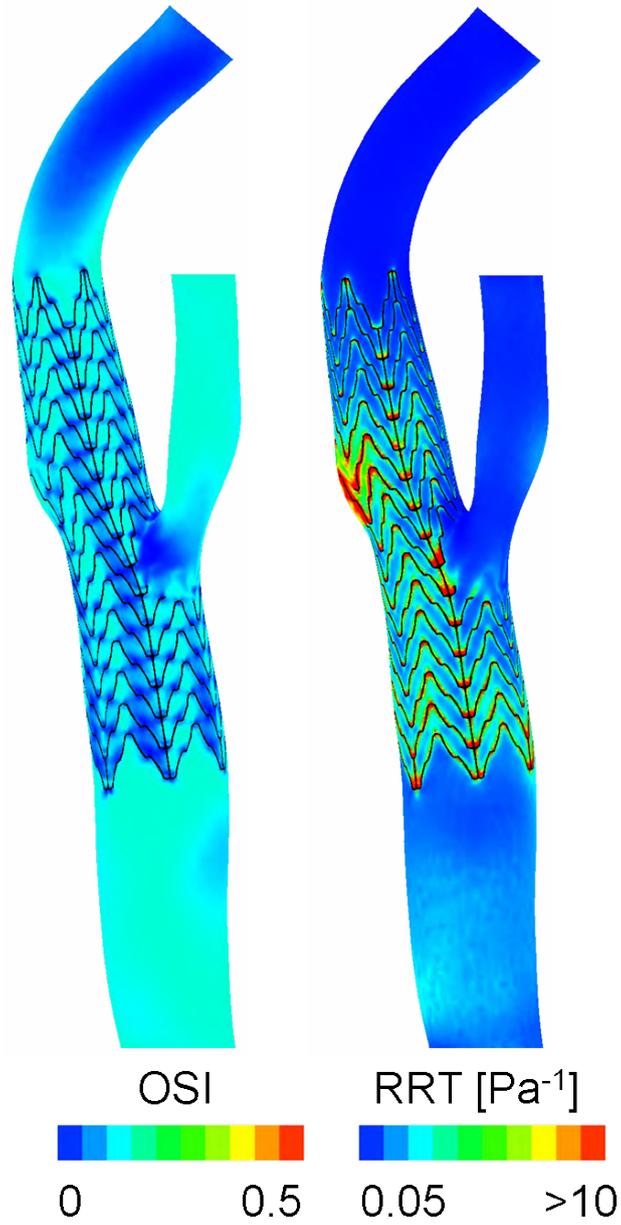
Figure 6.9: The OSI (left) and the RRT (right)are shown on the anterior side of the carotid artery (the stent is colored in black).

6.3.3 Stent hemodynamics

Two regions could be distinguished on the wet stent surface based on the analysis of the WSS. In the bifurcation the stent struts facing the ECA orifice were subjected to high TAWSS values, with instantaneous WSS vectors reaching a maximal intensity of 65 Pa during the cardiac cycle, while far from the bifurcation the stent struts experienced a TAWSS that was one order of magnitude lower (Fig. 6.10). Post-stenting geometrical features (malapposition gaps, fish scaling and struts facing the orifice) predicted from the FEA qualitatively colocalized with the altered hemodynamic features predicted from the CFD analysis.
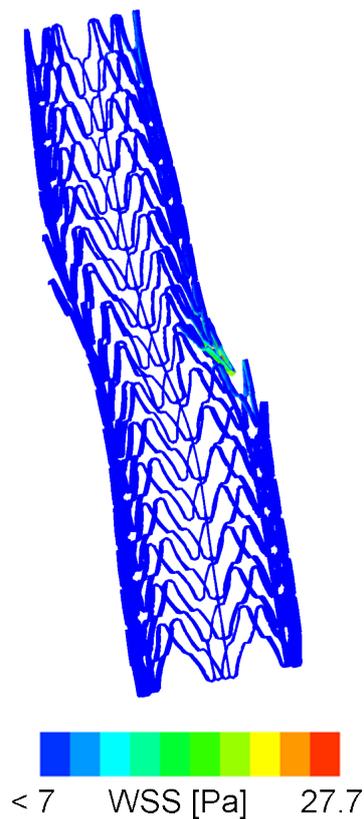
Figure 6.10: The TAWSS is plotted on the wet stent surface. The stent is visualized using the same view of Fig. 6.7 left, but the vessel surface is not shown.

6.4   Discussion

In this study the hemodynamic impact of CAS is explored using both a stent- and a patient-specific analysis. A stent is deployed in a carotid artery using FEA and both the deformed vessel and stent are taken into account for the flow computation using a CFD investigation. Low TAWSS values on the vessel surface are found in the locations of malapposition and at the distal side of the stent-strut interconnections.

While well-apposed strut interconnections directly cause lower shear forces, because the thick struts shield the distal vessel surface from the main stream, the role of malapposed struts may be overestimated. The large area of low TAWSS occurring in the regions of malapposed struts may be an effect of the stent malapposition but also of the vessel concavity that occurs in the same region, which is located distally to the stenosis (Fig. 6.3 b). The shoulder of the stenosis may shield the concave vessel region from the main stream causing a low velocity gradient. Moreover, the shoulder of the stenosis, more pronounced in the pre-stenting vessel, is also the cause of the strut malapposition because the stent is neither flexible enough to accomplish the concave vessel nor stiff enough to completely straighten up the vessel. Nevertheless, the correspondence of the locations of imperfect scaffolding, concavity and stent strut interconnections with the map of the atheroprone hemodynamics suggests that the geometrical characterization of the stented configuration may be used as a surrogate for the (more time-consuming) CFD analysis, thus significantly simplifying the assessment of the hemodynamics impact of a stent on a vessel.

The stent struts facing the ECA ostium represent an obstacle to the stream. On such struts, elevated shear forces may represent a risk for embolism. Recently, optical coherence tomography (OCT) imaging observations have suggested that struts facing the orifice may endothelialise [33]. If living cells colonialize the struts facing the ECA orifice, the abnormally high WSS may trigger thrombo-embolic events [6]. In such a case, the detached embolus could be either flown into the ECA or sucked into the ICA stream, depending on the flow features at that location and at that phase of the cardiac cycle, thereby possibly causing a stroke.

From a technical perspective, the major innovations presented in this work include (i) a strategy to convert a FEA-mesh into a CFD-mesh of a patient-specific stented artery using a triggering operation (which can be fully automated) and (ii) a tool to divide the wet-stent from the wet-vessel by visual examination for separated post-processing. With such improvements, a number of simplifications assumed in previous works no longer seem to be required. Virtual geometrical stenting (geometrical stent expansion in

a rigid vessel) has been proposed to replace the FEA of stenting [176]. However, it may introduce an error in the hemodynamic parameters because it approximates the post-stenting vessel using the unstented vessel and it considers the stent as a geometrical entity only. Two stents with the same design but different stiffness would result in the same vessel-stent configuration after virtual geometrical stenting and, in turn, in the same hemodynamic effect. Moreover, this approach does not allow to consider and quantify (also clinically) important stent-related aspects such as the lumen gain, vessel straightening, stent malapposition, fish scaling effect and asymmetric stent strut deployment which all occur in reality and can be captured by performing a structural analysis before solving the flow [51].

The geometrical complexity of a patient-specific analysis has motivated the use of simplified vessel geometries, such as an idealized vessel model (straight or curved cylinder), non-bifurcating vessels, non-stenosed (healthy) vessels which do not need stenting, or simplified stent designs, with a reduced stent size (to limit the computational domain, which requires a very fine mesh around the stent struts) and a non-realistic cross-section of the struts [53,174,175,184–186]. For the first time, the flow in a patient-specific stented bifurcating vessel has been imposed using an impedance model, following the recent contributions of Williams et al., who applied it to an idealized stented coronary artery bifurcation [187], and Morbiducci et al., who considered a patient-specific unstented carotid artery [45]. Prescribing a generic flow waveform as an inlet boundary condition and/or a fixed flow ratio as an outlet boundary condition (BC) would not suit the goal of this study since the hydraulic resistance of a stented carotid bifurcation may be different from the unstented case, and this effect would be lost when the flow waveforms measured before stenting would be imposed (flow conditions could not be measured because the CAS was not yet performed on the patient). Therefore, a total pressure was prescribed at the CCA inlet, and the vasculature distal to each outlet was modeled as a time-invariant linear dynamic system, completely determined by its impedance spectrum, represented as a vascular impulse response. The pressure and flow waveforms that were used to generate the boundary conditions were taken from a 1D model [180], which has been validated against in vivo data and yields generic but realistic pressure waveforms throughout the vascular tree. It is, however, important to note that the waveforms extracted from the 1D model (upon which we based our boundary conditions) characterize a normal, healthy carotid and not the specific subject. By following this approach, we assume that (i) the total pressure at the CCA is insensitive to the presence of the stent downstream and (ii) the impedance of the downstream vasculature is insensitive to the presence of the stent upstream.

The present methodology represents a valid solution to perform a CFD calculation based on the post-stenting configuration, in turn based on a

finite element replica of the CAS starting from images of the unstented vessel and stent, and can be expanded to other vessel/stent interventions such as a balloon-expandable stent for coronary stenting [50], implantation of a self-expanding flow diverter in a cerebral aneurysms [53] and implantation of a stented graft in an abdominal aortic aneurysm [168, 188, 189]. This full scale approach accurately reproduces the geometry and flow after CAS and could be used for clinical training or, after an *a posteriori* validation, for CAS planning. In this study the vessel wall reconstructed from medical images was considered unstressed in the pre-stenting configuration whereas, in reality, an initial stress is already present because of the blood pressure. The stress state in the pre-stenting wall can be computed from the known blood pressure using the backward incremental method [190] and applied before the stent deployment. Nevertheless, when the vessel deformation is not significant and a high geometrical accuracy is not required, the FEA can be replaced by a purely geometrical approach, thus reducing the computational effort to the CFD model only [186].

Chapter 7

Conclusion

THE primary objective of this research was to generate computational structured meshes in vascular domains reconstructed from medical images. This mission has been accomplished with the implementation of a novel framework, either in a simplified (the Bifmesh) or in a general (the Treemesh) version. As such, the new mesh generation method is the main result of this work. The initial applications of the framework to the test cases reported in Chapters 2-4 have proven the feasibility of structured mesh generation in a patient-specific blood vessel. The early contributions of this framework aside from its development, in the fields of computational fluid dynamics (CFD), finite element analysis (FEA) and fluid-structure interaction (FSI), reported in Chapter 5, have highlighted its robustness, flexibility, ease of use and potential to become a 'standard procedure' in mesh generation for image-based vascular analysis. However, more challenging geometries would still require the use of unstructured meshes, such as in case of a stented artery, as reported in Chapter 6.

7.1 Original contributions

In Chapter 2, Bezier splines have been used to represent the surface of a left coronary artery, reconstructed from a biplane angiography and modeled as a sequence of circular sections. These splines served as a guide for the mapping of a structured mesh in the arterial lumen by means of an isoparametric transformation. This procedure enabled to generate high-quality hexahedral meshes in a vascular tree with tubular vessels and multiple bifurcations. With respect to sweeping algorithms that generated similar meshes and were already applied to the image-based analysis of a straight vessel or a single vessel bifurcation [56, 60–62], the new tool extended the applicability of structured meshing to multiple non-planar bifurcations by

taking into account the vessel twisting.

To test whether a structured mesh could be beneficial for a blood flow simulation compared to an automatically-generated unstructured mesh, a series of structured hexahedral meshes and a series of unstructured hybrid meshes were generated in the same coronary artery for the calculation of the Wall Shear Stress (WSS) using a CFD analysis. The advantage of using a structured mesh appeared clear from the lower number of elements required to obtain a mesh-insensitive WSS (within a desired tolerance) and from the higher accuracy that could be reached by progressively refining the mesh, enabling a more accurate, faster and less memory-demanding computation as compared to an unstructured mesh [73]. This finding is not obvious and represents an issue against the trend of using automatically-generated unstructured meshes, as in a major part of the computational vascular research, at least when a detailed discussion of the results is not preceded by an equally-detailed mesh sensitivity analysis. The simulation of blood flow using a structured hexahedral mesh benefits from the high number of nodes per cell, the alignment of the mesh cells and gridlines with the predominant flow (i.e. the flow along the vessel centerlines) and the possibility to stretch the cells in the direction of the predominant flow, generating an anisotropic grid. These results motivated further methodological developments of the mesh generation.

In Chapter 3, a framework to generate a mesh from a triangulated surface model of a single nearly-planar bifurcation (the vascular BIFurcation MESHer, Bifmesh) was implemented. The circularity of the sections of the vessel described in Chapter 2 was not necessary for the spline reconstruction. As such, the spline reconstruction could be applied to non-tubular vessels. By clicking on a few points on the monitor, a predefined bifurcation topology was applied to the specific vessel geometry by cutting the surface with planes in a slicing operation. Six vessel semi-branches were then reconstructed by means of Bezier splines and meshed using a sweeping approach, thus with a constant cross-section topology. As a result, a structured mesh of the bifurcation's lumen was generated. By applying the Bifmesh on the outer vessel wall (either segmented from medical images or artificially constructed), the arterial wall was also meshed with layers of hexahedrons. The Bifmesh functionalities have been embedded in a Graphical User Interface (GUI) to generate a high-quality mesh of the lumen and wall of a vessel bifurcation from a given STL model with only few clicks and within two minutes' time by a non-expert user [112]. In the wall, the layered design of the mesh resembled the intima, media and adventitia structures, and allowed assigning layer-specific material properties. Moreover, each element could be equipped with a material orientation for the implementation of an anisotropic material model, capturing the structural role of the collagen fibers that reinforce the arterial wall in vivo. A similar layer-specific

material specification would require a much finer mesh if an unstructured mesh would be used, with a consequent more expensive computation. Remarkably, the ease of generating a mesh using the Bifmesh derived from the predefined vessel topology, which, however, restricted its applicability to a specific anatomical vascular subclass (i.e. a bifurcation) [108].

In Chapter 4, the meshing framework has been generalized to enable its applicability to all kind of vascular networks: a bifurcation, a trifurcation, an n-furcation, a stenosis, an aneurysm and a combination of them. The vascular-TREE MESHer (Treemesh) is a powerful and flexible tool because it does not impose any limitation on the topology of the vessel. The mesh was generated in two steps: first, the topology of the vascular tree was designed by assembling a number of blocks, asking for the user's intervention; second, the blocks were filled with a structured mesh and projected towards the vessel surface in a fully automatic procedure. To facilitate the first step, the centerlines' algorithms implemented in VMTK [47] could be applied to guide the design of the blocks inside the vascular tree, reducing the mesh generation time. The Treemesh could be easily extended to mesh the vascular wall if the outer wall surface was provided. Alternatively, the maximum inscribed-sphere radius could be used as a measure of the local vessel size, which, in turn, could serve as an indicator of the location-specific wall thickness based on anatomical relations (wall-to-lumen ratio). The Treemesh allowed defining the number of elements of a computational mesh *a priori* by choosing a set of topological and geometrical parameters. As a result, after generating a first mesh, increasingly finer meshes could be generated by recycling the blocks of the first step and adjusting some parameters of the second step to reach the required resolution. The shape of the elements was preserved both in the coarser and finer meshes, resulting in an optimal mesh quality for computational purposes. The structure of the lumen mesh was reproduced in the wall mesh, with a layered assembly of elements, and the orientation of each cell matching the position occupied within the vessel. As such, the orientation of the vascular collagen fibers could be defined for the implementation of an anisotropic material model, as for the Bifmesh. The Treemesh represents a unique tool in terms of generality and robustness, as demonstrated on two cases of interest: a human aortic arch and an abdominal aortic aneurysm [141].

The methodological advances in the structured mesh generation would not represent an added value for the research without applications. In Chapter 5 the published applications of the Bifmesh and Treemesh in the pre-processing phase of several computational investigations were reported. The Bifmesh contributed to the mesh generation in (1) a parametric model of an arterio-venous graft for hemodialysis with a swirling design for the improvement of the hemodynamics (manuscript in preparation), (2) the arterial wall of a carotid artery bifurcation for the comparison of different

self-expanding stents [51, 52], and (3) a parametric model of a coronary bifurcation for the evaluation of balloon-expandable stents [160]. The Treemesh contributed to the mesh generation in (1) the abdominal aorta of five mice to investigate the initiation of an aneurysm [191], (2) two human aortic arches to quantify the impact of different strategies of imposing in vivo measured boundary conditions [127], (3) a silicone model of a stenosed coronary bifurcation for the assessment of the computational accuracy of the FEA of stenting against an experimental counterpart [192] and (4) a carotid artery bifurcation for the characterization of the arterial wall motion [193]. The applications of the framework on these and other ongoing studies at one year time from the development of the framework indicate that the original mission has been accomplished and that the novel mesh methodology had a valuable impact on the research.

Because of the need to apply the image-based analysis to large domains and perform computationally-demanding simulations (e.g. multi-physics analyses, multi-scale models), the computation requirements in terms of memory and CPU time become an issue, especially when a high performance computational infrastructure is not available. Moreover, a large output file generated from a computational analysis using a large mesh may be difficult to analyze in the post-processing phase. A solution is reducing the number of elements in the portion of the domain outside the region of interest, not only by stretching the elements but also by refining the mesh in the cross-section. A topological refinement based on transitional blocks has been implemented to increase or decreased the number of elements in a vessel cross-section, maintaining a conformal mesh. This is a significant improvement in the image-based structured mesh generation and may be useful for future applications of the Bifmesh and Treemesh.

In Chapter 6, the hemodynamic impact of carotid artery stenting (CAS) on a patient was assessed using pre-operative data. Based on a CT angiography image of a mildly-stenosed carotid artery, the CAS was simulated using FEA to predict the post-stenting vessel lumen. The computation was performed on structured meshes generated using the Bifmesh facility. The stented-vessel lumen, constructed from the structural domain, was then meshed using tetrahedrons and perfused using CFD and realistic time-dependent boundary conditions. A time-dependent pressure was applied to the inlet and impedances taken from a healthy carotid artery were applied to the outlets. The boundary conditions were assumed insensitive to the change of the shape of the lumen after inserting the stent. From the predicted post-stenting flow, WSS-based hemodynamic indicators of abnormal flow were calculated and matched with the post-implantation geometry. Critical regions were found (1) in regions of stent-to-vessel malapposition, (2) distal to the stent strut interconnections and (3) in the ostium of the external carotid artery, were floating struts disturbed the blood stream [194]. The

combination of an image-based structural analysis and a flow analysis with a realistic set of boundary conditions represents a novel comprehensive approach to simulate patient-specific stenting. Technical solutions to convert a FEA-mesh into a CFD-mesh and to post-process the hemodynamic data were proposed. This computational analysis does not describe an existing in vivo flow, but forecasts the flow that would establish after the insertion of a stent in a subject-specific vessel. In a future, such a blood flow simulation based on image-based virtual stenting may provide a clinician with a map of the post-CAS hemodynamics which may help to select the most appropriate device.

7.2 Future directions

With the technological advances reported in this thesis, the structured mesh generation has the potential to become the standard in vascular computational analysis and may be extended to other research fields, such as orthopaedic biomechanics. However, to motivate the use of structured meshes, which would represent a major change in the image-based analysis, (1) the advantages of using a structured mesh over an unstructured mesh need to be extensively demonstrated and (2) the mesh generation framework needs to be generally applicable and easy to use, from the segmentation to the solver.

7.2.1 Advantage of choosing a structured mesh

An initial comparison of the possible meshing options has shown some of the advantages of using a structured mesh in the arterial CFD for the computation of the WSS. However, the effect of the mesh style needs to be further investigated. First, the pressure and flow data at the boundaries of a multi-branched vascular district can be estimated using a computational model and compared to an experimental counterpart. Second, the sensitivity to the mesh size of some (critical) hemodynamic parameters, such as the relative residence time and the helical content, for the computation of the flow in the vicinity of the wall and in the bulk, respectively, should be evaluated in a series of structured and in a series of unstructured meshes. Third, the performance of a structured mesh in a flow domain without a predominant flow direction, such as in an aneurysm, should be assessed. Fourth, a comparison of structured versus unstructured meshes should be performed on the same bench test but using different solvers.

An advantage of using a structured mesh in the FEA of arterial districts

is the possibility of stretching the elements, generating geometrically-anisotropic meshes. As a result, the elements can be layered in the arterial wall without the need of increasing the circumferential and longitudinal resolution and without losing the element quality. Another advantage is the possibility of using the orientation of the elements as a surrogate of the local material orientations to specify a material anisotropy. However, apart from these design considerations, the computational differences between a structured and an unstructured mesh of an artery in a FEA remain unexplored.

The reduction of the run time in the CFD and FEA applications would be amplified in case of a large domain and a multi-physics simulation. For example, a partitioned approach to solve an FSI analysis requires a number of coupling iterations in each time step with a consequent enlargement of the calculation time [195]. An even more critical case would be an FSI simulation with flow boundary conditions specified by means of an impedance model. Reducing the run time in both the structural solver and the flow solver would drastically speed up the FSI calculation.

7.2.2   Ease of use and extension of the applicability of the mesh generation framework

In this thesis a graphical user interface (GUI) to ease the mesh generation was created for the Bifmesh and allowed to fully automate the mesh generation process by only requiring few clicks by the user. The software pyFormex provides powerful tools to interface the user with the code, using dedicated menus and widgets. Current work is aiming at generating a GUI for the Treemesh to facilitate the application of the framework. While the different blood vessels represent challenging districts for the structured mesh generation, other districts of the human body could also be meshed using the same framework. Some examples are the human femur, which resembles the tubular shape of the lumen of a blood vessel, and the eye, which resembles a sphere.

After generating the mesh, the nodal coordinates and the element connectivity need to be moved to the solver. In general, a text file enables to import or export a mesh but different text formats are required for different solvers. Therefore, some efforts to implement the syntax to read and write a mesh in the most common formats would enlarge the applicability of the novel meshing framework.

Some additional features may be crucial for niche applications. The conformal mesh refinement strategy may serve to further reduce the computational time in case of large models. As an example, a blood vessel may

be discretized with different cross-sectional resolutions, depending on the accuracy required at that location. One would like to have a very coarse mesh outside - and a very fine mesh inside - the region of interest and, as an extreme case, one single element in the entire cross-section where the boundary conditions are applied. Another usefull feature would be to move a mesh without changing the element connectivity, by displacing the internal nodes in response to a displacement applied to the surface nodes, without degrading the mesh quality, to facilitate an FSI analysis.

The mesh generation method is currently implemented as a pyFormex plugin and is available, via research collaboration and gentlemen's agreement, as open source code for academic use. In future, depending on the request, it may be either freely released for research, as an open source application, or further improved for commercial purposes.

List of Figures

List of Tables

Bibliography

[1] B. Boon. Leonardo da Vinci on atherosclerosis and the function of the sinuses of Valsalva. *Neth Heart J*, 17:496–499, 2009.

[2] BBC, `http://www.bbc.co.uk/science/leonardo/gallery/heart.shtmlhttp://www.bbc.co.uk/science/leonardo/gallery/heart.shtml`, (accessed 7 July 2011).

[3] World Health Organization: cardiovascular diseases, `http://www.who.int/cardiovascular_diseases/en/`, (accessed 7 July 2011).

[4] S. Allender, P. Scarborough, V. Peto, M. Rayner, J. Leal, R. Luengo-Fernandez, and A. Gray. European cardiovascular disease statistics. 2008.

[5] Wikipedia: blood vessel, `http://en.wikipedia.org/wiki/Blood_vessel`, (accessed 7 July 2011).

[6] A. M. Malek, S. L. Alper, and S. Izumo. Hemodynamic shear stress and its role in atherosclerosis. *JAMA*, 282:2035–2042, 1999.

[7] Wikipedia: artery, `http://en.wikipedia.org/wiki/Artery` (accessed 8 August 2011).

[8] G. A. Holzapfel, G. Sommer, C. T. Gasser, and P. Regitnig. Determination of layer-specific mechanical properties of human coronary arteries with nonatherosclerotic intimal thickening and related constitutive modeling. *Am. J. Physiol. Heart Circ. Physiol.*, 289:H2048–2058, 2005.

[9] R. Ross. The pathogenesis of atherosclerosis: a perspective for the 1990s. *Nature*, 362:801–809, 1993.

[10] N. M. Caplice, T. J. Bunch, P. G. Stalboerger, S. Wang, D. Simper, D. V. Miller, S. J. Russell, M. R. Litzow, and W. D. Edwards. Smooth muscle cells in human coronary atherosclerosis can originate from cells administered at marrow transplantation. *Proc. Natl. Acad. Sci. U.S.A.*, 100:4754–4759, 2003.

[11] R. Ross and J. A. Glomset. Atherosclerosis and the arterial smooth muscle cell: Proliferation of smooth muscle is a key event in the genesis of the lesions of atherosclerosis. *Science*, 180:1332–1339, 1973.

[12] R. Ross. The pathogenesis of atherosclerosis–an update. *N. Engl. J. Med.*, 314:488–500, 1986.

[13] H. C. Stary. The sequence of cell and matrix changes in atherosclerotic lesions of coronary arteries in the first forty years of life. *Eur. Heart J.*, 11 Suppl E:3–19, 1990.

[14] A. Didangelos, D. Simper, C. Monaco, and M. Mayr. Proteomics of acute coronary syndromes. *Curr Atheroscler Rep*, 11:188–195, 2009.

[15] Wikipedia: atherosclerosis, `http://en.wikipedia.org/wiki/Atherosclerosis`, (accessed 7 July 2011).

[16] A. Sambola, V. Fuster, and J. J. Badimon. [Role of coronary risk factors in blood thrombogenicity and acute coronary syndromes]. *Rev Esp Cardiol*, 56:1001–1009, 2003.

[17] A. M. Malek and S. Izumo. Control of endothelial cell gene expression by flow. *J Biomech*, 28:1515–1528, 1995.

[18] M. Bongrazio, C. Baumann, A. Zakrzewicz, A. R. Pries, and P. Gaehtgens. Evidence for modulation of genes involved in vascular adaptation by prolonged exposure of endothelial cells to shear stress. *Cardiovasc. Res.*, 47:384–393, 2000.

[19] J. J. Chiu, D. L. Wang, S. Chien, R. Skalak, and S. Usami. Effects of disturbed flow on endothelial cells. *J Biomech Eng*, 120:2–8, 1998.

[20] N. DePaola, P. F. Davies, W. F. Pritchard, L. Florez, N. Harbeck, and D. C. Polacek. Spatial and temporal regulation of gap junction connexin43 in vascular endothelial cells exposed to controlled disturbed flows in vitro. *Proc. Natl. Acad. Sci. U.S.A.*, 96:3154–3159, 1999.

[21] P. P. Hsu, S. Li, Y. S. Li, S. Usami, A. Ratcliffe, X. Wang, and S. Chien. Effects of flow patterns on endothelial cell migration into a zone of mechanical denudation. *Biochem. Biophys. Res. Commun.*, 285:751–759, 2001.

[22] J. E. Phelps and N. DePaola. Spatial variations in endothelial barrier function in disturbed flows in vitro. *Am. J. Physiol. Heart Circ. Physiol.*, 278:H469–476, 2000.

[23] G. A. Truskey, K. M. Barber, T. C. Robey, L. A. Olivier, and M. P. Combs. Characterization of a sudden expansion flow chamber to study the response of endothelium to flow recirculation. *J Biomech Eng*, 117:203–210, 1995.

[24] J. J. Chiu and S. Chien. Effects of disturbed flow on vascular endothelium: pathophysiological basis and clinical perspectives. *Physiol. Rev.*, 91:327–387, 2011.

[25] M. J. Starmans-Kool, A. V. Stanton, S. Zhao, X. Y. Xu, S. A. Thom, and A. D. Hughes. Measurement of hemodynamics in human carotid artery using ultrasound and computational fluid dynamics. *J. Appl. Physiol.*, 92:957–961, 2002.

[26] S.A. Berceli, V.S. Warty, R.A. Sheppeck, W.A. Mandarino, S.K. Tanksale, and H.S. Borovetz. Hemodynamics and low density lipoprotein metabolism. Rates of low density lipoprotein incorporation and degradation along medial and lateral walls of the rabbit aorto-iliac bifurcation. *Arteriosclerosis*, 10:686–694, 1990.

[27] T. Karino, T. Asakura, and S. Mabuchi. Role of hemodynamic factors in atherogenesis. *Adv. Exp. Med. Biol.*, 242:51–57, 1988.

[28] H. N. Sabbah, F. Khaja, J. F. Brymer, E. T. Hawkins, and P. D. Stein. Blood velocity in the right coronary artery: relation to the distribution of atherosclerotic lesions. *Am. J. Cardiol.*, 53:1008–1012, 1984.

[29] C. K. Zarins, D. P. Giddens, B. K. Bharadvaj, V. S. Sottiurai, R. F. Mabon, and S. Glagov. Carotid bifurcation atherosclerosis. Quantitative correlation of plaque localization with flow velocity profiles and wall shear stress. *Circ. Res.*, 53:502–514, 1983.

[30] D. N. Ku, D. P. Giddens, C. K. Zarins, and S. Glagov. Pulsatile flow and atherosclerosis in the human carotid bifurcation. Positive correlation between plaque location and low oscillating shear stress. *Arteriosclerosis*, 5:293–302, 1985.

[31] A. M. Shaaban and A. J. Duerinckx. Wall shear stress and early atherosclerosis: a review. *AJR Am J Roentgenol*, 174:1657–1665, 2000.

[32] M. H. Friedman and D. L. Fry. Arterial permeability dynamics and vascular disease. *Atherosclerosis*, 104:189–194, 1993.

[33] S. G. Carlier, L. C. van Damme, C. P. Blommerde, J. J. Wentzel, G. van Langehove, S. Verheye, M. M. Kockx, M. W. Knaapen, C. Cheng, F. Gijsen, D. J. Duncker, N. Stergiopulos, C. J. Slager, P. W. Serruys, and R. Krams. Augmentation of wall shear stress inhibits neointimal hyperplasia after stent implantation: inhibition through reduction of inflammation? *Circulation*, 107:2741–2746, 2003.

[34] U. Morbiducci, R. Ponzini, G. Rizzo, M. Cadioli, A. Esposito, F. M. Montevecchi, and A. Redaelli. Mechanistic insight into the physiological relevance of helical blood flow in the human aorta: an in vivo study. *Biomech Model Mechanobiol*, 10:339–355, 2011.

[35] U. Morbiducci, R. Ponzini, G. Rizzo, M. Cadioli, A. Esposito, F. De Cobelli, A. Del Maschio, F. M. Montevecchi, and A. Redaelli. In vivo quantification of helical blood flow in human aorta by time-resolved three-dimensional cine phase contrast magnetic resonance imaging. *Ann Biomed Eng*, 37:516–531, 2009.

[36] R. Ponzini, M. Lemma, U. Morbiducci, F. M. Montevecchi, and A. Redaelli. Doppler derived quantitative flow estimate in coronary artery bypass graft: a computational multiscale model for the evaluation of the current clinical procedure. *Med Eng Phys*, 30:809–816, 2008.

[37] A. Swillens, T. De Schryver, L. Lovstakken, H. Torp, and P. Segers. Assessment of numerical simulation strategies for ultrasonic color blood flow imaging, based on a computer and experimental model of the carotid artery. *Ann Biomed Eng*, 37:2188–2199, 2009.

[38] D. Katritsis, L. Kaiktsis, A. Chaniotis, J. Pantos, E. P. Efstathopoulos, and V. Marmarelis. Wall shear stress: theoretical considerations and methods of measurement. *Prog Cardiovasc Dis*, 49:307–329, 2007.

[39] L. Antiga, M. Piccinelli, L. Botti, B. Ene-Iordache, A. Remuzzi, and D. A. Steinman. An image-based modeling framework for patient-specific computational hemodynamics. *Med Biol Eng Comput*, 46:1097–1112, 2008.

[40] S. W. Lee, L. Antiga, J. D. Spence, and D. A. Steinman. Geometry of the carotid bifurcation predicts its exposure to disturbed flow. *Stroke*, 39:2341–2347, 2008.

[41] X. Liu, F. Pu, Y. Fan, X. Deng, D. Li, and S. Li. A numerical study on the flow of blood and the transport of LDL in the human aorta: the physiological significance of the helical flow in the aortic arch. *Am. J. Physiol. Heart Circ. Physiol.*, 297:H163–170, 2009.

[42] X. Liu, Y. Fan, and X. Deng. Effect of spiral flow on the transport of oxygen in the aorta: a numerical study. *Ann Biomed Eng*, 38:917–926, 2010.

[43] X. Liu, Y. Fan, X. Deng, and F. Zhan. Effect of non-Newtonian and pulsatile blood flow on mass transport in the human aorta. *J Biomech*, 44:1123–1131, 2011.

[44] U. Morbiducci, D. Gallo, R. Ponzini, D. Massai, L. Antiga, F. M. Montevecchi, and A. Redaelli. Quantitative analysis of bulk flow in image-based hemodynamic models of the carotid bifurcation: the influence of outflow conditions as test case. *Ann Biomed Eng*, 38:3688–3705, 2010.

[45] U. Morbiducci, D. Gallo, D. Massai, F. Consolo, R. Ponzini, L. Antiga, C. Bignardi, M. A. Deriu, and A. Redaelli. Outflow conditions for image-based hemodynamic models of the carotid bifurcation: implications for indicators of abnormal flow. *J Biomech Eng*, 132:091005, 2010.

[46] D. A. Steinman. Image-based computational fluid dynamics modeling in realistic arterial geometries. *Ann Biomed Eng*, 30:483–497, 2002.

[47] Vascular Modeling Toolkit, `http://www.vmtk.org/`, (accessed 15 July 2011).

[48] Mimics, Materialise NV, Leuven, Belgium, `http://www.materialise.com/mimics`, (accessed 7 July 2011).

[49] D. E. Kiousis, S. F. Rubinigg, M. Auer, and G. A. Holzapfel. A methodology to analyze changes in lipid core and calcification onto fibrous cap vulnerability: The human atherosclerotic carotid bifurcation as an illustratory example. *J. Biomech. Eng.*, 131:121002, 2009.

[50] P. Mortier, G. A. Holzapfel, M. De Beule, D. Van Loo, Y. Taeymans, P. Segers, P. Verdonck, and B. Verhegghe. A novel simulation strategy for stent insertion and deployment in curved coronary bifurcations: comparison of three drug-eluting stents. *Ann Biomed Eng*, 38:88–99, 2010.

[51] M. Conti, D. Van Loo, F. Auricchio, M. De Beule, G. De Santis, B. Verhegghe, A. Pirelli, and A. Odero. Impact of carotid stent cell design on vessel scaffolding: a case study comparing experimental investigation and numerical simulations. *J Endovasc Ther*, 18:397–406, 2011.

[52] F. Auricchio, M. Conti, M. De Beule, G. De Santis, and B. Verhegghe. Carotid artery stenting simulation: from patient-specific images to finite element analysis. *Med Eng Phys*, 33:281–289, 2011.

[53] A. G. Radaelli, L. Augsburger, J. R. Cebral, M. Ohta, D. A. Rüfenacht, R. Balossino, G. Benndorf, D. R. Hose, A. Marzo, R. Metcalfe, P. Mortier, F. Mut, P. Reymond, L. Socci, B. Verhegghe, and A. F. Frangi. Reproducibility of haemodynamical simulations in a subject-specific stented aneurysm model–a report on the Virtual Intracranial Stenting Challenge 2007. *J Biomech*, 41:2069–2081, 2008.

[54] C. Capelli, A. M. Taylor, F. Migliavacca, P. Bonhoeffer, and S. Schievano. Patient-specific reconstructed anatomies and computer simulations are fundamental for selecting medical device treatment: application to a new percutaneous pulmonary valve. *Philos Transact A Math Phys Eng Sci*, 368:3027–3038, 2010.

[55] Y. Zhang, Y. Bazilevs, S. Goswami, C. L. Bajaj, and T. J. Hughes. Patient-Specific Vascular NURBS Modeling for Isogeometric Analysis of Blood Flow. *Comput Methods Appl Mech Eng*, 196:2943–2959, 2007.

[56] B. J. Wolters, M. C. Rutten, G. W. Schurink, U. Kose, J. de Hart, and F. N. van de Vosse. A patient-specific computational model of fluid-structure interaction in abdominal aortic aneurysms. *Med Eng Phys*, 27:871–883, 2005.

[57] M. Xenos, S. H. Rambhia, Y. Alemu, S. Einav, N. Labropoulos, A. Tassiopoulos, J. J. Ricotta, and D. Bluestein. Patient-based abdominal aortic aneurysm rupture risk prediction with fluid structure interaction modeling. *Ann Biomed Eng*, 38:3323–3337, Nov 2010.

[58] T. Baker. Automatic mesh generation for complex three-dimensional regions using a constrained Delaunay triangulation. *Engineering with Computers*, 5:161–175, 1989.

[59] L. Antiga. *Patient-Specific Modeling of Geometry and Blood Flow in Large Arteries*. PhD thesis, Politecnico di Milano, Italy, 2002.

[60] Q. Long, X. Y. Xu, M. W. Collins, M. Bourne, and T. M. Griffith. Magnetic resonance image processing and structured grid generation of a human abdominal bifurcation. *Comput Methods Programs Biomed*, 56:249–259, 1998.

[61] L. Antiga, B. Ene-Iordache, L. Caverni, G. P. Cornalba, and A. Remuzzi. Geometric reconstruction for computational mesh generation of arterial bifurcations from CT angiography. *Comput Med Imaging Graph*, 26:227–235, 2002.

[62] C.S. Verma, P.F. Fischer, S.E. Lee, and F. Loth. An all-hex meshing strategy for bifurcation geometries in vascular flow simulation. Presented at the 14th International Meshing Roundtable. Available at `http://www.imr.sandia.gov/papers/imr14/verma.pdf`, (accessed 7 July 2011).

[63] A. Creane, E. Maher, S. Sultan, N. Hynes, D. J. Kelly, and C. Lally. Finite element modelling of diseased carotid bifurcations generated from in vivo computerised tomographic angiography. *Comput. Biol. Med.*, 40:419–429, 2010.

[64] M. Auer and T. C. Gasser. Reconstruction and finite element mesh generation of abdominal aortic aneurysms from computerized tomography angiography data with minimal user interactions. *IEEE Trans Med Imaging*, 29:1022–1028, 2010.

[65] P. Knupp. Next-Generation Sweep Tool: A Method for Generating All-Hex Meshes on Two-And-One-Half Dimensional Geometries. Presented at the 7th International Meshing Roundtable. Available at `http://citeseerx.ist.psu.edu/viewdoc/summary?doi=10.1.1.43.1382`, (accessed 7 July 2011).

[66] T. Blacker. The Cooper Tool. Presented at the 5th International Meshing Roundtable. Available at `http://www.imr.sandia.gov/papers/abstracts/Bl22.html`, (accessed 7 July 2011).

[67] J. Shepherd, S. Mitchell, P. Knupp, and D. White. Methods for MultiSweep Automation. Presented at the 9th International Meshing Roundtable. Available at `http://citeseerx.ist.psu.edu/viewdoc/summary?doi=10.1.1.31.8263`, (accessed 7 July 2011).

[68] D. White, S. Saigal, and Owen S. Automatic Decomposition of Multi-Sweep Volumes. *Engineering With Computers*, 20:222–236, 2004.

[69] M. Staten, S. Canaan, and Owen S. BMSweep: Locating Interior Nodes During Sweeping. Presented at the 7th International Meshing Roundtable. Available at `http://www.springerlink.com/content/hqfdnrgh9nmnakvp/`, (accessed 7 July 2011).

[70] M. Scott, M. Earp, and Benzley S. Adaptive Sweeping Techniques. Presented at the 14th International Meshing Roundtable. Available at `http://www.imr.sandia.gov/papers/imr14/scott.pdf`, (accessed 7 July 2011).

[71] J. Shepherd, Y. Zhang, C.J. Tuttle, and C.T. Silva. Quality Improvement and Boolean-like Cutting Operations in Hexahedral Meshes. Presented at the 10th ISGG Conference on Numerical Grid Generation. Available at `https://cfwebprod.sandia.gov/cfdocs/CCIM/docs/isgg_octree.pdf`, (accessed 7 July 2011).

[72] O. C. Zienkiewicz and R. L. Taylor, editors. *The Finite Element Method. Solid Mechanics.* Butterworth Heinemann, Oxford, 2000.

[73] G. De Santis, P. Mortier, M. De Beule, P. Segers, P. Verdonck, and B. Verhegghe. Patient-specific computational fluid dynamics: structured mesh generation from coronary angiography. *Med Biol Eng Comput*, 48:371–380, 2010.

[74] Ansys Inc., Canonsburg, USA, `http://www.ansys.com/Products/Simulation+Technology/Fluid+Dynamics`, (accessed 7 July 2011).

[75] pyFormex, `http://www.pyformex.org`, (accessed 7 July 2011).

[76] T. Frauenfelder, E. Boutsianis, T. Schertler, L. Husmann, S. Leschka, D. Poulikakos, B. Marincek, and H. Alkadhi. In-vivo flow simulation in coronary arteries based on computed tomography datasets: feasibility and initial results. *Eur Radiol*, 17:1291–1300, 2007.

[77] N. H. Pijls, B. De Bruyne, K. Peels, P. H. Van Der Voort, H. J. Bonnier, J. J. Bartunek J Koolen, and J. J. Koolen. Measurement of fractional flow reserve to assess the functional severity of coronary-artery stenoses. *N. Engl. J. Med.*, 334:1703–1708, 1996.

[78] N. H. Pijls, P. van Schaardenburgh, G. Manoharan, E. Boersma, J. W. Bech, M. van't Veer, F. Bar, J. Hoorntje, J. Koolen, W. Wijns, and B. de Bruyne. Percutaneous coronary intervention of functionally nonsignificant stenosis: 5-year follow-up of the DEFER Study. *J. Am. Coll. Cardiol.*, 49:2105–2111, 2007.

[79] P. A. Tonino, B. De Bruyne, N. H. Pijls, U. Siebert, F. Ikeno, M. van' t Veer, V. Klauss, G. Manoharan, T. Engstrom, K. G. Oldroyd, P. N. Ver Lee, P. A. MacCarthy, W. F. Fearon, N. Pijls, W. Fearon, B. De Bruyne, P. Tonino, N. Pijls, W. Fearon, B. De Bruyne, U. Siebert, P. Tonino, E. Eeckhout, M. El Gamal, E. Barbato, M. Kern, J. Hodgson, U. Siebert, R. Gothe, B. Bornschein, W. Fearon, F. Ikeno, T. Brinton, D. Lee, S. Williams, A. Yeung, P. Ver Lee, A. Wiseman, G. Crespo, R. Fincke, P. Vom Eigen, M. Lim, R. Longnecker, M. Leesar, V. Yalamanchili, S. Ikram, M. Ragosta, L. Gimple, L. Lipson, E. Powers, K. Oldroyd, M. Lindsay, S. Robb, S. Watkins, G. Manoharan, P. Tierney, P. MacCarthy, A. Shah, M. Thomas, J. Hill, A. Baumbach, P. Wilde, A. Nightingale, A. Skyme-Jones, E. Barnes, I. Herzfeld, M. Tornerud, P. Alstrom, N. Witt, F. Schersten, J. Bonnier, C. Botman, B. Brueren, J. van Dantzig, J. Koolen, H. Michels, C. Peels, N. Pijls, P. Tonino, V. Klauss, J. Rieber, T. Schiele, M. Leibig, Y. Sohn, J. Sollner, W. Bojara, M. Lindstaedt, A. Yazar, G. Riess, G. Werner, T. Engstrom, H. Kelbaek, E. Jorgensen, S. Helqvist, K. Saunamaki, P. Clemmensen, J. Kastrup, K. Rasmussen, O. Frobert, B. De Bruyne, N. Melikian, J. Bartunek, E. Wyffels, G. Heyndrickx, W. Wijns, M. Vanderheyden, and H. Batjoens. Fractional flow reserve versus angiography for guiding percutaneous coronary intervention. *N. Engl. J. Med.*, 360:213–224, 2009.

[80] L. Goubergrits, E. Wellnhofer, U. Kertzscher, K. Affeld, C. Petz, and H. C. Hege. Coronary artery WSS profiling using a geometry reconstruction based on biplane angiography. *Ann Biomed Eng*, 37:682–691, 2009.

[81] J. V. Soulis, G. D. Giannoglou, V. Papaioannou, G. E. Parcharidis, and G. E. Louridas. Low-Density Lipoprotein concentration in the normal Left Coronary Artery tree. *Biomed Eng Online*, 7:26, 2008.

[82] E. Wellnhofer, L. Goubergrits, U. Kertzscher, K. Affeld, and E. Fleck. Novel non-dimensional approach to comparison of wall shear stress distributions in coronary arteries of different groups of patients. *Atherosclerosis*, 202:483–490, 2009.

[83] L. Antiga, B. Ene-Iordache, and A. Remuzzi. Computational geometry for patient-specific reconstruction and meshing of blood vessels from MR and CT angiography. *IEEE Trans Med Imaging*, 22:674–684, 2003.

[84] L. Baghdadi, D. A. Steinman, and H. M. Ladak. Template-based finite-element mesh generation from medical images. *Comput Methods Programs Biomed*, 77:11–21, 2005.

[85] B. Holzapfel and Oeltze, editors. *3D visualization of vasculature: An overview.* Springer-Verlag Berlin, Berlin, 2008.

[86] E. Boutsianis, H. Dave, T. Frauenfelder, D. Poulikakos, S. Wildermuth, M. Turina, Y. Ventikos, and G. Zund. Computational simulation of intracoronary flow based on real coronary geometry. *Eur J Cardiothorac Surg*, 26:248–256, 2004.

[87] P. W. Longest and C. Kleinstreuer. Numerical simulation of wall shear stress conditions and platelet localization in realistic end-to-side arterial anastomoses. *J Biomech Eng*, 125:671–681, 2003.

[88] P. W. Longest and C. Kleinstreuer. Particle-hemodynamics modeling of the distal end-to-side femoral bypass: effects of graft caliber and graft-end cut. *Med Eng Phys*, 25:843–858, 2003.

[89] P. W. Longest, C. Kleinstreuer, and A. Deanda. Numerical simulation of wall shear stress and particle-based hemodynamic parameters in pre-cuffed and streamlined end-to-side anastomoses. *Ann Biomed Eng*, 33:1752–1766, 2005.

[90] D. A. Steinman, D. A. Vorp, and C. R. Ethier. Computational modeling of arterial biomechanics: insights into pathogenesis and treatment of vascular disease. *J. Vasc. Surg.*, 37:1118–1128, 2003.

[91] S. Prakash and C. R. Ethier. Requirements for mesh resolution in 3D computational hemodynamics. *J Biomech Eng*, 123:134–144, 2001.

[92] Philips Medical Systems, Best, The Nederlands, `http://www.healthcare.philips.com`, (accessed 20 July 2011).

[93] P. Agostoni, G. Biondi-Zoccai, G. Van Langenhove, K. Cornelis, P. Vermeersch, C. Convens, C. Vassanelli, P. Van Den Heuvel, F. Van Den Branden, and S. Verheye. Comparison of assessment of native coronary arteries by standard versus three-dimensional coronary angiography. *Am. J. Cardiol.*, 102:272–279, 2008.

[94] Wikipedia: coronary catheterization, `http://en.wikipedia.org/wiki/Coronary_catheterization`, (accessed 12 July 2011).

[95] J. Peiro, S. J. Sherwin, and S. Giordana. Automatic reconstruction of a patient-specific high-order surface representation and its application to mesh generation for CFD calculations. *Med Biol Eng Comput*, 46:1069–1083, 2008.

[96] E. Catmull and R. Rom, editors. *Computer aided geometric design, chapter a class of local interpolating splines.* Academic Press, New York, 1974.

[97] J. Svensson, R. Gardhagen, E. Heiberg, T. Ebbers, D. Loyd, T. Lanne, and M. Karlsson. Feasibility of patient specific aortic blood flow CFD simulation. *Med Image Comput Comput Assist Interv*, 9:257–263, 2006.

[98] L. Goubergrits, U. Kertzscher, B. Schoneberg, E. Wellnhofer, C. Petz, and H. C. Hege. CFD analysis in an anatomically realistic coronary artery model based on non-invasive 3D imaging: comparison of magnetic resonance imaging with computed tomography. *Int J Cardiovasc Imaging*, 24:411–421, 2008.

[99] Bumper cluster, `http://bumps.ugent.be/bumper/`, (accessed 20 July 2011).

[100] Nichols W.W. and O'Rourke M.F. *McDonald's blood flow in Arteries.* Edward Arnold, London, 2005.

[101] J. V. Soulis, T. M. Farmakis, G. D. Giannoglou, and G. E. Louridas. Wall shear stress in normal left coronary artery tree. *J Biomech*, 39:742–749, 2006.

[102] E. Wellnhofer, L. Goubergrits, U. Kertzscher, and K. Affeld. In-vivo coronary flow profiling based on biplane angiograms: influence of geometric simplifications on the three-dimensional reconstruction and wall shear stress calculation. *Biomed Eng Online*, 5:39, 2006.

[103] S. Vinchurkar and P.W. Longest. Evaluation of hexahedral, prismatic and hybrid mesh styles for simulating respiratory aerosol dynamics. *Comput Fluids*, 37:317–331, 2008.

[104] P. W. Longest and S. Vinchurkar. Effects of mesh style and grid convergence on particle deposition in bifurcating airway models with comparisons to experimental data. *Med Eng Phys*, 29:350–366, 2007.

[105] 3D Slicer, `http://www.slicer.org/`, (accessed 20 July 2011).

[106] OsiriX, `http://www.osirix-viewer.com/`, (accessed 20 July 2011).

[107] Tetgen, `http://tetgen.berlios.de/`, (accessed 15 July 2011).

[108] G. De Santis, M. De Beule, P. Segers, P. Verdonck, and B. Verhegghe. Patient-specific computational haemodynamics: generation of structured and conformal hexahedral meshes from triangulated surfaces of vascular bifurcations. *Comput Methods Biomech Biomed Engin*, 2011, (in press).

[109] B. K. Podesser, F. Neumann, M. Neumann, W. Schreiner, G. Wollenek, and R. Mallinger. Outer radius-wall thickness ratio, a postmortem quantitative histology in human coronary arteries. *Acta Anat (Basel)*, 163:63–68, 1998.

[110] Fluent Inc. *Gambit Version 2.3 User's Guide.* Lebanon, New Hampshire, 2006.

[111] Abaqus CAE, Simulia Inc., Providence, US, `http://www.simulia.com/products/abaqus_cae.html`, (accessed 15 July 2011).

[112] Bifmesh tutorial, `http://www.youtube.com/watch?v=T1pVFCzrmGI`, (accessed 20 July 2011).

[113] F.R. Arko, E.H. Murphy, C.M. Davis, E.D. Johnson, S.T. Smith, and C.K. Zarins. Dynamic geometry and wall thickness of the aortic neck of abdominal aortic aneurysms with intravascular ultrasonography. *Acta Anat (Basel)*, 46:891–897, 2007.

[114] B. Bijnens, P. Rudenick, and A. Evangelista. Assessing aortic strain and stiffness: don't forget the physics and engineering. *Heart*, 97:339; author reply 340, 2011.

[115] L. Antiga and D. A. Steinman. Robust and objective decomposition and mapping of bifurcating vessels. *IEEE Trans Med Imaging*, 23:704–713, 2004.

[116] P. Murdoch, S. Benzley, T. Blacker, and S.A. Mitchell. The spatial twist continuum: A connectivity based method for representing allhexahedral finite element meshes. Finite Elements in Analysis and Design. *Finite Elements in Analysis and Design*, 28:137–149, 1997.

[117] J. E. Moore, C. Xu, S. Glagov, C. K. Zarins, and D. N. Ku. Fluid wall shear stress measurements in a model of the human abdominal aorta: oscillatory behavior and relationship to atherosclerosis. *Atherosclerosis*, 110:225–240, 1994.

[118] I. L. Gordon, C. A. Kohl, M. Arefi, R. A. Complin, and M. Vulpe. Spinal cord injury increases the risk of abdominal aortic aneurysm. *Am Surg*, 62:249–252, 1996.

[119] J. F. Vollmar, E. Paes, P. Pauschinger, E. Henze, and A. Friesch. Aortic aneurysms as late sequelae of above-knee amputation. *Lancet*, 2:834–835, 1989.

[120] J. J. Yeung, H. J. Kim, T. A. Abbruzzese, I. E. Vignon-Clementel, M. T. Draney-Blomme, K. K. Yeung, I. Perkash, R. J. Herfkens, C. A. Taylor, and R. L. Dalman. Aortoiliac hemodynamic and morphologic adaptation to chronic spinal cord injury. *J. Vasc. Surg.*, 44:1254–1265, 2006.

[121] A. Daugherty and L. A. Cassis. Mouse models of abdominal aortic aneurysms. *Arterioscler. Thromb. Vasc. Biol.*, 24:429–434, 2004.

[122] K. Saraff, F. Babamusta, L. A. Cassis, and A. Daugherty. Aortic dissection precedes formation of aneurysms and atherosclerosis in angiotensin II-infused, apolipoprotein E-deficient mice. *Arterioscler. Thromb. Vasc. Biol.*, 23:1621–1626, 2003.

[123] C. Barisione, R. Charnigo, D. A. Howatt, J. J. Moorleghen, D. L. Rateri, and A. Daugherty. Rapid dilation of the abdominal aorta during infusion of angiotensin II detected by noninvasive high-frequency ultrasonography. *J. Vasc. Surg.*, 44:372–376, 2006.

[124] A. Daugherty, M. W. Manning, and L. A. Cassis. Angiotensin II promotes atherosclerotic lesions and aneurysms in apolipoprotein E-deficient mice. *J. Clin. Invest.*, 105:1605–1612, 2000.

[125] B. Vandeghinste, B. Trachet, M. Renard, C. Casteleyn, S. Staelens, B. Loeys, P. Segers, and S. Vandenberghe. Replacing vascular corrosion casting by in vivo micro-CT imaging for building 3D cardiovascular models in mice. *Mol Imaging Biol*, 13:78–86, 2011.

[126] E. A. Finol, K. Keyhani, and C. H. Amon. The effect of asymmetry in abdominal aortic aneurysms under physiologically realistic pulsatile flow conditions. *J Biomech Eng*, 125:207–217, 2003.

[127] D. Gallo, G. De Santis, Negri F., Tresoldi D., Ponzini R., Massai D., Deriu M., Segers P., Verhegghe B., Rizzo G., and U. Morbiducci. On the use of in vivo measured flow rates as boundary conditions

for image-based hemodynamic models of abnormal flow. *Ann Biomed Eng*, 2011, (submitted).

[128] N. Shahcheraghi, H. A. Dwyer, A. Y. Cheer, A. I. Barakat, and T. Rutaganira. Unsteady and three-dimensional simulation of blood flow in the human aortic arch. *J Biomech Eng*, 124:378–387, 2002.

[129] C. Y. Wen, A. S. Yang, L. Y. Tseng, and J. W. Chai. Investigation of pulsatile flowfield in healthy thoracic aorta models. *Ann Biomed Eng*, 38:391–402, 2010.

[130] M. S. Olufsen. Structured tree outflow condition for blood flow in larger systemic arteries. *Am. J. Physiol.*, 276:H257–268, 1999.

[131] A. D. Augst, D. C. Barratt, A. D. Hughes, S. A. Thom, and X. Y. Xu. Various issues relating to computational fluid dynamics simulations of carotid bifurcation flow based on models reconstructed from three-dimensional ultrasound images. *Proc Inst Mech Eng H*, 217:393–403, 2003.

[132] A. Veneziani and C. Vergara. Flow rate defective boundary conditions in haemodynamics simulations. *Int Journ Num Meth Fluids*, 47:803–816, 2005.

[133] I. E. Vignon-Clementel, C. A. Figueroa, K. E. Jansen, and C. A. Taylor. Outflow boundary conditions for three-dimensional finite element modeling of blood flow and pressure in arteries. *Comput Methods Appl Mech Engrg*, 195:3776–3796, 2006.

[134] L. Grinberg and G. E. Karniadakis. Outflow boundary conditions for arterial networks with multiple outlets. *Ann Biomed Eng*, 36:1496–1514, 2008.

[135] H. C. Groen, L. Simons, Q. J. van den Bouwhuijsen, E. M. Bosboom, F. J. Gijsen, A. G. van der Giessen, F. N. van de Vosse, A. Hofman, A. F. van der Steen, J. C. Witteman, A. van der Lugt, and J. J. Wentzel. MRI-based quantification of outflow boundary conditions for computational fluid dynamics of stenosed human carotid arteries. *J Biomech*, 43:2332–2338, 2010.

[136] A. G. van der Giessen, H. C. Groen, P. A. Doriot, P. J. de Feyter, A. F. van der Steen, F. N. van de Vosse, J. J. Wentzel, and F. J. Gijsen. The influence of boundary conditions on wall shear stress distribution in patients specific coronary trees. *J Biomech*, 44:1089–1095, 2011.

[137] L. Formaggia, J. F. Gerbeau, Nobile F., and A. Quarteroni. On the Coupling of 3D and 1D Navier-Stokes Equations for Flow Problems in Compliant Vessels. *Comput Meth Appl Mech Eng*, 191:561–582, 2001.

[138] A. Quarteroni, S. Ragni, and Veneziani A. Coupling Between Lumped and Distributed Models for Blood Flow Problems. *Comput Visual Sci*, 4:111–124, 2001.

[139] H. J. Kim, C. A. Figueroa, T. J. R. Hughes, K. E. Jansen, and Taylor C. A. Augmented Lagrangian Method for Constraining the Shape of Velocity Profiles at Outlet Boundaries for Three-Dimensional Finite Element Simulations of Blood Flow. *Comput Methods Appl Mech Engrg*, 198:3551–3556, 2009.

[140] N. Westerhof, Lankhaar J. W., and B. E. Westerhof. The Arterial Windkessel. *Med Biol Eng Comput*, 47:131–141, 2009.

[141] G. De Santis, M. De Beule, K. Van Canneyt, P. Segers, P. Verdonck, and B. Verhegghe. Full-hexahedral structured meshing for image-based computational vascular modeling. *Med Eng Phys*, 2011, (in press).

[142] M. Allon. Current management of vascular access. *Clin J Am Soc Nephrol*, 2:786–800, 2007.

[143] M. F. Fillinger, E. R. Reinitz, R. A. Schwartz, D. E. Resetarits, A. M. Paskanik, D. Bruch, and C. E. Bredenberg. Graft geometry and venous intimal-medial hyperplasia in arteriovenous loop grafts. *J. Vasc. Surg.*, 11:556–566, 1990.

[144] P. Roy-Chaudhury, L. M. Spergel, A. Besarab, A. Asif, and P. Ravani. Biology of arteriovenous fistula failure. *J. Nephrol.*, 20:150–163, 2007.

[145] U. Morbiducci, R. Ponzini, M. Grigioni, and A. Redaelli. Helical flow as fluid dynamic signature for atherogenesis risk in aortocoronary bypass. A numeric study. *J Biomech*, 40:519–534, 2007.

[146] Veryan Medical, London, UK, `http://www.veryanmed.com/`, (accessed 7 July 2011).

[147] S. Chaturvedi, A. Bruno, T. Feasby, R. Holloway, O. Benavente, S. N. Cohen, R. Cote, D. Hess, J. Saver, J. D. Spence, B. Stern, and J. Wilterdink. Carotid endarterectomy–an evidence-based review: report of the Therapeutics and Technology Assessment Subcommittee of the American Academy of Neurology. *Neurology*, 65:794–801, 2005.

[148] No authors listed. Endovascular versus surgical treatment in patients with carotid stenosis in the Carotid and Vertebral Artery Transluminal Angioplasty Study (CAVATAS): a randomised trial. *Lancet*, 357:1729–1737, 2001.

[149] M. A. Creager, C. J. White, W. R. Hiatt, M. H. Criqui, S. C. Josephs, M. J. Alberts, W. H. Pearce, B. H. Gray, and K. J. Rocha-Singh. Atherosclerotic Peripheral Vascular Disease Symposium II: executive summary. *Circulation*, 118:2811–2825, 2008.

[150] T. L. Forbes. Preliminary results of carotid revascularization endarterectomy vs stenting trial (CREST). *J. Vasc. Surg.*, 51:1300–1301, 2010.

[151] Z. Liu, Z. Shi, Y. Wang, B. Chen, T. Zhu, Y. Si, and W. Fu. Carotid artery stenting versus carotid endarterectomy: systematic review and meta-analysis. *World J Surg*, 33:586–596, 2009.

[152] S. Brahmanandam, E. L. Ding, M. S. Conte, M. Belkin, and L. L. Nguyen. Clinical results of carotid artery stenting compared with carotid endarterectomy. *J. Vasc. Surg.*, 47:343–349, 2008.

[153] Stockx L. Techniques in carotid artery stenting. *European Journal of Radiology*, 60:11–13, 2006.

[154] S. Sayeed, S. F. Stanziale, M. H. Wholey, and M. S. Makaroun. Angiographic lesion characteristics can predict adverse outcomes after carotid artery stenting. *J. Vasc. Surg.*, 47:81–87, 2008.

[155] Centre for X-ray Tomography from Ghent University, `http://www.ugct.ugent.be/`, (accessed 3 Aug 2011).

[156] G. Sommer, P. Regitnig, L. Koltringer, and G. A. Holzapfel. Biaxial mechanical properties of intact and layer-dissected human carotid arteries at physiological and supraphysiological loadings. *Am. J. Physiol. Heart Circ. Physiol.*, 298:898–912, 2010.

[157] V. Legrand, M. Thomas, M. Zelisko, B. De Bruyne, N. Reifart, T. Steigen, D. Hildick-Smith, R. Albiero, O. Darremont, G. Stankovic, M. Pan, J. Flensted Lassen, Y. Louvard, and T. Lefèvre. Percutaneous coronary intervention of bifurcation lesions: state-of-the-art. Insights from the second meeting of the European Bifurcation Club. *EuroInt.*, 3:44–49, 2007.

[158] G. Stankovic, O. Darremont, M. Ferenc, D. Hildick-Smith, Y. Louvard, R. Albiero, M. Pan, J. F. Lassen, and T. Lefevre. Percutaneous coronary intervention for bifurcation lesions: 2008 consensus document from the fourth meeting of the European Bifurcation Club. *EuroIntervention*, 5:39–49, 2009.

[159] Boston Scientific, Natick, US, `http://www.bostonscientific.com/`, (accessed 3 Aug 2011).

[160] P. Mortier. *Computer Modelling of Coronary Bifurcation Stenting.* PhD thesis, Ghent University, Belgium, 2010.

[161] G. Finet, M. Gilard, B. Perrenot, G. Rioufol, P. Motreff, M. Gavit, and R. Prost. Fractal geometry of arterial coronary bifurcations: a quantitative coronary angiography and intravascular ultrasound analysis. *EuroInt.*, 3:490–498, 2007.

[162] A. Swillens, J. Degroote, J. Vierendeels, L. Lovstakken, and P. Segers. A simulation environment for validating ultrasonic blood flow and vessel wall imaging based on fluid-structure interaction simulations: ultrasonic assessment of arterial distension and wall shear rate. *Med Phys*, 37:4318–4330, 2010.

[163] K. Tchon, J. Dompierre, and R. Camarero. Conformal refinement of all-quadrilateral and all-hexahedral meshes according to an anisotropic metric. Presented at the 11th International Meshing Roundtable. Available at `http://www.imr.sandia.gov/papers/imr11/tchon.pdf`, (accessed 7 July 2011).

[164] S. Bangalore, S. Kumar, J. Wetterslev, A. A. Bavry, C. Gluud, D. E. Cutlip, and D. L. Bhatt. Carotid artery stenting vs carotid endarterectomy: meta-analysis and diversity-adjusted trial sequential analysis of randomized trials. *Arch. Neurol.*, 68:172–184, 2011.

[165] T. G. Brott, R. W. Hobson, G. Howard, G. S. Roubin, W. M. Clark, W. Brooks, A. Mackey, M. D. Hill, P. P. Leimgruber, A. J. Sheffet, V. J. Howard, W. S. Moore, J. H. Voeks, L. N. Hopkins, D. E. Cutlip, D. J. Cohen, and J. J. et al. Popma. Stenting versus endarterectomy for treatment of carotid-artery stenosis. *N. Engl. J. Med.*, 363:11–23, 2010.

[166] J. Ederle, J. Dobson, R. L. Featherstone, L. H. Bonati, H. B. van der Worp, G. J. de Borst, T. H. Lo, P. Gaines, P. J. Dorman, S. Macdonald, P. A. Lyrer, J. M. Hendriks, C. McCollum, P. J. Nederkoorn, M. M. Brown, and A. et al. Algra. Carotid artery stenting compared with endarterectomy in patients with symptomatic carotid stenosis (International Carotid Stenting Study): an interim analysis of a randomised controlled trial. *Lancet*, 375:985–997, 2010.

[167] K. I. Paraskevas, D. P. Mikhailidis, and F. J. Veith. Mechanisms to explain the poor results of carotid artery stenting (CAS) in symptomatic patients to date and options to improve CAS outcomes. *J. Vasc. Surg.*, 52:1367–1375, 2010.

[168] Z. Li and C. Kleinstreuer. Blood flow and structure interactions in a stented abdominal aortic aneurysm model. *Med Eng Phys*, 27:369–382, 2005.

[169] P. K. Shah. Inflammation, neointimal hyperplasia, and restenosis: as the leukocytes roll, the arteries thicken. *Circulation*, 107:2175–2177, 2003.

[170] M. Cosottini, M. C. Michelassi, W. Bencivelli, G. Lazzarotti, S. Picchietti, G. Orlandi, G. Parenti, and M. Puglioli. In stent restenosis predictors after carotid artery stenting. *Stroke Res Treat*, 2010, (in press).

[171] R. A. Ener, D. Fiss, A. Georgakis, N. M. Wolf, N. Pandit, and G. N. Piegari. Carotid artery in-stent restenosis after carotid artery stenting. *J Invasive Cardiol*, 20:286–291, 2008.

[172] K. Groschel, A. Riecker, J. B. Schulz, U. Ernemann, and A. Kastrup. Systematic review of early recurrent stenosis after carotid angioplasty and stenting. *Stroke*, 36:367–373, 2005.

[173] D. Carnelli, G. Pennati, T. Villa, L. Baglioni, B. Reimers, and F. Migliavacca. Mechanical properties of open-cell, self-expandable shape memory alloy carotid stents. *Artif Organs*, 35:74–80, 2011.

[174] S. Pant, N. W. Bressloff, A. I. Forrester, and N. Curzen. The influence of strut-connectors in stented vessels: a comparison of pulsatile flow through five coronary stents. *Ann Biomed Eng*, 38:1893–1907, 2010.

[175] R. Balossino, F. Gervaso, F. Migliavacca, and G. Dubini. Effects of different stent designs on local hemodynamics in stented arteries. *J Biomech*, 41:1053–1061, 2008.

[176] S. Appanaboyina, F. Mut, R. Lohner, C. A. Putman, and J. R. Cebral. Computational fluid dynamics of stented intracranial aneurysms using adaptive embedded unstructured grids. *Int J Numer Meth Fluids*, 57:475–493, 2008.

[177] Abbott Vascular, `http://www.abbottvascular.com/av_dotcom/url/content/en_US/10.10.330.10:10/general_content/Abtdiv_General_Content_0000104.htm`, (accessed 5 May 2009).

[178] P. J. Prendergast, C. Lally, S. Daly, A. J. Reid, T. C. Lee, D. Quinn, and F. Dolan. Analysis of prolapse in cardiovascular stents: a constitutive equation for vascular tissue and finite-element modelling. *J Biomech Eng*, 125:692–699, 2003.

[179] F. Auricchio, R. L. Taylor, and Lubliner J.

[180] P. Reymond, F. Merenda, F. Perren, D. Rufenacht, and N. Stergiopulos. Validation of a one-dimensional model of the systemic arterial tree. *Am. J. Physiol. Heart Circ. Physiol.*, 297:H208–222, 2009.

[181] D. W. Holdsworth, C. J. Norley, R. Frayne, D. A. Steinman, and B. K. Rutt. Characterization of common carotid artery blood-flow waveforms in normal human subjects. *Physiol Meas*, 20:219–240, 1999.

[182] X. He and D. N. Ku. Pulsatile flow in the human left coronary artery bifurcation: average conditions. *J Biomech Eng*, 118:74–82, 1996.

[183] S. W. Lee, L. Antiga, and D. A. Steinman. Correlations among indicators of disturbed flow at the normal carotid bifurcation. *J Biomech Eng*, 131:061013, 2009.

[184] M. Kim, D. B. Taulbee, M. Tremmel, and H. Meng. Comparison of two stents in modifying cerebral aneurysm hemodynamics. *Ann Biomed Eng*, 36:726–741, 2008.

[185] J. F. LaDisa, I. Guler, L. E. Olson, D. A. Hettrick, J. R. Kersten, D. C. Warltier, and P. S. Pagel. Three-dimensional computational fluid dynamics modeling of alterations in coronary wall shear stress produced by stent implantation. *Ann Biomed Eng*, 31:972–980, 2003.

[186] I. Larrabide, M. Kim, L. Augsburger, M. C. Villa-Uriol, D. Rufenacht, and A. F. Frangi. Fast virtual deployment of self-expandable stents: Method and in vitro evaluation for intracranial aneurysmal stenting. *Med Image Anal*, 2010.

[187] A. R. Williams, B. K. Koo, T. J. Gundert, P. J. Fitzgerald, and J. F. LaDisa. Local hemodynamic changes caused by main branch stent implantation and subsequent virtual side branch balloon angioplasty in a representative coronary bifurcation. *J. Appl. Physiol.*, 109:532–540, 2010.

[188] C. Kleinstreuer, Z. Li, and M. A. Farber. Fluid-structure interaction analyses of stented abdominal aortic aneurysms. *Annu Rev Biomed Eng*, 9:169–204, 2007.

[189] C. Kleinstreuer, Z. Li, C. A. Basciano, S. Seelecke, and M. A. Farber. Computational mechanics of Nitinol stent grafts. *J Biomech*, 41:2370–2378, 2008.

[190] S. de Putter, B. J. Wolters, M. C. Rutten, M. Breeuwer, F. A. Gerritsen, and F. N. van de Vosse. Patient-specific initial wall stress in abdominal aortic aneurysms with a backward incremental method. *J Biomech*, 40:1081–1090, 2007.

[191] B. Trachet, M. Renard, G. De Santis, S. Staelens, J. De Backer, L. Antiga, B. Loeys, and P. Segers. An Integrated Framework to Quantitatively Link Mouse-Specific Hemodynamics to Aneurysm Formation in Angiotensin II-infused ApoE -/- mice. *Ann Biomed Eng*, 39:2430–2444, 2011.

[192] P. Mortier, I. Krabbendam-Peters, M. De Beule, H. M. M. Van Beusekom, B. Van Der Smissen, G. De Santis, J. M. Ligthart, B. Verhegghe, and W. J. Van Der Giessen. Improved understanding of stent malapposition using virtual bench testing. *Interventional Cardiology*, 2011, (in press).

[193] A. Swillens, G. De Santis, J. Degroote, L. Lovstakken, J. Vierendeels, and P. Segers. Accuracy of carotid strain estimates from ultrasonic wall tracking: a study based on multiphysics simulations and in-vivo data. *IEEE Trans Med Imaging*, 2011, (in press).

[194] G. De Santis. Hemodynamics impact of stent-vessel (mal)apposition following carotid artery stenting: mind the gaps ! *Comput Methods Biomech Biomed Engin*, 2011, (submitted).

[195] J. Degroote, K. J. Bathe, and Vierendeels J. Performance of a new partitioned procedure versus a monolithic procedure in fluid-structure interaction. *Comput Struct*, 87:793–801, 2009.

Publications

Publications in international journals

First author

- G. De Santis, P. Mortier, M. De Beule, P. Segers, P. Verdonck, and B. Verhegghe. Patient-specific computational fluid dynamics: structured mesh generation from coronary angiography. *Medical and Biological Engineering and Computing*, 48, 4:371-380, 2010.

- G. De Santis, M. De Beule, P. Segers, P. Verdonck, and B. Verhegghe. Patient-specific computational haemodynamics: generation of structured and conformal hexahedral meshes from triangulated surfaces of vascular bifurcations. *Computer Methods in Biomechanics and Biomedical Engineering*, 14, 9:797-802, 2011.

- G. De Santis, M. De Beule, K. Van Canneyt, P. Segers, P. Verdonck, and B. Verhegghe. Full-hexahedral structured meshing for image-based computational vascular modeling. *Medical Engineering & Physics*, in press (available online).

- G. De Santis, M. Conti, B. Trachet, T. De Schryver, M. De Beule, J. Degroote, J. Vierendeels, F. Auricchio, P. Segers, P. Verdonck, and B. Verhegghe. Hemodynamics impact of stent-vessel (mal)apposition following carotid artery stenting: mind the gaps ! *Computer Methods in Biomechanics and Biomedical Engineering*, in press (available online).

- G. De Santis, A. B. Lennon, F. Boschetti, B. Verhegghe, P. Verdonck, and P. J. Prendergast. How can cells sense the elasticity of a substrate? An analysis using a cell tensegrity model. *European Cells and Materials*, in press (available online).

- G. De Santis, B. Trachet, M. Conti, M. De Beule, U. Morbiducci, P. Segers, P. Verdonck, and B. Verhegghe. A prospective patient-specific

study of carotid artery stenting: hemodynamic impact of open vs. closed stent cell design. To be submitted.

Co-author

- M. De Beule, P. Mortier, G. De Santis, M. Conti, P. Segers, P. Verdonck, and B. Verhegghe. A virtual product development strategy for minimally invasive medical devices. *Technology and Engineering*, 24, 1:19-26, 2010.

- F. Auricchio, M. Conti, M. De Beule, G. De Santis, and B. Verhegghe. Carotid artery stenting simulation: from patient-specific images to finite element analysis. *Medical Engineering & Physics*, 33, 3:281-289, 2011.

- M. Conti, D. Van Loo, F. Auricchio, M. De Beule, G. De Santis, B. Verhegghe, S. Pirrelli, and A. Odero. Impact of carotid stent cell design on vessel scaffolding: a case study comparing experimental investigation and numerical simulations. *Journal of Endovascular Therapy*, 18, 3:397-406, 2011.

- B. Trachet, M. Renard, G. De Santis, S. Staelens, J. De Backer, L. Antiga, B. Loeys, and P. Segers. An integrated framework to quantitatively link mouse-specific hemodynamics to aneurysm formation in angiotensin II-infused ApoE -/- mice. *Annals of Biomedical Engineering*, 39, 9:2430-2444, 2011.

- P. Mortier, I. Krabbendam-Peters, M. De Beule, H. M. M. Van Beusekom, B. Van Der Smissen, G. De Santis, J. M. Ligthart, B. Verhegghe, and W. J. Van Der Giessen. Improved understanding of stent malapposition using virtual bench testing. *Interventional Cardiology*, 6, 2:106-109.

- A. Swillens, G. De Santis, J. Degroote, L. Lovstakken, J. Vierendeels, and P. Segers. Accuracy of carotid strain estimates from ultrasonic wall tracking: a study based on multiphysics simulations and in-vivo data. *IEEE Transactions on Medical Imaging*, in press (available online).

- D. Gallo, G. De Santis, F. Negri, D. Tresoldi, R. Ponzini, D. Massai, M. Deriu, P. Segers, B. Verhegghe, G. Rizzo, and U. Morbiducci. On the use of in vivo measured flow rates as boundary conditions for image-based hemodynamic models of abnormal flow. *Annals of Biomedical Engineering*, in press (available online).

- B. Trachet, J. Bols, G. De Santis, S. Vandenberghe, B. Loeys, and P. Segers. CFD in the mouse aorta: do simplified boundary conditions and geometrical restrictions influence the computed flow field? A comparison with a reference data set. *Journal of Biomechanical Engineering-Transactions of the ASME*, under review.

- U. Morbiducci, R. Ponzini, D. Gallo, F. Pennella, D. Tresoldi, D. Massai, M. Deriu, G. De Santis, and G. Rizzo. Implications for in vivo measured 3D Phase Contrast MRI blood velocity profiles as inlet boundary conditions in numerical models of the human aorta. A preliminary study. To be submitted.

Abbreviations and symbols

Abbreviations

1D	one-dimensional
2D	two-dimensional
2.5D	two-and-a-half-dimensional
3D	three-dimensional
4D	four-dimensional
AAA	abdominal aortic aneurysm
AAo	ascending aorta
BCA	brachiocephalic artery
BC	boundary condition
BIF	bifurcation
Bifmesh	vascular bifurcation mesher
BL_Block	outer mesher block (boundary layer)
CAD	computer-aided design
CAE	computer-aided engineering
CAS	carotid artery stenting
CCA	common carotid artery
CFD	computational fluid dynamics
CG	conventional straight graft
COR	constant outflow ratio
CPU	central processing unit
CSD	computational structural dynamics
CT	computed tomography
CTA	computed tomographic angiography
cu	curliness
DAo	descending aorta
DBV	double-bifurcating vessel
DICOM	digital imaging and communications in medicine
Ds	diameter after stenting

Du	diameter before stenting
ECA	external carotid artery
ECG	electrocardiogram
FEA	finite element analysis
FFR	fractional flow reserve
FSI	fluid-structure interaction
GUI	graphical user interface
HEX	hexahedral
ICA	internal carotid artery
IN_Block	inner mesher block
IVUS	intravascular ultrasound imaging
LAD	left anterior descending coronary artery
LCA	left coronary artery
LCX	left circumflex artery
LDL	low-density lipoprotein
LMCA	left main coronary artery
LSA	left subclavian artery
MFR	measured flow rate
max	maximum
min	minimum
MRI	magnetic resonance imaging
Ndv	number of daughter vessels
Nrb	number of blocks in the real domain
Nxb	number of blocks in the flow extensions
OCT	optical coherence tomography
OSI	oscillating shear index
Pbe	parameter for isotropic refinement before projection
Pbl	parameter for boundary layers of the lumen
PDE	partial differential equations
Pil	parameter for isotropic refnement of the lumen
Piw	parameter for isotropic refnement of the wall
$PC-MRI$	magnetic resonance imaging
Prw	parameter for radial layers of the wall
Psw	parameter for surface refnement of the wall
$Qeas$	equiangle skew
ROI	region of interest
RR	R wave to R wave interval, inverse of the heart rate
RRT	relative residence time
SBV	single-bifurcating vessel
SF	stress free
SG	SwirlGraft
SJ	scaled Jacobian
St	scaled thickness
STL	stereolitography
Sw	strut width

TAWSS	time-averaged wall shear stress
te	tension
TET	tetrahedral
TP	tetrahedral-prismatic
Treemesh	vascular tree mesher
US	ultrasound imaging
VMTK	vascular modeling toolkit
VRML	virtual reality modeling language
WSS	wall shear stress magnitude
WSS	wall shear stress vector
WSS_{99}	99 area-weighted percentile of the wall shear stress magnitude
WSS$_{fc}$	face-centered wall shear stress vector

Symbols

a	cross-sectional parameter
A	area
b	cross-sectional parameter
c	cross-sectional parameter
G_1	first-order geometric continuity
n	unit vector
N	number
na	longitudinal parameter
nb	longitudinal parameter
nc	longitudinal parameter
nr	radial parameter
J	jacobian transformation
p	pressure
P	Fourier transform of the pressure waveform or parameter
P	position vector
q	flow
Q	Fourier transform of the flow waveform
S	outlet treatment scheme
t	scalar variable or time
T	time period
U	parent domain
X	physical domain
z	impulse response
Z	impedance spectrum

Greek Symbols

θ   angle between two edges of a face of an element

Units

GB   gigabyte
GHz   gigahertz
h   hour
kg   kilogram
m   meter
μm   micrometer
ml   milliliter
mm   millimeter
mmHg   millimeter of mercury
mPa   millipascal
Pa   Pascal
s   second
T   Tesla